CHARACTER OF VERTICAL-COMPONENT SIGNALS AT HIGH-GAIN, LONG-PERIOD STATIONS AND SIGNAL INTERFERENCE ON SEISMIC DETECTION NETWORKS

D. H. von Seggern, et al

Teledyne Geotech

Prepared for:

Air Force Technical Applications Center
Defense Advanced Research Projects Agency

21 July 1975

ESTIMATE OF VISUAL COMPONENT OF SIGNALS AT FAR AND LONG RANGES: STATISTICS AND VISUAL INTERFERENCE ON SIGNAL DETECTION VIEWING

Disclaimers: Neither the Defense Advanced Research Projects Agency nor the Air Force Technical Applications Center will be responsible for information contained herein which has been supplied by other organizations or contractors, and this document is subject to later revision as may be necessary. The views and conclusions presented are those of the authors and should not be interpreted as necessarily representing the official policies, either expressed or implied, of the Defense Advanced Research Projects Agency, the Air Force Technical Applications Center, or the US Government.

Unclassified

SECURITY CLASSIFICATION OF THIS PAGE (When Data Entered)

REPORT DOCUMENTATION PAGE

1 REPORT NUMBER: SDAC-TR-75-1	2 GOVT ACCESSION NO
3 RECIPIENT'S CATALOG NUMBER	
4 TITLE (and Subtitle): CHARACTER OF VERTICAL-COMPONENT SIGNALS AT HIGH-GAIN, LONG-PERIOD STATIONS AND SIGNAL INTERFERENCE ON SEISMIC DETECTION NETWORKS	5 TYPE OF REPORT & PERIOD COVERED: Technical
	6 PERFORMING ORG. REPORT NUMBER
7 AUTHOR(s): von Seggern, D. H. and Tillman, M. F.	8 CONTRACT OR GRANT NUMBER(s): F08606-74-C-0006
9 PERFORMING ORGANIZATION NAME AND ADDRESS: Teledyne Geotech, 314 Montgomery Street, Alexandria, Virginia 22314	10 PROGRAM ELEMENT, PROJECT, TASK AREA & WORK UNIT NUMBERS
11 CONTROLLING OFFICE NAME AND ADDRESS: Defense Advanced Research Projects Agency, Nuclear Monitoring Research Office, 1400 Wilson Blvd.-Arlington, Va. 22209	12 REPORT DATE: 21 July 1975
	13 NUMBER OF PAGES: 86
14 MONITORING AGENCY NAME & ADDRESS (if different from Controlling Office): VELA Seismological Center, 312 Montgomery Street, Alexandria, Virginia 22314	15 SECURITY CLASS (of this report): Unclassified
	15a DECLASSIFICATION DOWNGRADING SCHEDULE

16 DISTRIBUTION STATEMENT (of this Report)

APPROVED FOR PUBLIC RELEASE; DISTRIBUTION UNLIMITED.

17 DISTRIBUTION STATEMENT (of the abstract entered in Block 20, if different from Report)

18 SUPPLEMENTARY NOTES

19 KEY WORDS (Continue on reverse side if necessary and identify by block number)

Seismic Signal Interference
Seismic Surface Waves
Seismic Surface-Wave Attenuation
Signal Shape
Signal Coda
Simulation Model

20 ABSTRACT (Continue on reverse side if necessary and identify by block number)

The amplitude and period of over 600 long-period vertical-component seismic signals were measured at regular intervals in order to characterize the LR signal and its coda. Signal envelopes out to 20 minutes after LR onset were found to vary considerably, but coda amplitudes decayed rather uniformly with time. Using average signal and coda parameters and randomly-generated events, a program which simulates long-period signal interference at seismic stations was devised to predict interference effects on network detection

DD FORM 1 JAN 73 1473 EDITION OF 1 NOV 65 IS OBSOLETE

Unclassified

SECURITY CLASSIFICATION OF THIS PAGE (When Data Entered)

statistics. Increasing the size of a network should not increase the number of reported events with interference at any M_S, but lowering the station thresholds will increase this number at lower M_S values.

CHARACTER OF VERTICAL-COMPONENT SIGNALS AT HIGH-GAIN, LONG-PERIOD STATIONS AND SIGNAL INTERFERENCE ON SEISMIC DETECTION NETWORKS

SEISMIC DATA ANALYSIS CENTER REPORT NO.: SDAC-TR-75-1

AFTAC Project No.:	VELA VT/4709
Project Title:	Seismic Data Analysis Center
ARPA Order No.:	1620
ARPA Program Code No.:	3F10
Name of Contractor:	TELEDYNE GEOTECH
Contract No.:	F08606-74-C-0006
Date of Contract:	01 July 1974
Amount of Contract:	$2,237,956
Contract Expiration Date:	30 June 1975
Project Manager:	Royal A. Hartenberger (703) 836-3882

P. O. Box 334, Alexandria, Virginia 22314

APPROVED FOR PUBLIC RELEASE; DISTRIBUTION UNLIMITED.

ABSTRACT

The amplitude and period of over 600 long-period vertical-component seismic signals were measured at regular intervals in order to characterize the LR signal and its coda. Signal envelopes out to 20 minutes after LR onset were found to vary considerably, but coda amplitudes decayed rather uniformly with time. Using average signal and coda parameters and randomly-generated events, a program which simulates long-period signal interference at seismic stations was devised to predict interference effects on network detection statistics. Increasing the size of a network should not increase the number of reported events with interference at any M_s, but lowering the station thresholds will increase this number at lower M_s values.

TABLE OF CONTENTS

LIST OF FIGURES

LIST OF FIGURES (Continued)

LIST OF TABLES

INTRODUCTION

The space-time distribution of seismic activity over the globe often results in the simultaneous arrival of two or more signals at a particular station. This phenomenon is especially serious in a detection context when one event is large and effectively masks the smaller arriving signals of one or more other events. The amount of actual interference on long-period stations has been documented by Mack and Robertson (1973) and von Seggern (1974); it can affect 10 to 20 percent of the seismic events which occur, and so in detection it is a significant hindrance which is not accounted for in routine prediction of seismic network capability. For a network, one might presume that the addition of more stations at various sites on the globe should ameliorate the interference problem since there are then more chances for separation in arrival time of signals from events which occur close in time but not in space. On the other hand the interference problem may increase in severity as the threshold of network drops, due to more stations, since many more events become involved. (One might expect though that the advantage of a lower threshold outweighs any increased interference problem.) These same presumptions apply when the network threshold is decreased by improvements in existing sites; that is, by the lowering of noise background on recordings.

These presumptions concerning interference problems on improved networks need to be validated theoretically. The data of Mack and Robertson or of von Seggern cannot be used for prediction because they represent particular networks of stations having specific noise levels and also because they are formed in response to necessarily incomplete epicenter lists created with short-period data and thus cannot be generalized. Therefore a simulation approach is required to fully investigate interference effects with a variety of network configurations and with stations having lower thresholds. In order to perform such simulation, knowledge of the duration and shape of typical long-period signal trains is necessary. Such quantities depend on recording distance, magnitude, depth of the event, and structure of the path. If we can parameterize the signal according to these variables, then a

reasonable simulation of the real seismic interference situation on the globe can be programmed. Alsup and Lambert (1973) made a statistical characterization of LR (fundamental-mode Rayleigh waves) signal amplitudes; but because their data was insufficient as a global sample, because they only measured signal amplitudes at intervals beyond the maximum recorded amplitude (that part of the signal which is normally termed "coda"), and because they did not take a sufficiently detailed approach to signal characterization, we undertook to newly measure hundreds of long-period signals and correct these deficiencies. The first part of this report describes the measuremnt of these signals, the second part describes in detail the character of LR signals as determined by these measurements, and the third part presents the composition and results of a program which simulates interference on a network of long-period stations. We will be concerned with Rayleigh waves (and therefore vertical-component recording) only in this report; a parallel study on Love waves would be a more difficult task since horizontal recordings always contain some Rayleigh-wave motion which would need to be eliminated.

SIGNAL MEASUREMENTS

High-gain, long-period recordings of the LPE (Long Period Experimental) network were used for signal measurements in this study. The particular sites were: ALQ, CHG, CTA, EIL, KIP, KON, OGD, and TLO. Since the LPE instruments have high-gain outputs peaked at greater periods than most conventional long-period instruments, the signal shapes reported in this study should differ from those derived from conventional instruments. We in fact have measured several signals on the LPE low-gain seismograms, which were produced by instruments with responses similar to those of the WWSSN, and found that the signals differed distinctly in most cases from those measured on the high-gain seismograms. Thus the results of this study are strictly applicable to LPE high-gain recording only.

In order to sample various propagation paths on the globe, we selected eight seismic regions (Flinn and Engdahl, 1965) for signal sources; Alaska-Aleutian Arc (1), Mexico-Guatemala Area (5), Andean South America (8), Kermadec-Tonga-Samoa Area (12), New Guinea (15), Japan-Kuriles-Kamchatka (19), Middle East-Crimea-Balkans (30), and Hindu Kush-Pamir (48). Signals actually measured were fairly evenly distributed over these regions and over the eight stations used as listed in Table I. A total of 611 signals made up the final data base. Epicenters in 1972 were used, and only those events whose depths of focus were listed at less than 100 km contributed to the final data base. (Initially some deep event signals were measured, but their shapes were seen to differ significantly from those of shallower events. Later, a justification for ignoring deep events will be given.)

We were interested not merely in that part of the signal normally termed "coda," that is, the continued motion after the arrival of the fundamental Rayleigh mode along the great circle path but also in the relative amplitudes of the entire long-period signal train. Our objective was to measure the long-period signal from the P-wave emergence through to that point where the coda merged into the background noise. For this reason, data selection began with the largest events and moved down into smaller events only if they were

TABLE I

Distribution of Signal Measurements
by Station and Seismic Region

Station	Seismic Region 1	5	8	12	16	19	30	48
ALQ	8	10	11	9	11	10	12	9
CHG	12	4	5	11	10	11	5	8
CTA	12	7	14	9	7	11	3	3
EIL	13	4	11	10	8	11	12	12
KIP	12	9	12	10	12	12	5	2
KON	10	9	9	10	10	12	11	12
OGD	11	12	11	9	12	10	9	7
TLO	11	12	12	9	11	10	11	4

Seismic Region	Name
1	Alaska-Aleutian Area
5	Mexico-Guatemala Area
8	Andean South America
12	Kermadec-Tonga-Samoa Area
16	New Guinea
19	Japan-Kuriles-Kamchatka
30	Middle East-Crimea-Balkans
48	Hindu-Kush and Pamir

required to obtain a sufficient sample. Many of the largest signals overdrove the recordings and were thus unusable. In order to get a good sample for each station from each seismic region, it was necessary to use some signals for which body waves were below the noise level and finally some signals which were of limited duration even in the Rayleigh and coda parts. Arrival times for P, S, and 40-second LR were predicted by routine procedures in order to pinpoint the arrival of these phases. Finally, because most selected signals had no visible body waves, the measurements of the signal train between P and LR onset were not subsequently used in signal characterization; but some data is available for a further study if needed. (Later we will justify ignoring this part of the long-period signal for simulation purposes.)

The analysis procedure was to measure the amplitude and period of the signal at two-minute intervals following the onset of P, S, or LR, whichever was first visible. In each case it was noted with which phase measurements began. This required from five to fifty or more such measurements per signal. The amplitude in each two-minute interval was taken to be the maximum within the interval, and the period was taken to be the dominant or average period. The measurements were coded, punched, and edited to become the data base for long-period signal characterization.

SIGNAL CHARACTER

DATA BASE

In characterizing the long-period signals, we disregarded the body-wave portion and concentrated on that portion following onset of LR because body waves are detectable only for events above roughly 4.5-5.0(m_b) and because their duration is short relative to the LR and coda portions on the long-period seismogram. The portion of a typical LPE seismogram taken up with body waves is very small, only a few percent of a day's recording time. Thus, any precision gained by attempting to model the body-wave portion of the seismogram for a simulation experiment would probably be small and would not be worth the added complexity introduced into the simulation. We will not be significantly underestimating interference effects by neglecting body waves.

We first plotted the signal amplitudes of all the selected events for each station-region pair; these plots are contained in the appendix. Each event was normalized by the maximum amplitude before plotting; note that the vertical amplitude scale is logarithmic. These plots represent the signal from LR onset to whenever the coda died out, that is, became indistinguishable from background noise. In most cases the plots begin with the longest period LR, which is normally near 40 sec or greater for large events recorded by these LPE instruments. The maximum signal amplitude generally occurs within 3 or 4 minutes of LR onset and occurs after 10 minutes in only a few cases. Some signals were used which had low enough S/N ratios that the earliest LR cycles of motion with periods of 40 seconds or more were probably not seen; in these cases the measurements began shortly before or at the maximum amplitude. Since this maximum occurs close to the earliest LR arrival anyway and since the long coda train will not be shifted too much relative to larger events, it is acceptable to plot these smaller events with the first measured arrival at zero time even though it is not strictly the fundamental LR onset. If all events for a station-region were of equally high S/N ratio, we would expect more similarity among signal shapes for each station region pair. We might have obtained the same improvement by trying to align signals according to reported periods before plotting.

For each station-region pair in the appendix, an average signal shape is computed using for each two-minute interval the equally weighted, normalized amplitudes from all the events having a measurement at that interval. The average coda shape so derived is less reliable as time increases and the measurements become fewer. These average coda shapes are reproduced and grouped by station in Figure 1. We provide in Table II the average epicentral distance for events in each station-region pair and the rough percentage of oceanic and continental path involved. These numbers relate to the coda shapes, as will be discussed next.

PARAMETERIZING SIGNAL SHAPES

We next attempted to parameterize the average signal shapes shown in Figure 1. Only nonlinear functions were considered, and a program which fitted these functions in a least squares sense by Gauss-Newton iteration on the parameters was employed. As seen in the plots, every coda ends with some finite amplitude, presumably the background noise level; therefore, before fitting, we added one point, equal in amplitude to this last point, to the beginning of each set of amplitudes to be fitted, at one minute prior to the first measured amplitude. The time scale as seen in Figure 1 was then shifted back one minute for fitting purposes. This results in a rather rapid rise time to the signal. Although this rapid rise will not realistically reflect most signal shapes because body waves and higher-mode LR usually precede the fundamental LR, we feel it is not unrealistic enough to degrade our simulation of long-period interference since the amplitudes preceding fundamental LR are usually much smaller and in many cases are simply background noise.

Several functional forms were used in attempting to fit the normalized coda; by far the most satisfactory function with ≤ 4 parameters was:

$$\log_{10} [\hat{A}(t)] = p_1(1-e^{p_2 t})\, e^{p_3 t} + p_4$$

where t is measured in minutes and log A is, arbitrarily, the logarithm of the average of the normalized codas seen in the appendix plus 0.3. This function includes an exponential decay term $e^{p_3 t}$ with scaling parameter p_1; the $(1-e^{p_2 t})$ term provides a smooth rise from the noise background amplitude

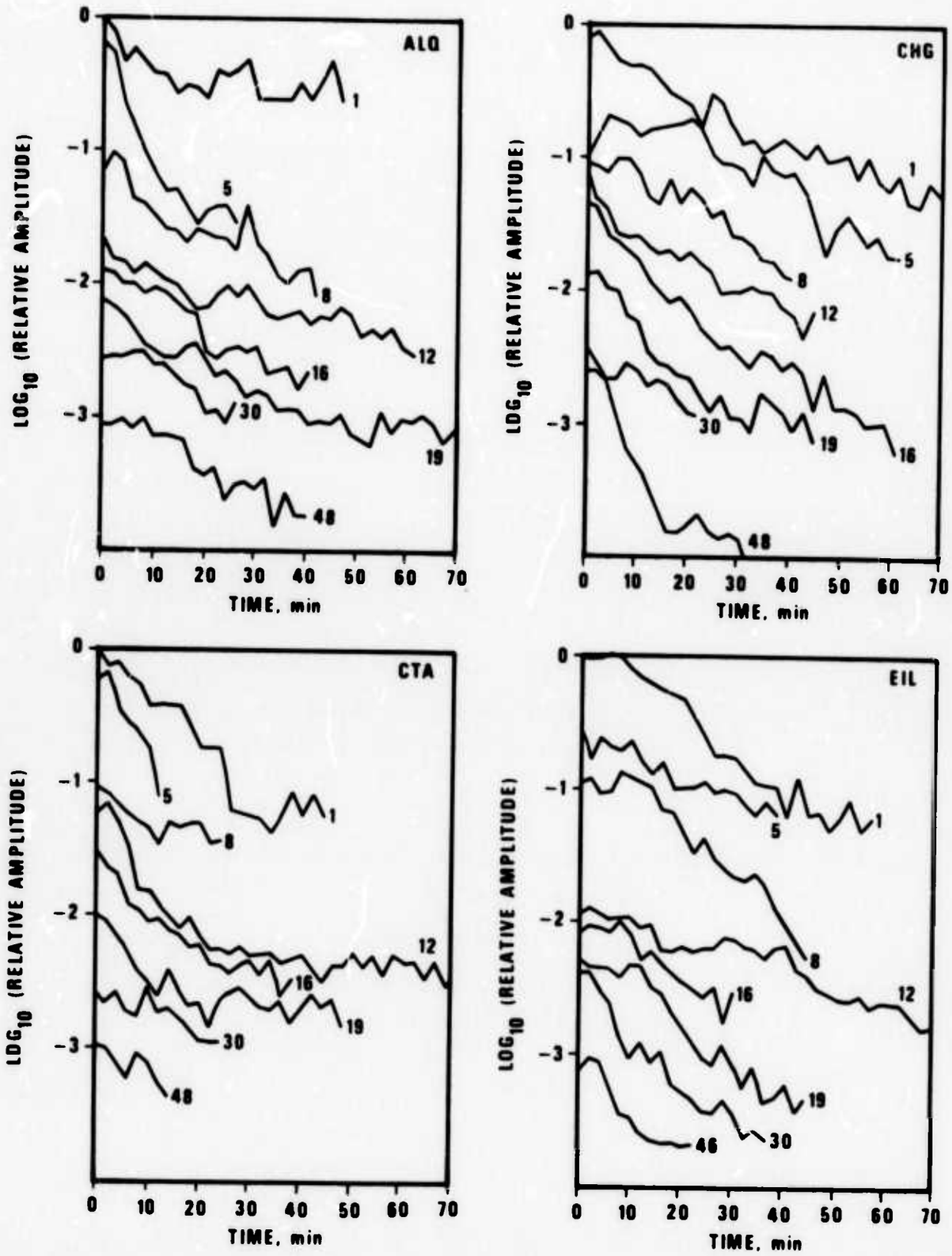

Figure 1. Average signal shapes (LR+coda) from shallow epicenters for 64 station-region pairs.

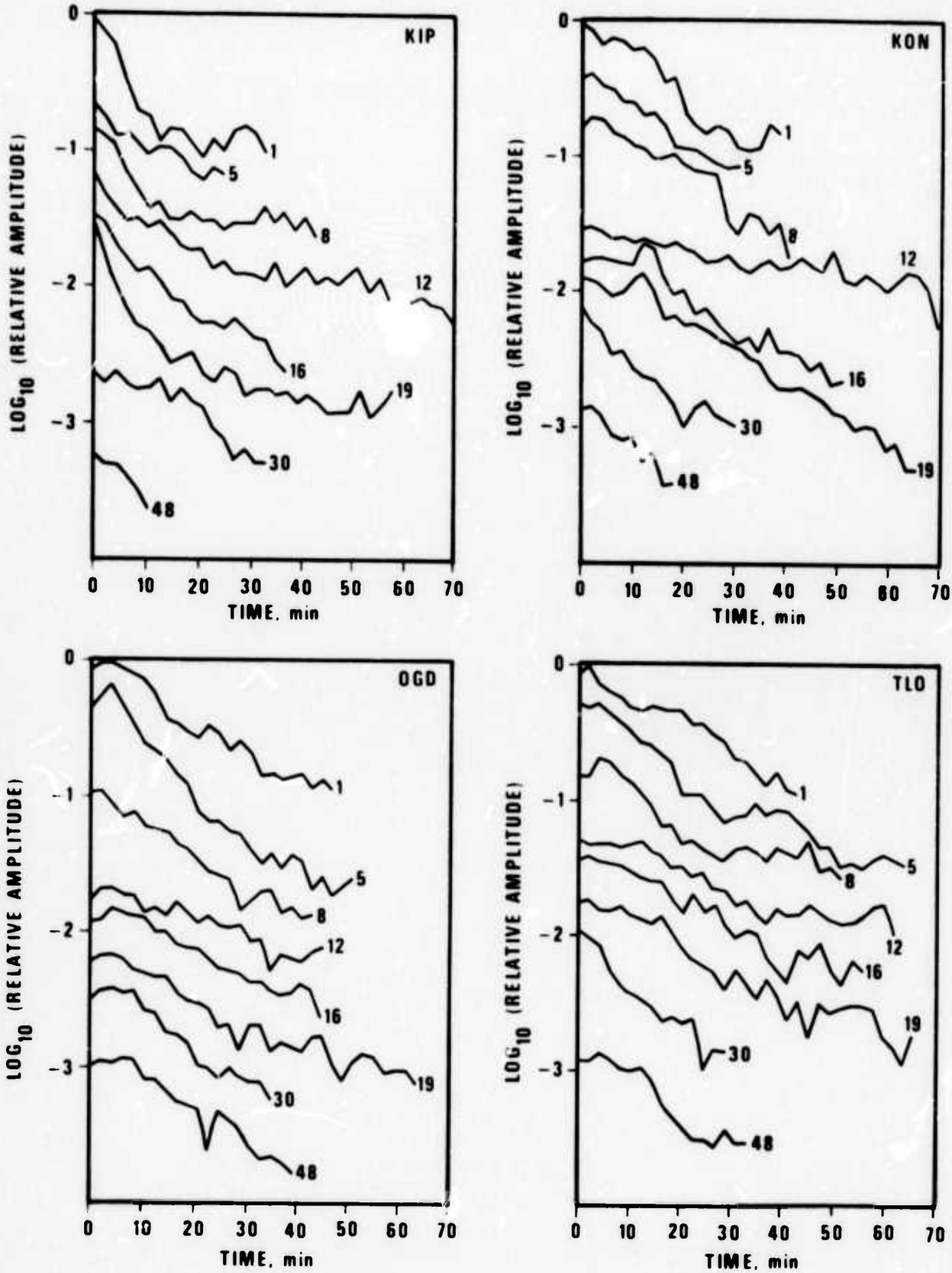

Figure 1. Average signal shapes (LR+coda) from shallow epicenters for 64 station-region pairs.

TABLE II

Average Distance and Path Structure for Measured Signals Belonging to Each Station-Region Pair

Station	Seismic Region							
	1	5	8	12	16	19	30	48
ALQ	48°/60*	22°/0	60°/30	90°/90	180°/90	70°/90	95°/50	108°/20
CHG	74°/50	143°/10	164°/80	93°/90	49°/90	50°/50	63°/10	32°/0
CTA	82°/100	123°/100	123°/1[illegible]	35°/100	19°/50	75°/90	125°/40	91°/50
EIL	92°/40	116°/60	115°/30	151°/60	110°/30	84°/0	11°/0	30°/0
KIP	34°/100	36°/100	92°/100	47°/100	66°/100	47°/100	120°/50	112°/50
KON	65°/90	84°/50	102°/50	143°/80	112°/40	73°/30	22°/0	44°/0
OGD	66°/20	32°/40	59°/50	113°/70	130°/70	80°/10	73°/60	96°/10
TLO	85°/80	82°/90	74°/70	103°/70	132°/60	81°/50	21°/50	55°/10

*Path structure as a percentage of oceanic - remainder is continental.

at zero time to the maximum amplitude; and the additive term p_4 relates directly to the logarithm of the background noise amplitude and does not pertain to coda shape itself. The final values of the four parameters for each station-region pair are given in Table III along with the residual mean square error between the estimated funciton and the actual data. (These particular parameters represent only the normalized signals, which will be appropriately scaled when simulating actual seismic observations.) Seven cases where convergence did not occur are indicated in the table; however, the residual square error in these cases is apparently not any larger than for the 57 converging cases, and so the fit is considered good for even these nonconverging cases. Several cases are also noted where p_2 hit the boundary limit and was held constant through subsequent iterations; again, the residual error in those cases is typically no greater than those cases where p_2 was allowed to vary throughout.

It was thought that the parameters p_1, p_2, and p_3 should show some dependence on the epicentral distance at which signals were recorded. The average distance for each station-region pair was given in Table II. In Figure 2 p_1, p_2, and p_3 are plotted versus these distances. A slight dependence on distance is apparent for each parameter, and conjectural lines have been visually fit to the data. In each case the dependence is as would be expected due to the effects of dispersion on Rayleigh waves; that is, the fundamental LR is progressively stretched out in time with increasing epicentral distance, leading to slower rise and decay times for the envelope of the signal. These parameters displayed in Figures 2a, 2b, and 2c are calculated for the coda together with the fundamental LR arrival; and so a large scatter with distance, unrelated to dispersion characteristics, occurs. Given the data in these figures, the use of a constant p_1, p_2, or p_3, say the 90° value, would not lead to a gross misrepresentation of signal shape at any distance since scatter at the extremes of 0° and 180° seem to overlap in all three cases.

DURATION

For simulation purposes it is necessary to estimate an appropriate duration for the signal, related to the event magnitude and the epicentral

TABLE III

Signal Parameter Estimates for

$$f(t) = p_1(e^{p_2 t})\, e^{p_3 t} + p_4$$

Station	Area	Δ	p_1	p_2	p_3	p_4	$\overline{e^2}$	Comments
ALQ	1	48°	.69	- 2.08	-.199	1.66	.0073	
	5	22°	2.02	- 1.49	-.156	.89	.0035	
	8	60°	1.05	- 1.23	-.138	1.53	.0084	
	12	90°	.65	-10.00	-.030	1.49	.0080	p_2 bounded
	16	108°	.98	- 1.84	-.051	1.74	.0095	
	19	70°	1.42	-10.00	-.020	.75	.0055	p_2 bounded
	30	94°	2.01	- .12	-.173	1.78	.0102	did not converge
	48	108°	.95	- 1.26	-.043	1.45	.0087	
CHG	1	74°	1.38	- 2.64	-.028	.92	.0063	
	5	143°	1.11	- .84	-.014	1.13	.0084	
	8	164°	.92	- 1.89	-.034	1.39	.0099	
	12	93°	1.01	-10.00	-.056	1.25	.0050	p_2 bounded
	16	49°	1.99	- 3.48	-.032	.36	.0019	
	19	49°	1.59	- 1.42	-.078	1.08	.0063	
	30	63°	.55	-10.00	-.060	1.72	.0081	p_2 bounded
	48	31°	2.08	- 1.30	-.103	.78	.0083	
CTA	1	82°	1.72	- 2.17	-.043	.77	.0275	
	5	123°	1.60	- 1.13	-.145	1.26	.0180	
	8	123°	.62	- 1.24	-.205	1.87	.0041	
	12	35°	1.69	- 1.43	-.090	.89	.0041	
	16	19°	1.10	- 3.44	-.075	1.29	.0027	
	19	75°	1.00	- 1.64	-.125	1.50	.0103	
	30	125°	.50	- 1.96	-.059	1.76	.0086	
	48	91°	.33	- 9.77	-.112	1.99	.0095	
EIL	1	92°	1.54	- 1.67	-.031	.89	.0112	
	5	116°	.79	-10.00	-.030	1.43	.0058	p_2 bounded
	8	115°	1.48	- 1.73	-.027	.88	.0164	
	12	151°	1.17	- 3.25	-.012	1.06	.0047	
	16	110°	1.01	- .22	-.081	1.68	.0229	
	19	84°	1.35	- 1.70	-.038	1.07	.0171	
	30	11°	1.54	- 2.01	-.068	.92	.0061	
	48	30°	1.68	- .28	-.176	1.60	.0106	did not converge

TABLE III (Continued)

Signal Parameter Estimates for

$$f(t) = p_1(e^{p_2 t})\, e^{p_3 t} + p_4$$

Station	Area	Δ	p_1	p_2	p_3	p_4	$\overline{e^2}$	Comments
KIP	1	34°	1.83	- .58	-.236	1.31	.0141	did not converge
	5	36°	.56	- 5.59	-.112	1.71	.0038	
	8	92°	1.18	- 1.26	-.160	1.45	.0021	
	12	47°	1.27	-10.00	-.027	.92	.0025	p_2 bounded
	16	66°	1.22	- 3.47	-.054	1.10	.0021	
	19	47°	1.51	- 2.94	-.015	.70	.0069	
	30	120°	.92	- 1.59	-.043	1.45	.0147	
	48	112°	.77	- .78	-.182	1.79	.0069	did not converge
KON	1	65°	1.21	- 1.64	-.057	1.27	.0182	
	5	84°	1.02	- 1.39	-.068	1.48	.0040	
	8	102°	1.22	- 1.63	-.032	1.17	.0125	
	12	143°	.92	-10.00	-.011	1.29	.0016	p_2 bounded
	16	112°	1.16	- 1.35	-.030	1.21	.0162	
	19	73°	1.51	- 2.94	-.015	.70	.0069	
	30	22°	1.05	- 2.98	-.078	1.32	.0045	
	48	44°	.86	- 1.29	-.102	1.63	.0063	
OGD	1	66°	1.18	- 1.47	-.047	1.20	.0039	
	5	32°	1.93	- 1.20	-.052	.72	.0060	
	8	60°	1.17	- 1.94	-.048	1.24	.0071	
	12	113°	.49	- .81	-.063	1.84	.0023	
	16	130°	.96	- .78	-.044	1.49	.0038	did not converge
	19	80°	1.17	- 1.60	-.034	1.26	.0053	
	30	73°	1.25	- .62	-.064	1.38	.0069	did not converge
	48	96°	1.08	- 1.28	-.042	1.37	.0096	
TLO	1	85°	.97	- 2.64	-.029	1.30	.0039	
	5	81°	1.51	- 1.76	-.041	1.02	.0068	
	8	74°	1.23	- .57	-.063	1.40	.0090	
	12	103°	.79	- 1.91	-.029	1.49	.0051	
	16	132°	1.00	- 1.83	-.032	1.34	.0043	
	19	81°	.97	- 1.74	-.061	1.44	.0090	
	30	21°	1.21	- 2.07	-.080	1.27	.0081	
	48	55°	1.18	- .30	-.082	1.56	.0189	did not converge

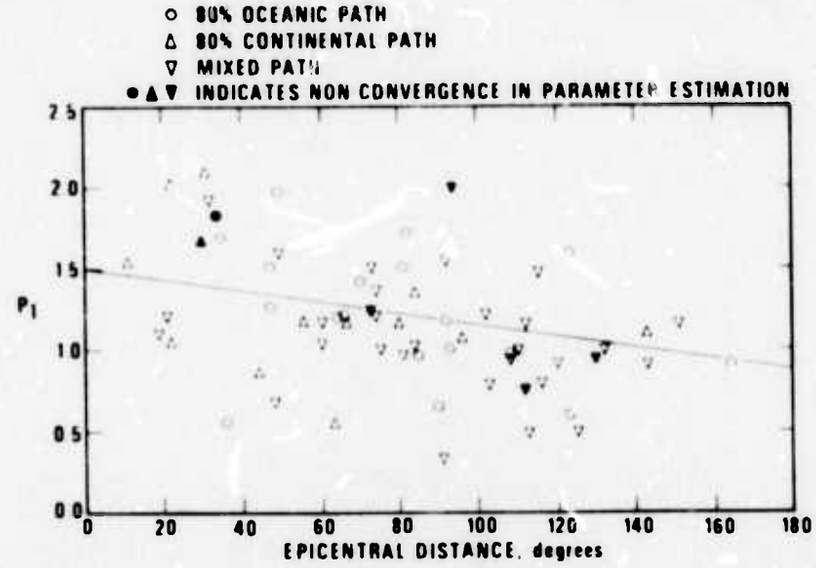

Figure 2a. Signal parameter estimate p_1 in $f(t) = p_1(1-e^{p_2 t})e^{p_3 t} + p_4$ versus epicentral distance (distance from Table II).

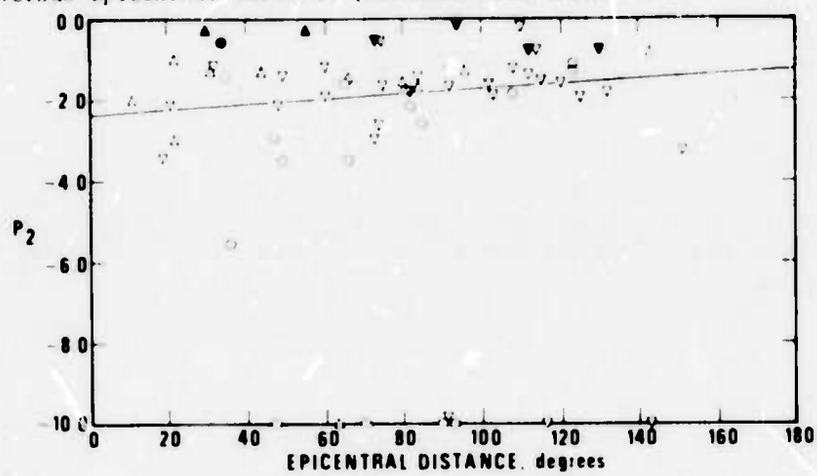

Figure 2b. Signal parameter estimate p_2 in $f(t) = p_1(1-e^{p_2 t})e^{p_3 t} + p_4$ versus epicentral distance (distance from Table II).

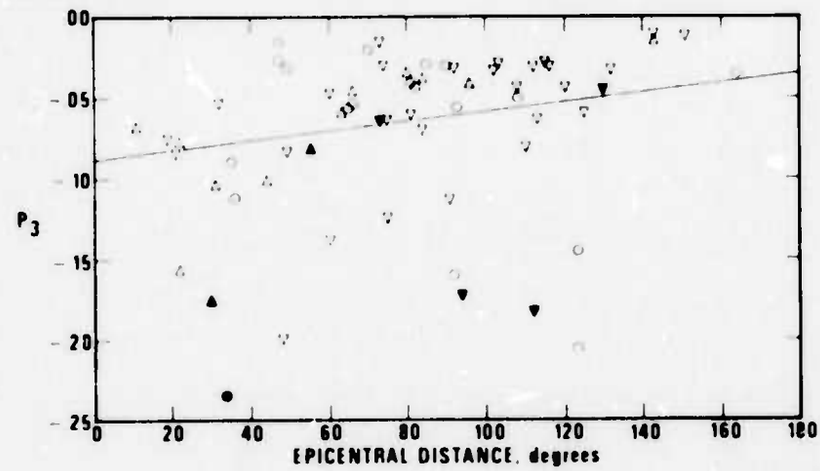

Figure 2c. Signal parameter estimate p_3 in $f(t) = p_1(1-e^{p_2 t})e^{p_3 t} + p_4$ versus epicentral distance (distance from Table II).

distance, because the amount of interference will directly depend on assigned signal durations. Figure 3 shows the plot of the reported duration of the measured signals versus their maximum amplitude (m_b ground displacement, peak-to-peak, between 17 and 23 sec) divided by period. We reiterate that the signal is considered to span from the LR onset to the end of the coda. On this plot, a visual estimate was made for the dependence of duration on maximum signal amplitude:

$$D = 0.741 \cdot \left(\frac{A}{T}\right) 1.067$$

where A/T is peak-to-peak amplitude in millimicrons over period in seconds and D is in minutes. It is often true that 20-sec LR amplitudes are not the maximum on the recorded trace; but with few exceptions, they are within a factor of two of the maximum amplitudes for shallow shocks measured in this study. Thus we feel that duration can be reliably linked to those LR amplitudes routinely used in computing M_s. There is of course considerable scatter in the data of Figure 3, and the above relation can only be considered to be a rough prediction of duration. Any simulation of long-period signals must produce data which reasonably agrees with this empirical data.

It was also felt that signal duration should depend on epicentral distance. To check this, we have plotted in Figure 4a all the durations for events with $1.70 \leq \log (A/T) < 2.00$ appearing in the previous figure versus the epicentral distance of these events. This subset of signals then has relatively high maximum amplitudes all within a factor of two of one another. Figure 4b is a similar plot using only events with $1.00 \leq \log (A/T) < 1.30$. Again, as with the parameters P_1, P_2, and P_3, there is considerable scatter and little discernible trend with distance. Such behavior is not unreasonable due to the scattering in a heterogeneous earth. On the basis of this plot, one would tend to ignore epicentral distance in assigning durations to signals; in fact, this would be required if one chose to assume constant signal shape with distance.

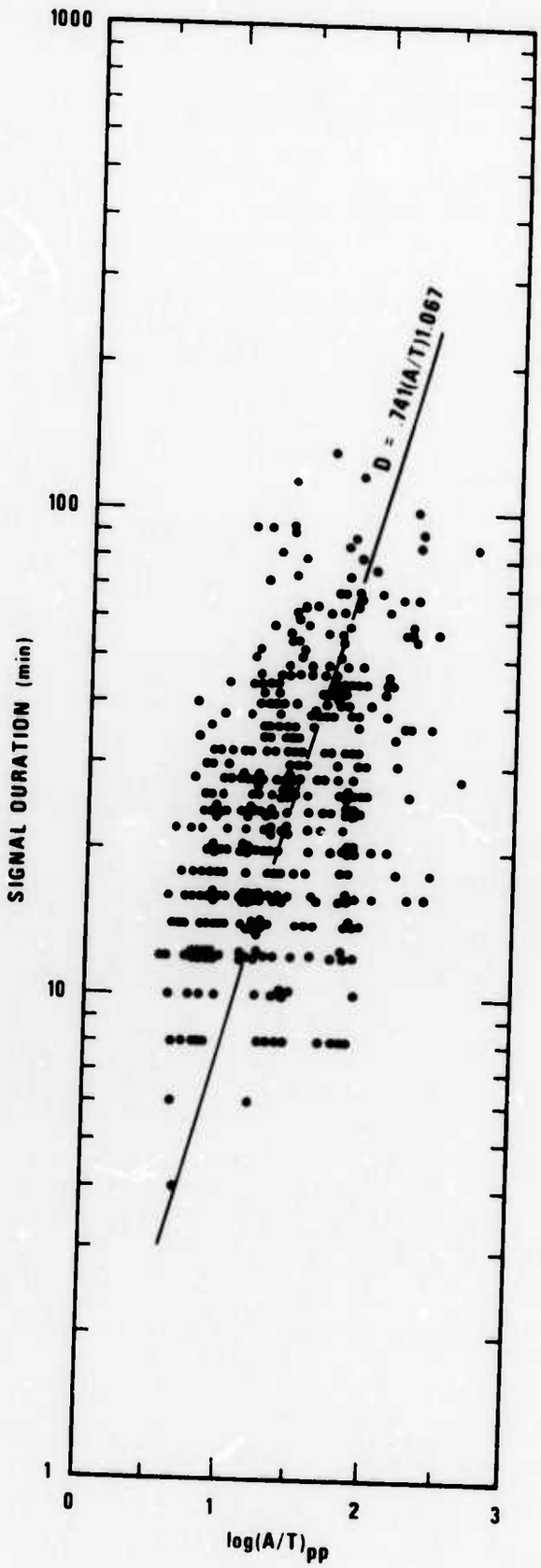

Figure 3. Relationship of signal duration to maximum amplitude of the signal (real data).

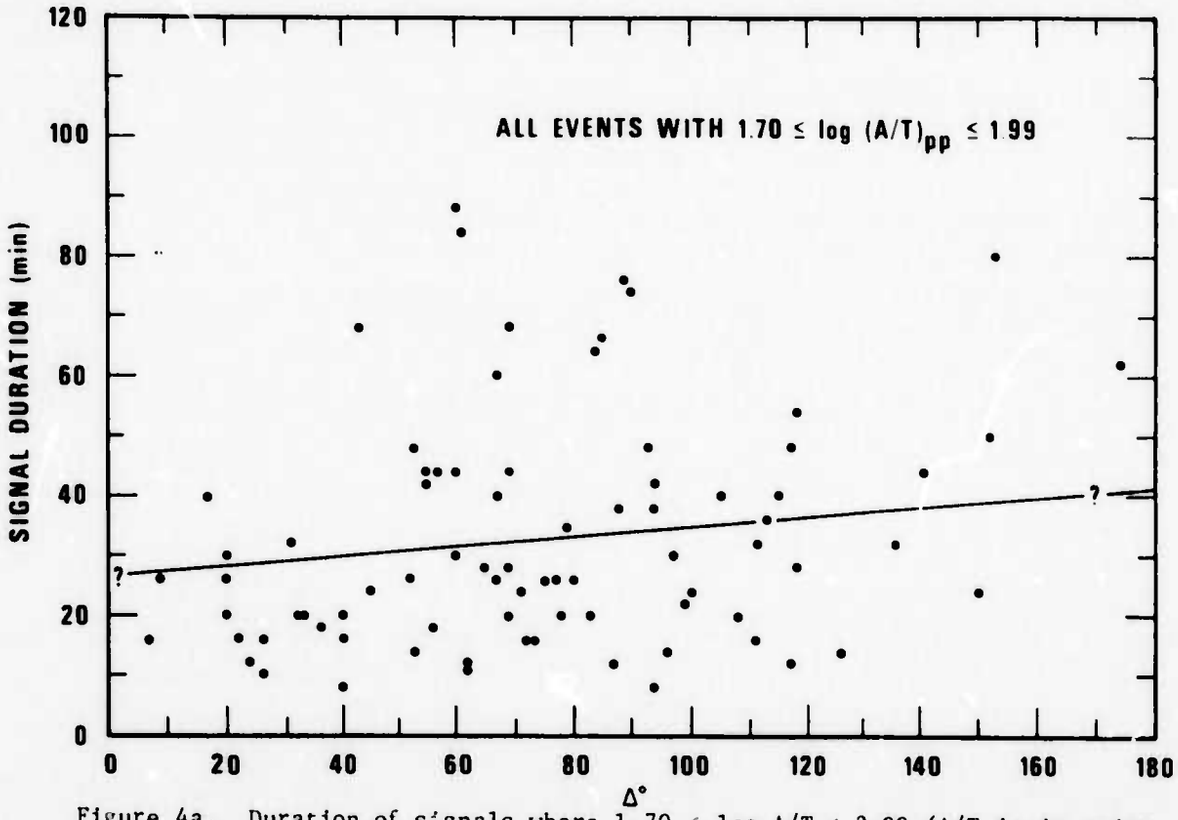

Figure 4a. Duration of signals where 1.70 $\leq$ log A/T < 2.00 (A/T is in units of millimicrons/second) versus the epicentral distance of recording.

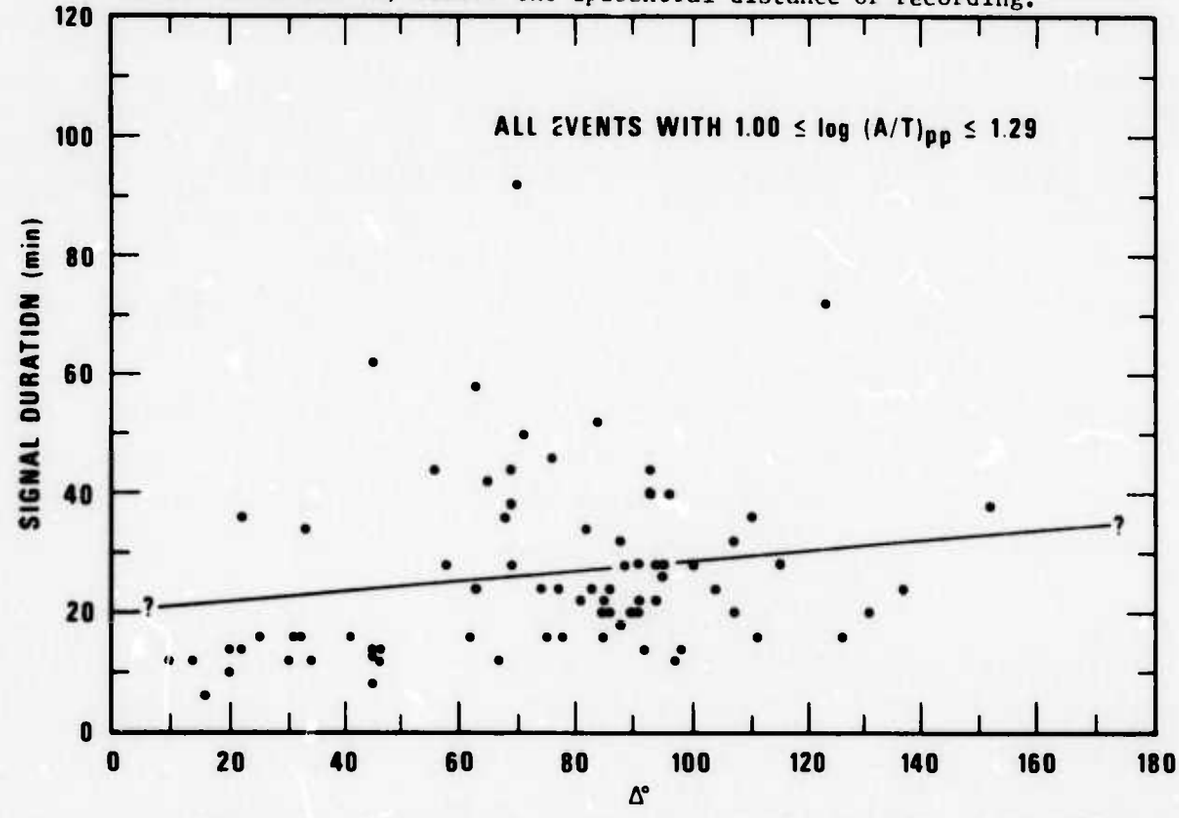

Figure 4b. Duration of signals where 1.00 $\leq$ log A/T < 1.30 (A/T is in units of millimicrons/seconds) versus the epicentral distance of the recording.

LONG-TERM CODA AMPLITUDES

As stated previously, many signals could not be used for measuring signal shape because they were overdriven on the LPE recordings. With this restriction we were unable to measure the long-term coda amplitudes visible for large events--our longest signal in the data base was 132 minutes while codas for large events (m_b > 5.5 approximately) continue for several hours. Although events with m_b > 5.5 occur at the rate of only roughly one every four days, their prolonged coda makes them account for a much more significant portion of the interference problem than their mere number might indicate. We felt it necessary to gather some data on the coda amplitudes for large events to be used whenever needed in the simulation program; a simple extrapolation of the signal shape function estimated from smaller, shorter signals might be very inaccurate for times greater than an hour or so, especially since we have used an exponential function in the fitting of signal shapes.

To this end we examined our LPE eight-month data file (von Seggern, 1974) for LR signals which had been indicated as overdriven at a station by the analysts. Signals were then examined to see both if they extended for at least 200 minutes after the LR arrival and if they were readable within 10 to 30 minutes after this arrival. Also, it was necessary that no signals from other events large enough to be recorded at the station arrived during this coda. Clearly, subjective judgement was involved here, but we tried to be reasonably sure that no other events were contributing to the coda. These criteria together were rather stringent; seventeen signals which met them were found though, and they were from six events as listed in Table IV. Amplitude and period of the LR signal and coda was measured at ten-minute intervals after the LR onset, starting whenever the recording became readable, in the same manner as done at two-minute intervals for the 611 signals in our main data base (except that amplitudes associated with periods > 50 sec were ignored here).

Recorded amplitude (millimeters) versus time for the six events is shown in Figure 5. Arrivals of R_2 are apparent in many of the plots where amplitudes increase with time, and these arrivals could indeed be seen on the recordings

TABLE IV

Epicenter Information (NOS) on Events
Used for Long-Term Coda Measurements

Date	Origin Time	m_b	Depth(km)	Longitude	Latitude	Seismic Region No.
7 Jan 72	06:25:48	5.9	33	2.1S	139.0E	16
20 Mar 72	23:31:49	6.0	46	51.3N	179.2W	1
2 May 72	06:56:23	5.8	33	5.2N	100.3W	44
5 May 72	23:16:28	5.6	32	4.1S	152.7E	15
12 Jun 72	19:47:37	5.8	44	53.3N	166.8W	1
24 Jun 72	15:29:22	6.0	47	36.2N	69.7E	48

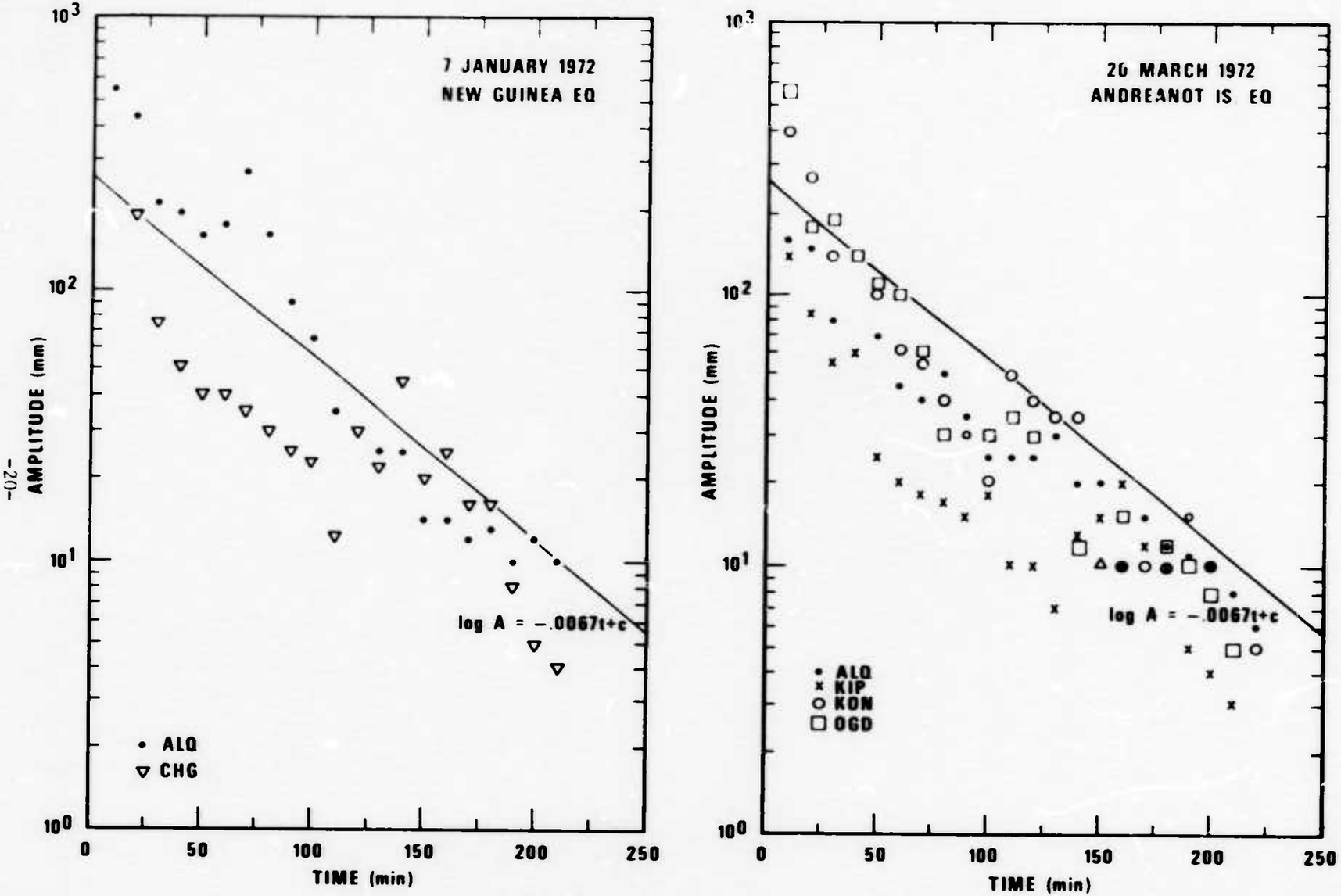

Figure 5. Amplitude versus time after LR onset for large earthquakes (LPE vertical component).

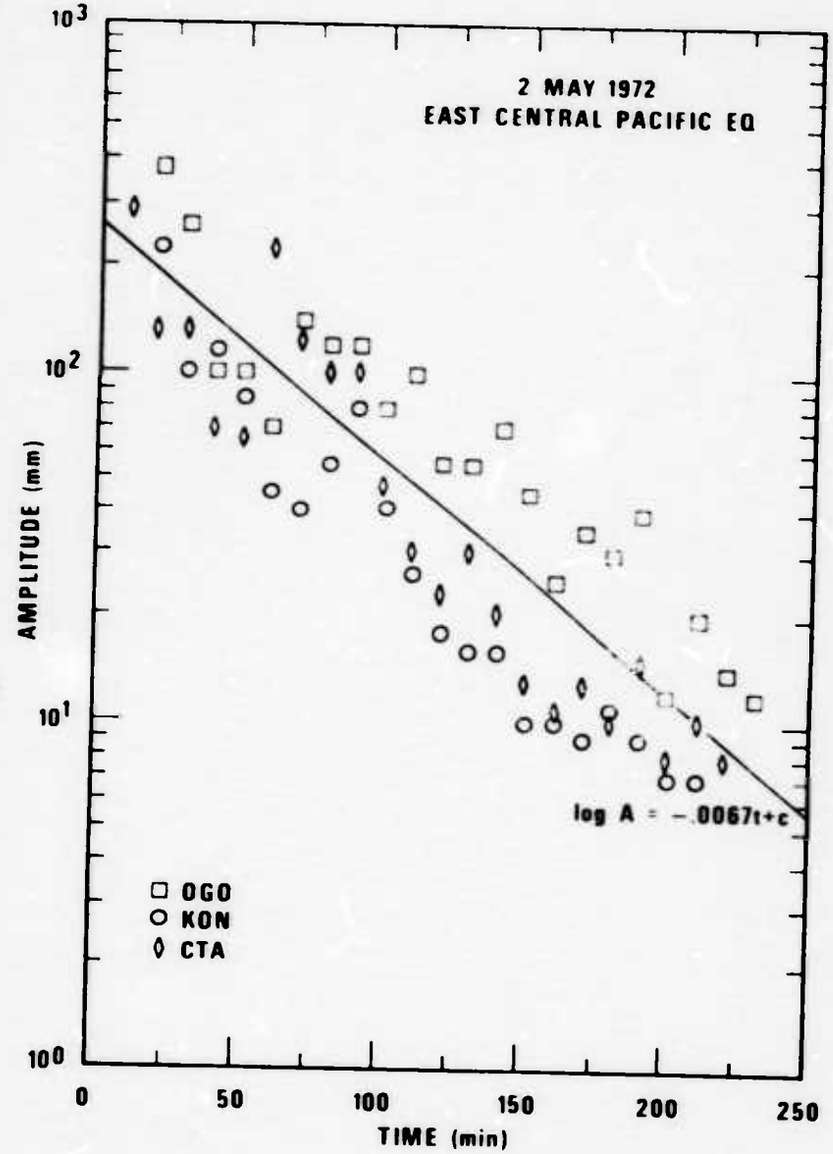

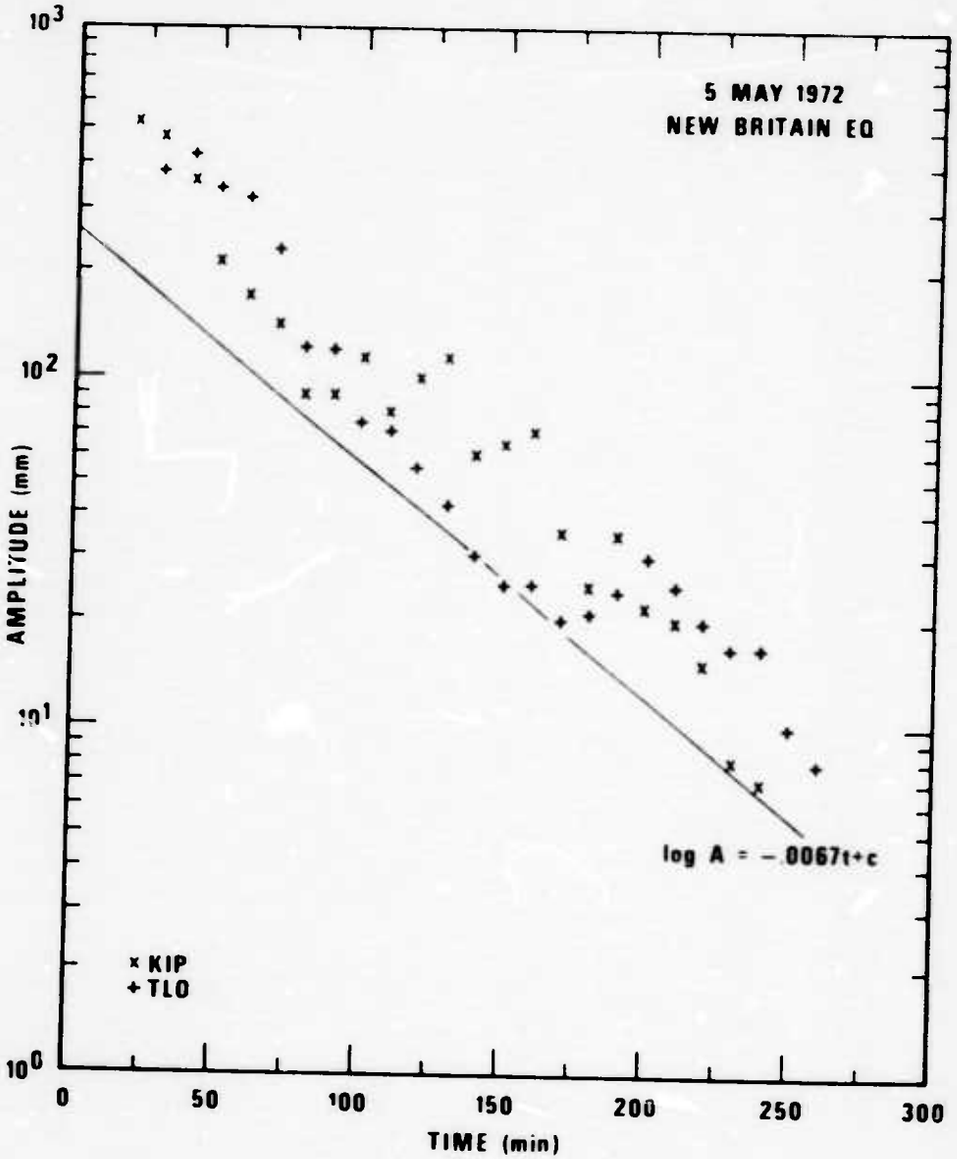

Figure 5. Amplitude versus time after LR onset for large earthquakes (LPE vertical component).

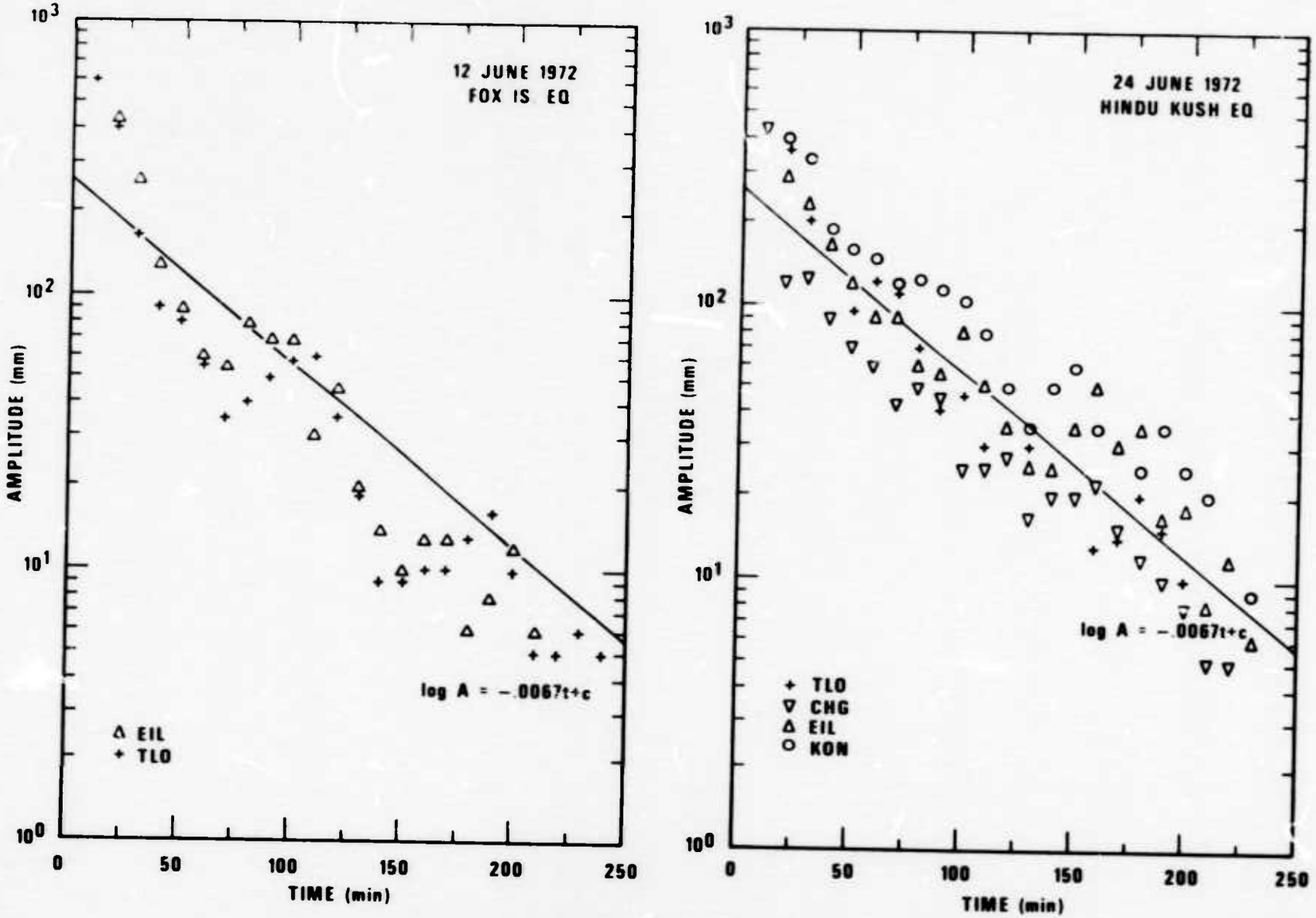

Figure 5. Amplitude versus time after LR onset for large earthquakes (LPE vertical component).

where usually longer periods accompanied the R_2 amplitudes. Using only amplitudes at $\geq$30 minutes and grouping all signals for all events together, a computed regression of $\log_{10}$ A on time in minutes had a slope of -.0067. This line has been drawn on all six figures, and it clearly fits all the coda decays at all times to within a factor of approximately two if it were shifted up or down by an amount appropriate to each of the six signals. Using the decay computed for large events' coda here and the signal shape calculated from smaller events' signals, we are able now to generate signal shapes from LR onset out to several hours if necessary for our simulation of interference problems.

CODA PERIODS

The frequency of coda waves is important since detection of newly-arriving signals depends not only on their amplitude relative to the coda but also their frequency content relative to the coda. Most of the LR signals detected on the LPE network had a visible bandwidth at least from .025 to .05 Hz (von Seggern, 1974). Due to dispersion, the energy in this bandwidth has a characteristic time distribution which further enhances the detectability of LR. Since our signal analysis for this study included reporting of the period at each two-minute interval, we are able to present the relation of dominant period to the coda time. Figure 6 shows plots for typical recordings with high S/N ratio. Again, the zero time is the fundamental LR onset. Note that each of the eight stations is represented and that each of the eight seismic regions is also; so there should be no particular bias to this sample. The salient feature of these plots is that except for a few minutes during the arrival of the fundamental-mode LR at the start and perhaps the arrival of this phase again from the longer great circle path, the dominant period of the signals is quite limited, centered at roughly 20 seconds. This coda characteristic implies that newly-arriving signals from other events should be easily detectable visually if their amplitude is at least as large as that of the coda because of their bandwidth and dispersion. Moreover, if processing is feasible, a narrow notch filter or a low-pass filter with corner at .05 Hz may be helpful in extracting

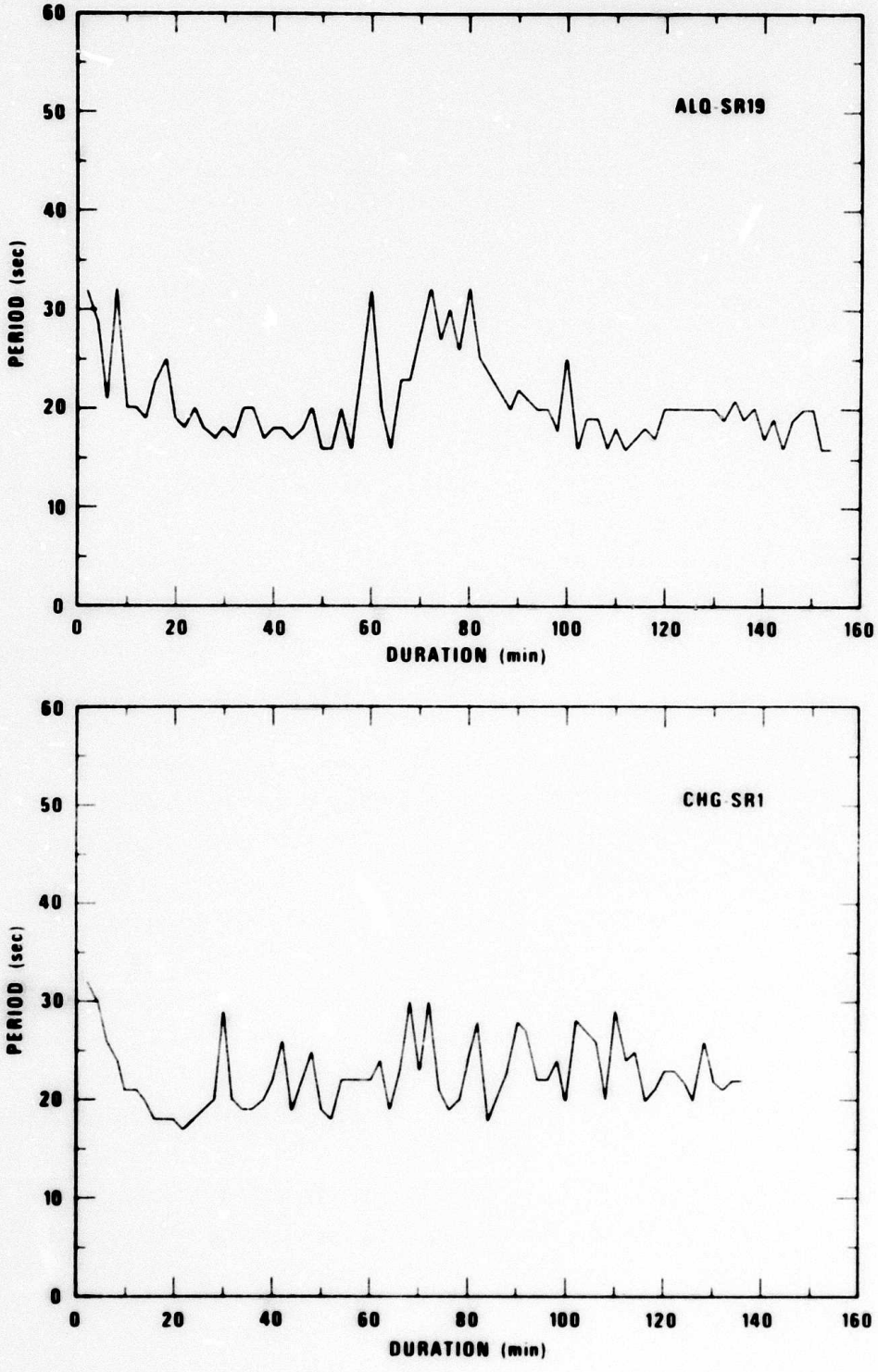

Figure 6. Typical plots of dominant signal period versus time after onset of fundamental-mode LR.

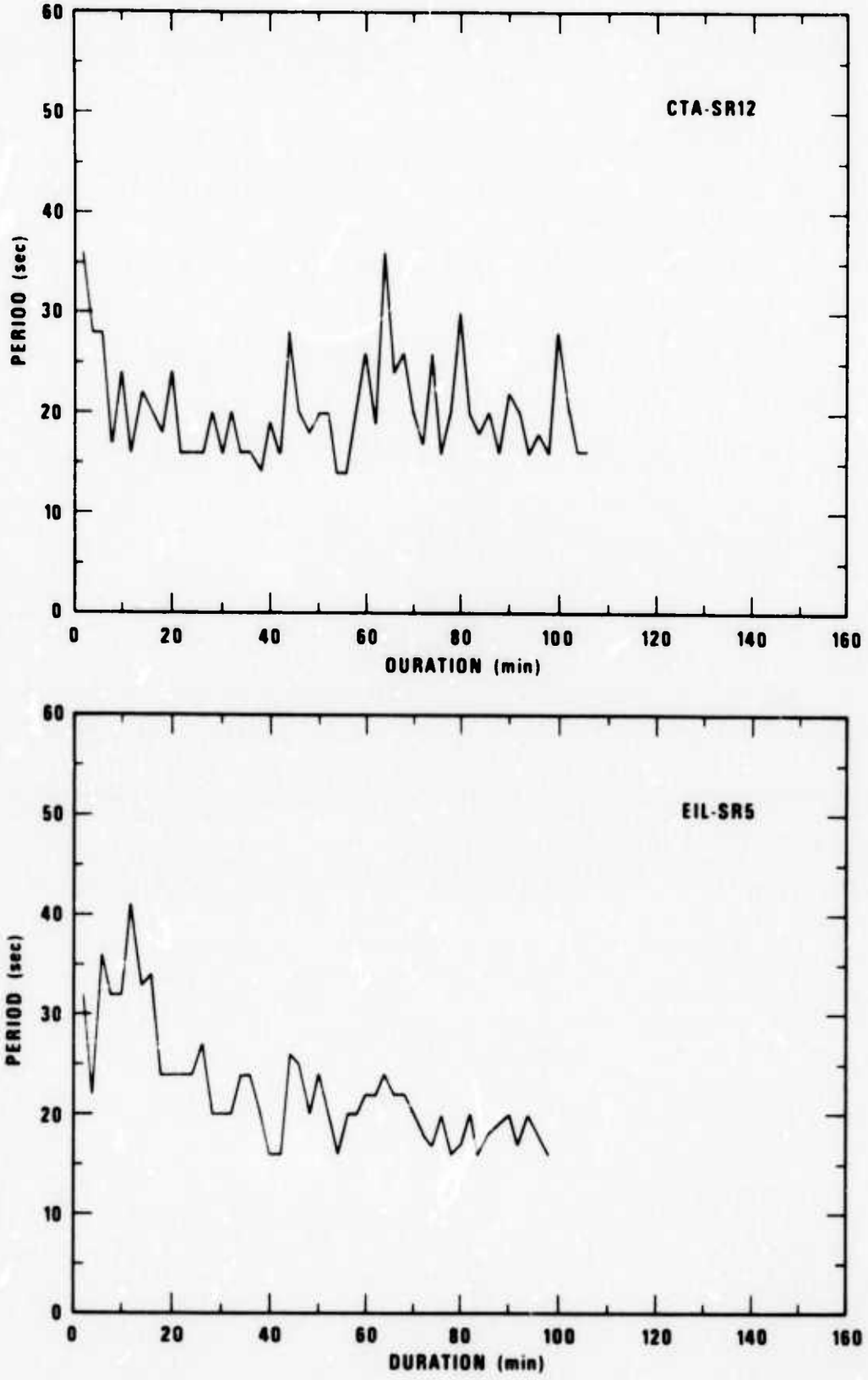

Figure 6. Typical plots of dominant signal period versus time after onset of fundamental-mode LR.

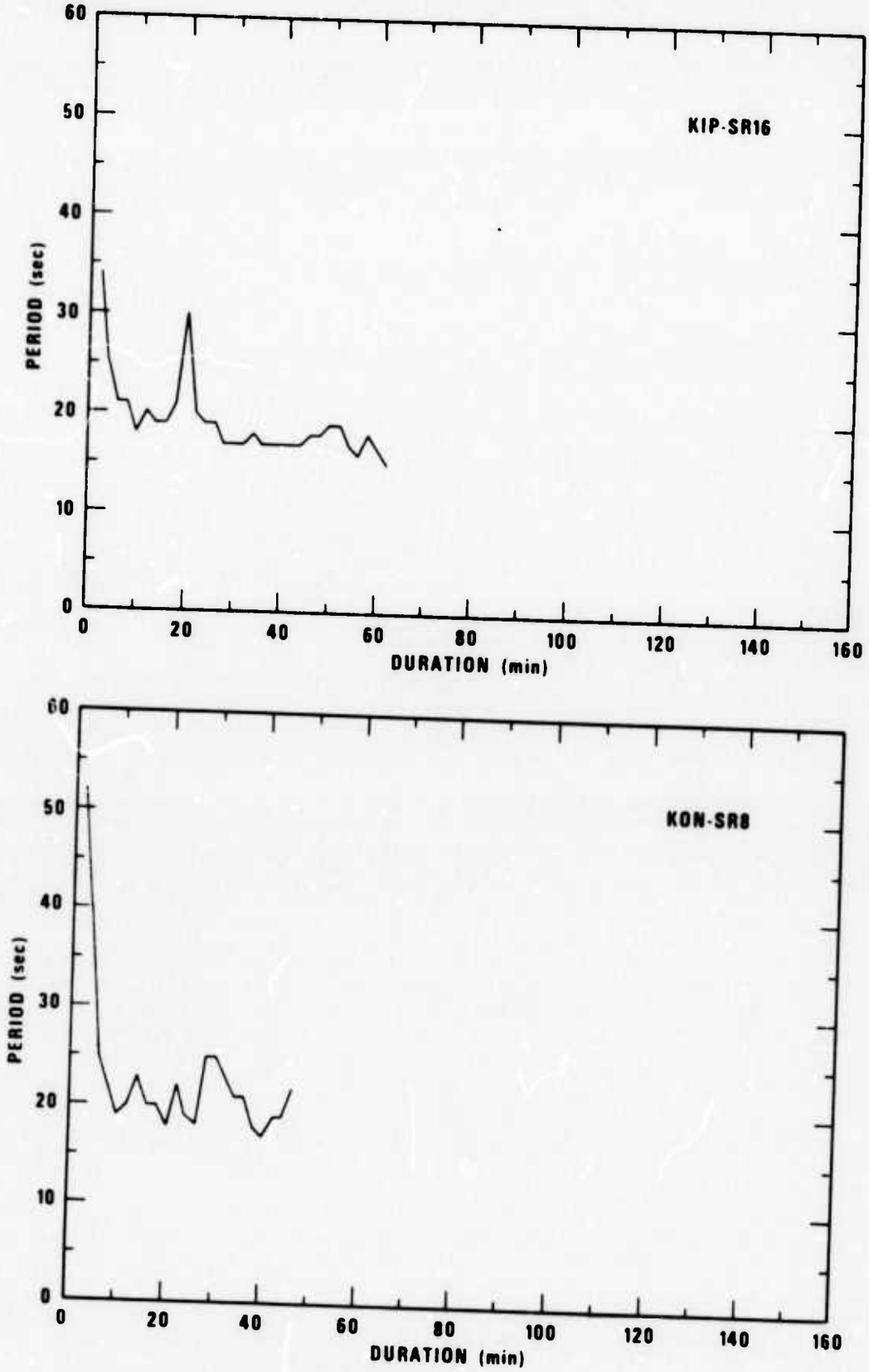

Figure 6. Typical plots of dominant signal period versus time after onset of fundamental-mode LR.

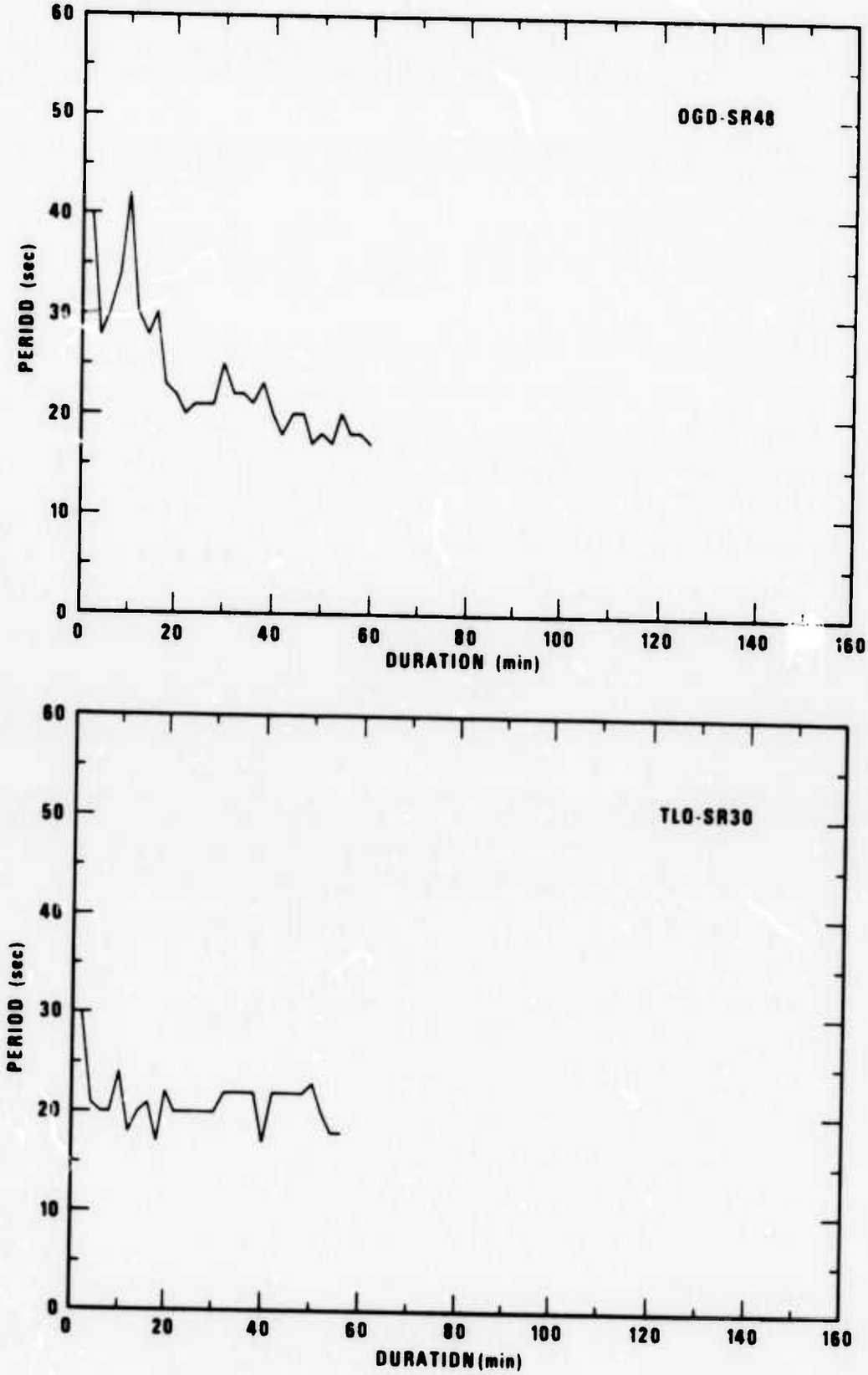

Figure 6. Typical plots of dominant signal period versus time after onset of fundamental-mode LR.

signals from the coda of other events. Because at least 75% of the time span of the signals is dominated by this .05 Hz coda as shown in Figure 5, there is cause for optimism in recovering by digital or analog processing many events which are visually masked within the coda of larger events at single-sensor sites.

Further evidence for this 20-second dominance in coda is obtained from our 17 signals with > 200-minute durations. Out of all the measured periods on these signals, three-fourths were in the range of 18 to 25 seconds. There was no discernable systematic change in period over the duration of these long codas, aside from the lengthening of period often accompanying arrival of R_2. (We note that codas on the low-gain, WWSSN-type responses had predominate periods somewhat shorter, 15 to 20 seconds, than the codas on the high-gain counterparts.)

The fact that the dominant periods in the coda are mostly near 20 seconds allows us to infer an interesting geophysical datum, Q, for this period. Remembering that we found $\log_{10} A \propto -.0067t$ for coda decay, taking the antilog and converting to base e, and then assuming an average 3.2 sec/km group velocity for 20-second LR waves over the glove, we obtain $A \propto \exp(-.000080r)$ where r is in kilometers. Inelastic attenuation of surface waves is commonly expressed as $A \propto \exp(-\pi r/QUT)$ where Q is the quality factor, U is group velocity, and T is period. Now, equating exponents and substituting in our values for U and T, we get $Q \simeq 630$. Note that we have not included the effect of dispersion on amplitudes, a factor proportional to $\Delta^{-1/2}$, and so the present estimate of Q is conservatively low. Other effects must be taken into account; for, clearly, 20-second waves late in the coda must have travelled extremely complex, circuitous paths (albeit, excellent ones for LR propagation) wherein, to be precise, geometrical spreading, mode conversion, and reflection-refraction coefficients would need to be calculated for any theoretical model. But since the arrivals in the coda have these diverse, unknown paths, such effects would be very difficult to quantify; we know only the arrival time of each amplitude measurement and thus the length of the path travelled.

SIMULATION MODEL

We desire to simulate in the time domain the seismic activity seen by typical LPE sites and thus by the network as a whole. Some events will produce signals above the noise level while others will not, according to signal and noise amplitude levels at each particular site. For those signals which are above the noise, clear detection is not guaranteed because of the possibility of signals from other events arriving simultaneously. The purpose of our simulation is to determine what percentage of events at a given magnitude are thus affected when we vary network threshold and configuration. Empirical measures have been reported by von Seggern (1974) for the LPE network, and these empirical results will aid in calibrating our simulation program; that is, we will attempt to reproduce those results, which grew from visual analysis of seismograms, with a simulation model run on the computer before proceeding with other cases.

In the calibration stage it is necessary to run the model with a real epicenter list, in fact the very list with which the LPE data base was formed. But if we are to employ the model for very sensitive networks with thresholds lower than achieved so far in seismology, we must simulate all events that could be detected with even a very small probability since each event, no matter how small, can possibly contribute to the interference problem if it is near a station. No presently available epicenter list has a low enough threshold to assure that all events which might produce observable long-period recordings are entered. (Recordings from the LPE sites typically show five or more events per day than are on the NOS list.) Therefore, in the full simulation, seismic events will be generated by a Monte Carlo technique. In this way, although we are able to create the necessary activity unreported on real epicenter lists, we replace the known pattern of earthquake occurrence in the earth with a random (except for the existence of aftershock sequences) spatial and temporal variation; but this departure from reality should not significantly detract from the utility of the results.

This Monte Carlo procedure is preferable to attempted extrapolations of real earthquake lists to lower magnitudes because seismic activity in each region has its different physical basis resulting in varying seismicity-magnitude relations, aftershock occurrences, and spectral shapes and because any real network has varying thresholds for each seismic region on the globe. Any attempt to faithfully extrapolate present earthquake lists would require so many complex rules and dubious assumptions that the completely random approach that we utilize seems not only more efficient than, but also nearly as realistic as, extrapolation.

GENERAL ASSUMPTIONS FOR THE SIMULATION PROGRAM

We examined no signals for this study from events with hypocenters listed at > 100 km; in fact roughly 80% of the signals are from epicenters at $\leq$ 50 km. Thus no signal characteristics for deep events are available in our data base. In the simulation then, we will ignore non-shallow seismic activity; for our purposes, a cutoff of 60 km will be used. It is possible to do this without significantly underestimating the interference problem because not only do approximately two-thirds of the world's earthquakes occur at $\leq$ 60 km (inferred from the NOS epicenter list) but also these events generate relatively greater surface-wave amplitudes in the 20 to 50 sec period range. In particular, for the 20-second waves which are often maximum visual amplitudes and which dominate the coda, the excitation for sources below 100 km is at least a factor of ten less than for surface or very shallow sources (Harkrider, 1970). Although the median m_b for shallow and deep sources (using 60 km as the dividing point) is nearly equal for the NOS list, the median M_s (without depth correction) would certainly be many tenths lower for the deep earthquakes.

From the incremental graph of von Seggern (1974) for numbers of shallow 1972 earthquakes (with DOF $\leq$ 60 km) at each M_s increment, the seismicity-magnitude relation

$$\log_{10}(N) = 6.902 - .872\ M_s$$

was taken for use in the simulation of earthquake magnitudes by Monte Carlo random drawing. N is the number of events per year with surface-wave

magnitude $\geq M_s$. M_s is the proper magnitude to simulate by Monte Carlo since it relates to signal amplitudes as measured for this study. No events with $M_s < 3.0$ are considered since only rarely are surface waves from an event below 3.0 recorded beyond local or regional distances, where only a few cycles of signal are visible above the background anyway. Clearly, events of $M_s < 3.0$ cannot cause significant interference. The above relation implies an average waiting time of 27 minutes between events with $M_s \geq 3.0$.

It is very important to include aftershocks in our earthquake simulation since aftershocks will produce more mixing-masking incidents than random main events. Shlien and Toksöz (1970) have shown that earthquake lists can be described by a generalized Poisson process wherein a random number of aftershocks (most often zero) is associated with each main shock. This random number of aftershocks is selected from the discrete Z (or Pareto) density:

$$p(n) = \zeta^{-1}(E) \cdot n^{-E}$$

where $\zeta(E)$ is the Riemann zeta function. For n = 1, there is just a main event and no aftershocks. Calculations based on the above density with E = 3.0, a value found for NOS epicenters from 1963 to 1968 by Shlien and Toksöz, predicts that .23 of all earthquakes will be of aftershock nature and .77 will be main shocks. Sadeh and Meidav (1973), applying very liberal aftershock criteria to NOS epicenters from 1964 through 1972, found that roughly 17% of the events were aftershocks so that the true percentage of aftershocks is probably somewhat less. Since the seismicity-magnitude relation given above implies an average waiting time (WT) of 27 minutes between origin times for all events with $M_s \geq 3.0$, the waiting time for main shocks only must be revised upward. The relation

$$27 \leq .77\ (WT_{MS}) + .23\ (WT_{AS})$$

must hold for the average waiting times of main shocks (WT_{MS}) and aftershocks (WT_{AS}). The equality would hold only if WT_{AS} approached zero. Aftershock waiting times are known to vary both with magnitude of the main shock and with time after the main shock (Shlien and Toksöz, 1974); but there is no analysis of aftershock waiting times on general basis known to the author. Consequently, we arbitrarily assumed WT_{AS} to be 15 minutes,

thus making $WT_{MS} \geq 31$ minutes. (In actual simulations, $WT_{MS} = 32$ gave the correct average waiting time of 27 minutes for all events.) Because we regard this average waiting time for aftershocks to be on the low side and because the number of aftershocks seems to be too high in the model of Toksöz and Shlien (1970), we expect to certainly not underestimate the amount of interference on a network when we incorporate aftershocks into our simulation.

Assuming that both main events and aftershock sequences associated with a particular main event occur as Poisson processes, their waiting times are exponentially distributed and can be randomly generated by:

$$WT = WT_{MS} \cdot \ln(1/x) \text{ or } WT = WT_{AS} \cdot \ln(1/x)$$

where x is a random variable drawn from a uniform distribution ($0<x<1$). (If no aftershock sequences are generated, we revert to an average waiting time of 27 minutes as stated above.) Assuming M_s to be distributed according to the above sesimicity-magnitude relation, a random M_s (≥ 3.0) can be generated for main events and aftershocks by:

$$M_s = [\ln(1/x)/(.872 \cdot \ln 10)] + 3.0$$

where x again is randomly drawn from the uniform distribution ($0<x<1$). For aftershocks, we do not allow a randomly generated M_s to exceed that of the main event, and so we continually draw new random $\underline{x}$'s until the required number of aftershocks, n-1, is attained with this constraint. This procedure will make aftershock sequences for small events appear to resemble swarms since we already require that all events have $M_s \geq 3.0$. For location of the main event, random longitude and latitude are generated by:

$$LON = 360x - 180$$

$$LAT = \frac{180}{\pi} \arcsin x$$

where each x is a different random number drawn from the uniform distribution. Another random number x is drawn, and if $x > .5$, the sign of LAT is changed, thus producing an equal number of events in the northern and southern hemispheres.

When a real epicenter list is used in providing sources for the simulation run, a conversion from m_b to M_s must be made for each event since events are routinely assigned m_b but only occasionally M_s. We used

$$M_s = 1.45\ m_b - 2.34$$

a regression computed by von Seggern (1974) using over 3000 M_s-m_b points for global earthquakes.

We have previously discussed our reasons for neglecting the body-wave portion of the seismogram in simulating long-period signals--relative to surface waves, they simply do not occupy much time on typical recordings. As with neglecting deep events and small events, this will tend to cause an underestimation of interference effects. As mentioned previously, these omissions should not seriously bias the results of the simulation program though.

DETECTION WITHOUT INTERFERENCE

By generating spatially and temporally random events and assigning them signal amplitudes and shapes at calculated epicentral distances, we are able to survey a station or network in the simulation program for its response in terms of detections, non-detections, and interference cases. In the case of signal interference, the shapes will be important; but let us first consider the simple response where a signal arrives alone and only amplitude need be considered for detection.

Each station used in the simulation run is assigned a background noise value. This value is the median of the maximum zero-to-peak noise amplitudes (millimicrons) measured in numerous 40-minute windows of seismic background noise (von Seggern, 1974) if an actual LPE site is used or estimated value (50mμ) if a hypothetical site is used. No noise variance is allowed; that is, the background is assumed to remain constant. Signal amplitudes at each site are calculated by:

$$A = T \cdot 10^{M_s - 1.06 \log\Delta - 1.43}$$

where A is a zero-to-peak amplitude (millimicrons), T is assumed to be a constant 20 seconds period, and Δ is distance in degrees. (The M_s formula

implied here is the result of a study of LPE data in von Seggern, 1974.) No signal variance is allowed either; so we do not attempt to model recognized magnitude variation due to radiation pattern and path effects. A signal is declared as detected at a station if its amplitude as calculated above exceeds the background noise amplitude. Thus detection jumps from zero to 100 percent at S/N ratio of 1.0, a value determined by von Seggern (1974) for Rayleigh waves on LPE recordings.

Our restriction of zero noise and signal variance requires some discussion. In a real detection situation, both signal and noise variance contribute to the cumulative normal shape of observed detection curves. Since the rate of seismicity increases with decreasing magnitude, such real detection curves entail many detections at magnitudes lower than the cutoff on the artificial unit-step detection curve which we have assumed for our simulation. Clearly our unrealistic assumption would adversely affect the simulation results for detection and interference if seismic activity were confined to one point on the globe. However, we in fact simulate random activity over the entire globe, and large signal deviations for a given M_s occur naturally at all stations because of the large scatter in distances to events with that M_s. This scatter tends to overwhelm that which would result if we incorporated signal variance for events and noise variance at stations. We therefore conclude that our restriction will not seriously bias the results.

DETECTION WITH INTERFERENCE

If two or more signals interfere, we still check each signal for detection as in the simple non-interference case; however, if each is above the noise level, some additional logic must be employed to decide whether they should be classified as "mixed" or "masked" rather than "detected." In a real situation many events which would be detected when arriving alone must be relegated to the mixed or masked category by the analyst. The simulation program must emulate the analyst's logic as closely as possible. This is a formidable problem since the situations in which events interfere form an

extensive and varied fabric to which the analyst applies visual criteria, often vague and intuitive, in deciding whether a particular event is seen or not. This contrasts with the fairly straightforward decision process when an event arrives singly. The simulation program must apply algorithms with quantified decision levels to signals which are also well quantified. Clearly, it is in this case now that signal shape will be important.

The dependence of signal shape on epicentral distance was previously presented. We concluded that this dependence was rather weak; nevertheless in the simulation, distance dependence is crudely modelled in that a signal is assigned parameters p_1, p_2 and p_3 equal to values at 15°, 60°, and 135° on the straight lines in Figures 2a, 2b, and 2c, depending on which distance range (0-30°, 30-90°, or 90-180°) the station fell in. Note that for the p_i values there is a large scatter which we do not choose to model; we will return to this matter later. Since we often need to generate signals with durations longer than those measured for signal shape and since we have shown that the latter part of signal codas can be reasonably approximated by an exponential decay, we model that part of the coda beyond 30 minutes after LR onset by the decay relation computed for the 17 large magnitude events:

$$\log_{10}A - \log_{10}A_o = -.0067\ (t-30)$$

where A_o is the amplitude calculated at 30 minutes and t is the time in minutes after LR onset. Since the maximum of the signal envelope is tied to M_s and thus the calculated maximum amplitude at the station, amplitude in millimicrons at any point in the signal can easily be calculated by scaling the peak of the signal envelope to this maximum amplitude.

A check on the validity of our signal shapes in the simulation model can be made by comparing the durations of simulated signals with real ones. Figure 3 presented signal duration versus maximum amplitude for the real events that were measured for signal shape. A preliminary run of the simulation program was made, with signals modelled as described above, to produce a similar body of data, shown in Figure 7. The straight-line visual fit to the data of Figure 3 is reproduced here, and also the general extent of the Figure 3 data is shown by a dashed perimeter. The simulated durations (that

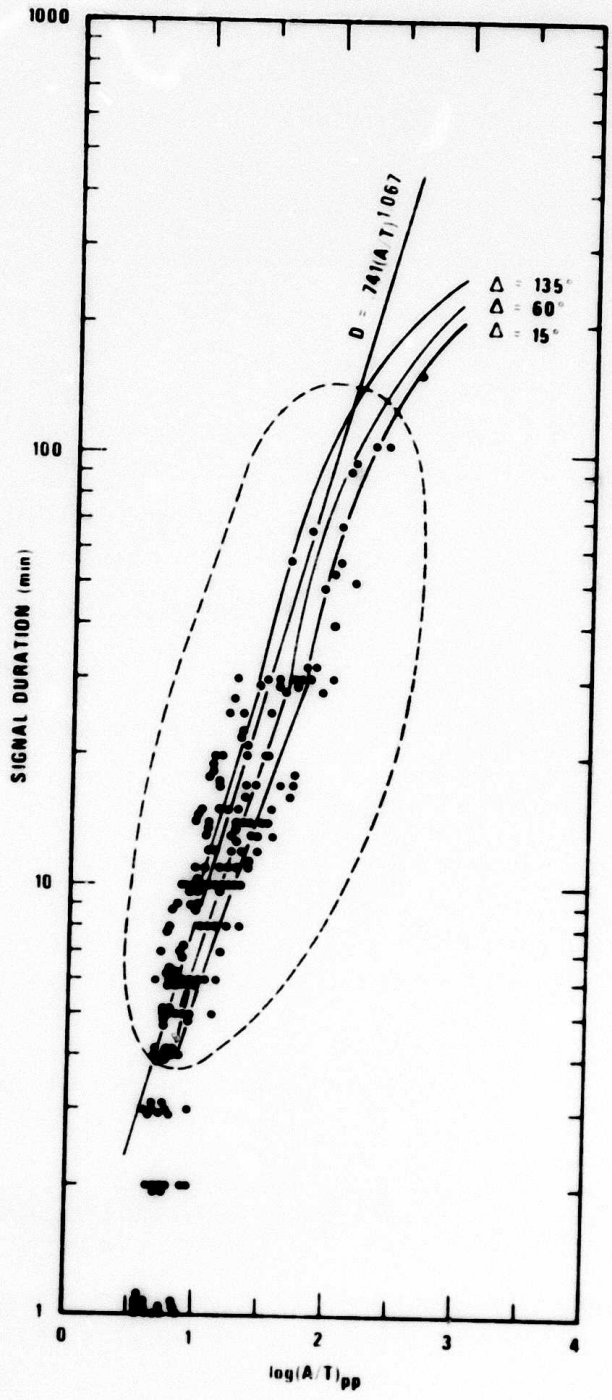

Figure 7. Relationship of signal duration to maximum amplitude of the signal (simulated data).

time for which the signal exceeds the noise) are consistent with the real data although they necessarily have less scatter due to definite constraints on the parameters in the signal shapes generated by the program and lack of signal and noise variance in the simulation.

The three curves on Figure 7 result from calculations of signal durations through the amplitude-time functions assumed in the simulation program. The shape of the signal is governed by different relations for time less than and greater than thirty minutes, and so there is a derivative discontinuity at this time for the three curves. The derivation of the duration-amplitude relations shown is as follows. We first establish the time t_m of the maximum amplitude of the signal shape given earlier by taking the derivative:

$$\frac{d}{dt} \log_{10} [A(t)] = p_1[(1-e^{p_2 t_m})(p_3 e^{p_3 t_m}) + (e^{p_3 t_m})(-p_2 e^{p_2 t_m})].$$

Equating to zero and solving for t_m gives

$$t_m = \frac{1}{p_2} \ln \left(\frac{p_3}{p_2 + p_3} \right).$$

Using the values of p_i at 15°, 60°, and 135° gives t_m = 1.69, 1.89, and 2.35 for these distances. For durations less than thirty minutes, the relation between the amplitude $A(t_c)$ in the signal at any time after the time of the maximum amplitude $A(t_m)$ is:

$$\log_{10} [A(t_c)/A(t_m)] = p_1(1-e^{p_2 t_c})\, e^{p_3 t_c} - p_1(1-e^{p_2 t_m})\, e^{p_3 t_m}.$$

The term $e^{p_2 t_c}$ can be neglected for any times $t_c > t_m$. One can solve for the time at which $A(t_c)$ falls to the noise level, by definition the duration of the signal, if we set $A(t_c)$ equal to the noise level, which is roughly an average of 50 mμ zero-to-peak for the LPE stations used in the simulation of the data of Figure 7. Since we are plotting durations versus peak-to-peak $A(t_m)$ in Figure 7, we assume a period T of 20 seconds and use 100 mμ for the noise level. With these assumptions, the solution for t_c is obtained as:

$$t_c = \frac{1}{p_3} \ln \left[\frac{1}{p_1}\left(.700 - \log \frac{A(t_m)}{T}\right) + (1-e^{p_2 t_m})e^{p_3 t_m}\right].$$

Using the values of p_i and t_m stated above results in the portions of the curves in Figure 7 up to thirty minutes' duration. For longer durations, the long-term coda relation established earlier must be used in conjunction with the short-term relation. The long-term relation is again:

$$\frac{A(t_c)}{A(30)} = 10^{-.0067(t_c-30)}.$$

Multiplying this by the short-term A_c/A_m ratio given above and neglecting $e^{p_2(30)}$ results in:

$$\log_{10}\left[A(t_c)/A(t_m)\right] = p_1 e^{30p_3} - p_1(1-e^{p_2 t_m})e^{p_3 t_m} - .0067(t_c-30).$$

Again, we allow $A(t_c)$ to approach 100 mμ and let T=20; solving then for t_c gives:

$$t_c = 149\left[\log \frac{A(t_m)}{T} + p_1(e^{30p_3} - e^{p_3 t_m} + e^{(p_2+p_3)t_m}\right] - 74.$$

Using the same values of p_i and t_m as above produces the portions of the three curves in Figure 7 for durations greater than thirty seconds. The actual durations "observed" from the simulation run lie outside these curves in some instances simply because the noise level at each station was different from 50 mμ zero-to-peak. Overall, the calculated duration-amplitude relations in Figure 7 do not violate the real data of Figure 3, and no real data was available to confirm our prediction of a reduction in the slope of the duration-amplitude relation for very large events with maximum A/T > 1000.

The durations in Figure 7 do not, as mentioned previously, reflect the observed scatter in durations of actual signals. This is due to the constraints of the p_i which we have made for the purpose of limiting computational time of the simulation program. With the three sets of p_i's used for three distance ranges, the program can preset the three corresponding signal shapes and merely scale them up or down according to the current event M_s; but if

the p_i's are allowed to assume statistical variations, the signal shape for each signal above the noise level needs to be computed. We did make one simulation run, however, to test the effect of varying the p_i's to more closely model actual variability in signal shape. In this run each signal above the noise level was assigned a p_1, p_2, and p_3 composed of a term equal to the value on the straight lines in Figures 2a, 2b, and 2c at the proper distance plus a random term reflecting the statistical distribution of points vertically about a point on the line in these figures. This distribution was assumed to be normal in each case, with the mean on the line and with standard deviations of .45, 1.0, and .020 for p_1, p_2, and p_3, respectively. (No positive values of p_1, p_2, or p_3 were allowed though; they were reset to small negative values if this occurred.) This refined model was used for the first thirty minutes of signal only; the constant -.0067 exponential decay for the long-term codas was retained without variation. The simulation run with variable signal shapes resulted in roughly 20% more mixing and masking, and consequently fewer detections, than a run identical in every respect except that signal shapes were constrained to the three sets of constant p_i's for three distance ranges. However, the required computer run time was quadrupled. We do not feel that the refined modelling justifies this increase in expenditure, and the results given in this report will be for the constrained model of signal shapes.

We now refer to the logic for mixed and masked events presented on the simulation program flowchart in Figure 8b. The first steps of the program are charted in Figure 8a and have already been discussed. At this point we qualitatively define a "mixed" event as one whose signal overlaps the signal of one or more other events (considering only those parts of the signal which exceed the background noise) and which is detected in some imperfect sense such that measurement of period and amplitude would be uncertain due to the interference. We qualitatively define a "masked" event as one whose signal exceeds the background noise for some time interval but which is effectively concealed by another signal arriving at that time; this does not require that the amplitude of the masking signal exceed that of the masked signal at every point. The "mixed-masked" logic in Figure 8b is an attempt to emulate

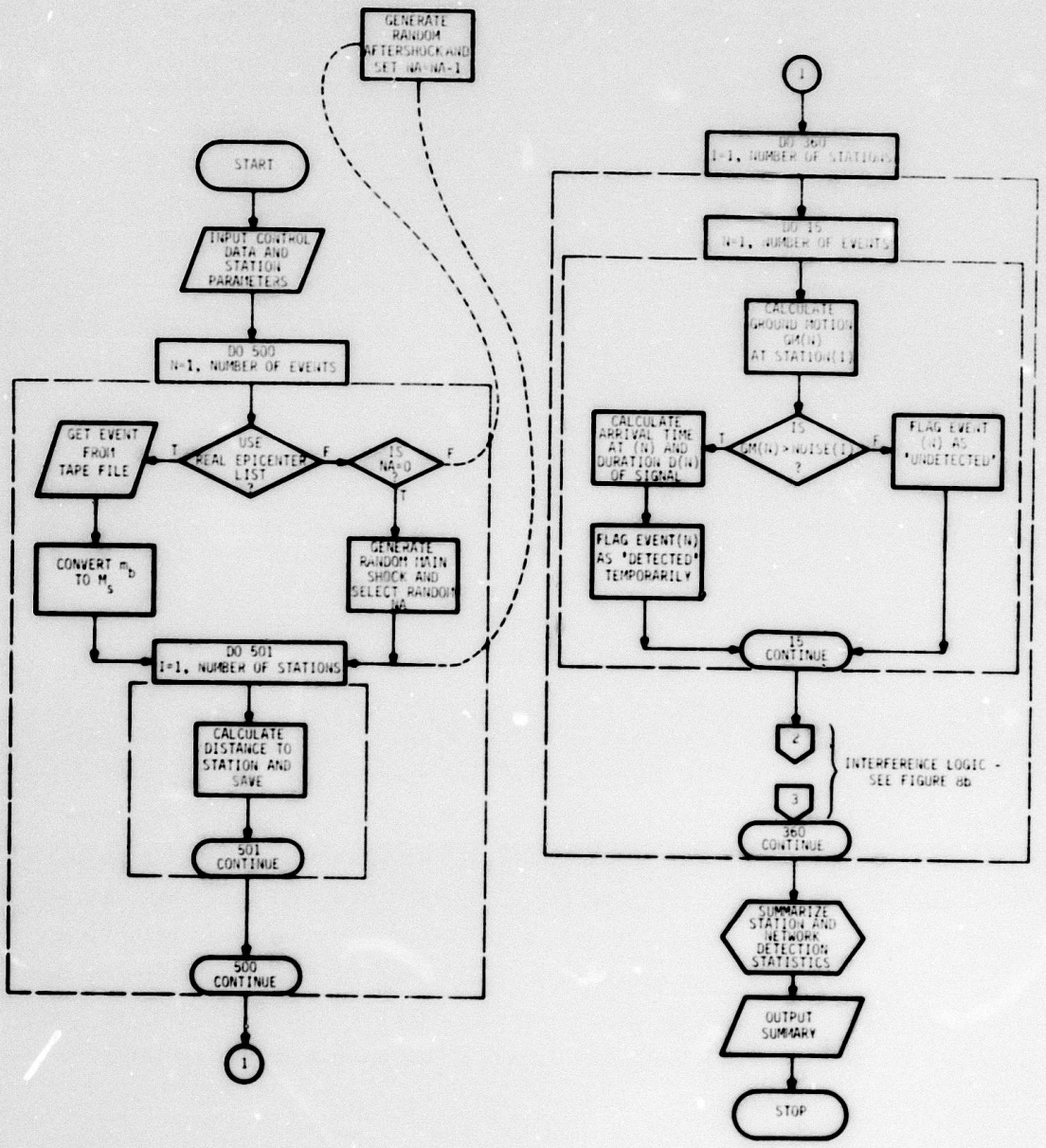

Figure 8a. Flowchart of the program for simulating interference on long-period networks.

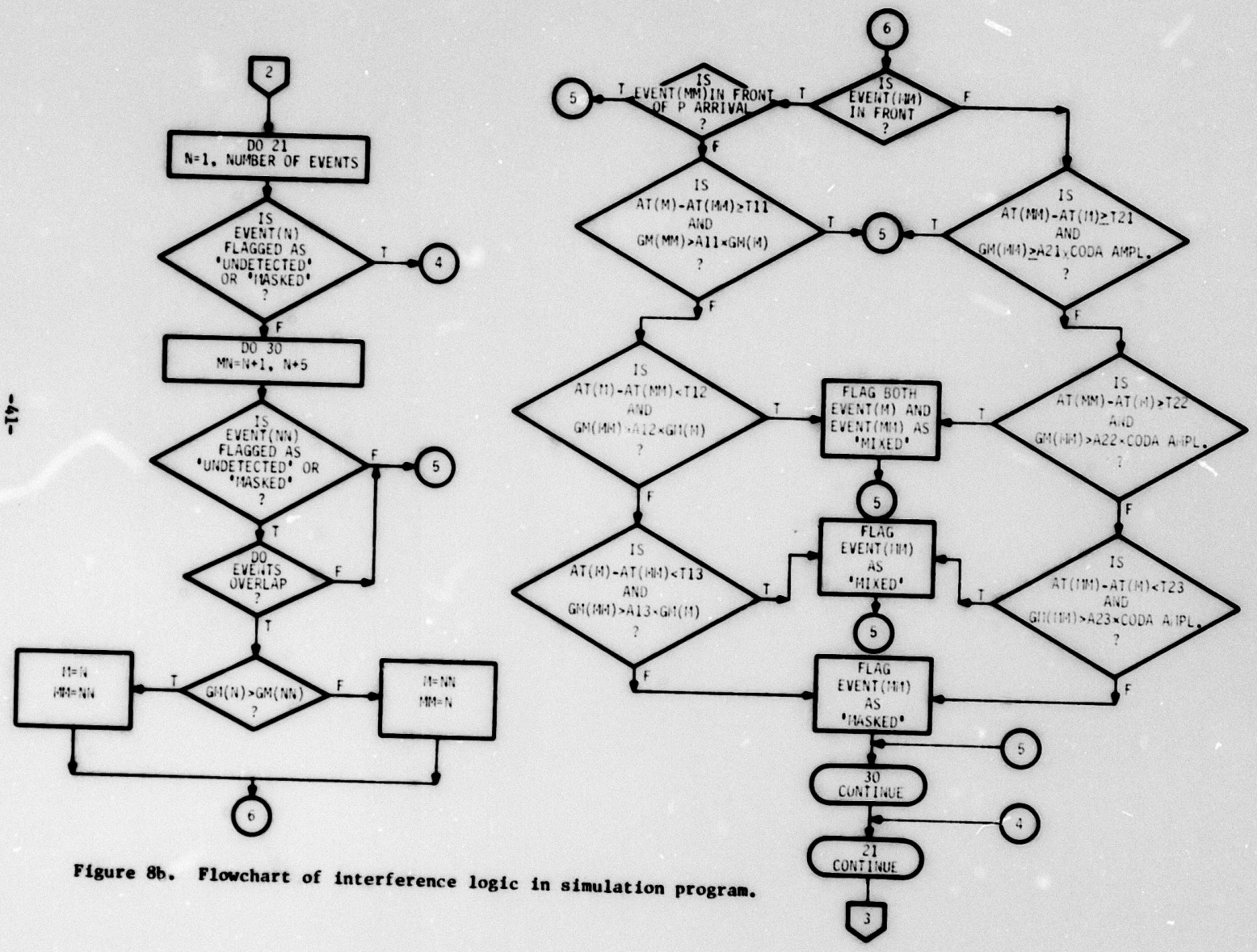

Figure 8b. Flowchart of interference logic in simulation program.

classification of mixed and masked events by a human observer. The exact values used in these logical tests were set by calibrating the simulation model against real data, as will be described in the next section. The decision logic is more graphically shown in Figure 9. Note that all possible occurrences are covered by the logic and that in order to simplify the logic we use rectangular decision areas, thereby requiring $T_{11} = T_{12} = T_{13}$, $T_{21} = T_{22} = T_{23}$, $A_{11} = A_{13}$, and $A_{21} = A_{23}$. A more realistic approach would employ curves to separate the decision areas, but we regard this refinement as not only indeterminable but also unnecessary.

CALIBRATING THE SIMULATION MODEL

Using a real data base of 611 signals, we have devised a functional representation of the signal envelope for long-period Rayleigh waves and their coda. We have checked the durations of signals generated in the model against those of real signals. We have assumed reported seismicity-magnitude, M_s-m_b, and amplitude-distance relations based on empirical data. We have set up a logical scheme which hopefully emulates the decisions of a human observer when he encounters possible interference on long-period recordings. Now we simply seek to match the amount of mixing and masking reported by the simulation program to that reported by analysts working with the LPE data as a final step in composing the working program. This involves determining the factors in the logic scheme of Figure 9.

For our calibration data, the month of January 1972 was selected from the LPE data base (von Seggern, 1974). Statistics on the number of events detected, mixed, and masked for stations and for the network are compiled. The simulation program was run on the same events, yielding similar, but artificial, statistics. The parameters T and R in the logic of Figure 9 were varied until satisfactory agreement, to within approximately 20%, was attained between the real and simulated results; the simulation results for mixed and masked percentages were purposely left low relative to the real percentages since deep events and body waves are not considered in the simulation. The parameter values set in this manner were:

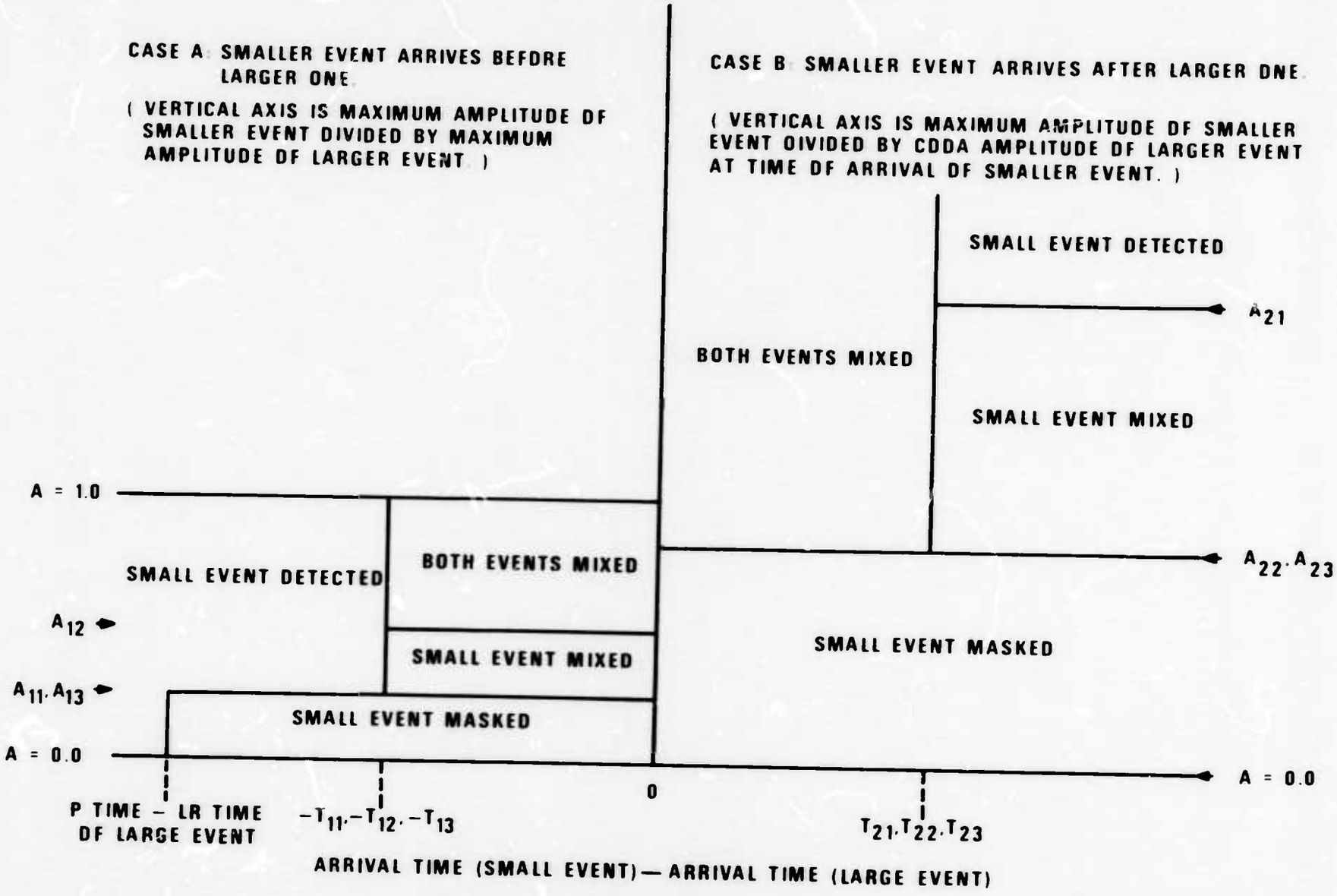

Figure 9. Graphical display of detected-mixed-masked decision logic.

$T_{11} = T_{12} = T_{13} = 6$ minutes,

$T_{21} = T_{22} = T_{23} = 8$ minutes,

$A_{11} = A_{13} = .25$,

$A_{12} = .5$,

$A_{21} = 2$,

$A_{22} = A_{23} = 1.$

Admittedly, this is not a unique set of parameter values; and other combinations of significantly different values, or even a change in the basic decision logic, could perhaps provide equally satisfying agreement between the simulated and empirical data. For example, decreasing the time constants by two or three minutes or changing the amplitude constants by 50% does not greatly affect the results of the simulation, but time constants of 1 minute or amplitude constants twice as large gave unsatisfactory results. However, the above set of values provides satisfactory agreement and has the property of being physically reasonable.

Before proceeding, we also need to check the seismicity-magnitude graph of the simulated data against the relation used in generating M_s values since the addition of aftershock sequences may significantly distort this relation. In Figure 10 we present sets of simulated data in the form of incremental graphs of number of events versus M_s. It can be seen that for the simulation with no aftershocks, the agreement with the seismicity-magnitude relation is very good over the entire range while for the simulation including aftershocks the resulting numbers are somewhat too high at the lowest magnitudes and somewhat too low at the intermediate magnitude due to a concentration of aftershocks toward the lower magnitudes. Even for the simulation with aftershocks, the variance of the points from the underlying relation is not considered to be significant though, and a line fit through these points would not differ much from the given one.

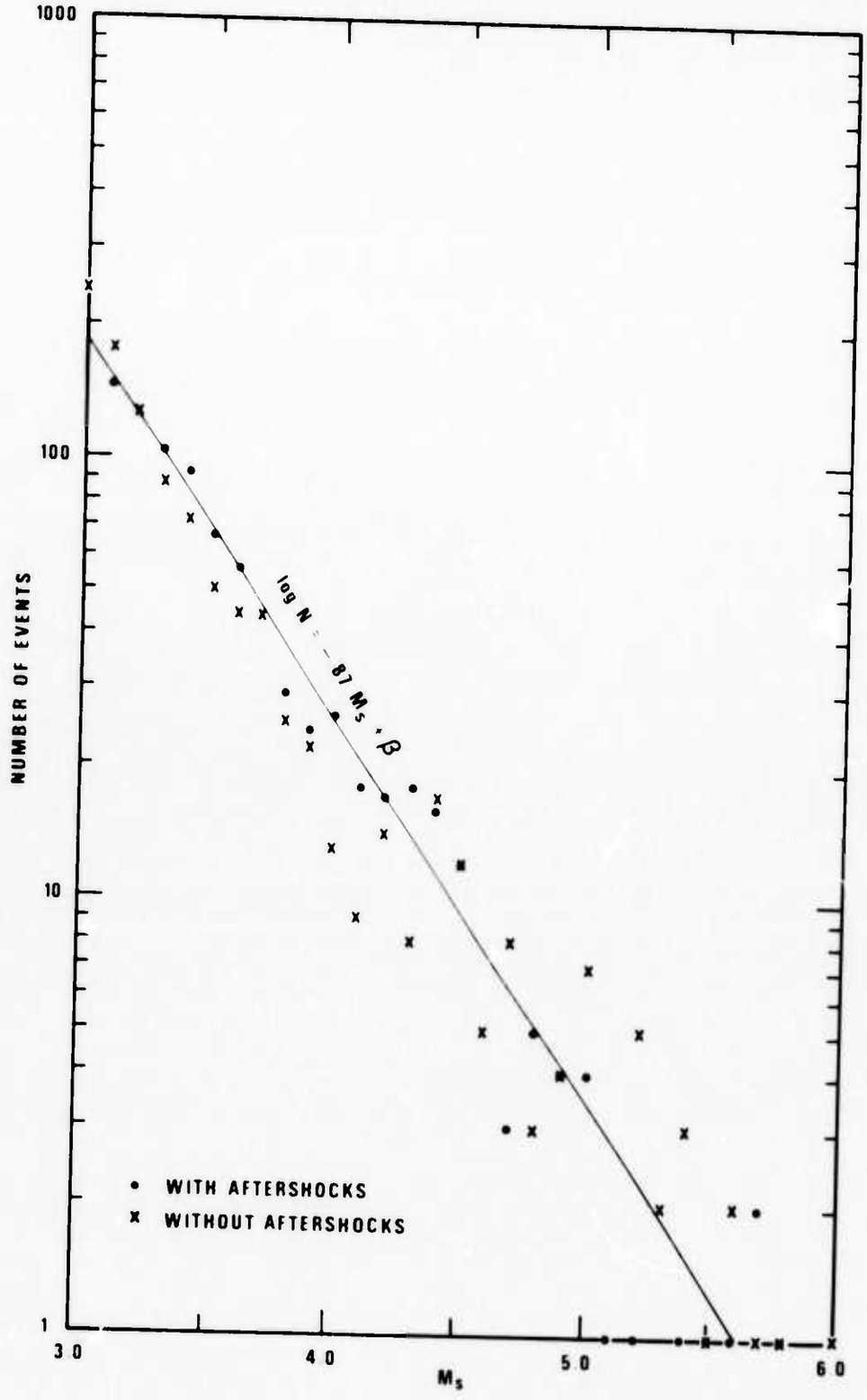

Figure 10. Seismicity-magnitude plots of simulated earthquake bulletins.

SIMULATION RESULTS

Using values as previously defined for all the parameters in the program for simulating network interference, we proceeded to obtain results for hypothetical networks. Five such arbitrary networks were considered; 5, 10, and 20-station global networks and 5 and 10-station northern-hemisphere networks. The 20 stations of which all these networks are comprised are listed in Table V. Note that each network covers the globe (or northern hemisphere) somewhat evenly. Ten of the locations in Table V are presently LPE sites; eight of the remaining ten were or are WWSSN sites.

The simulation results for the five networks are summarized in Table VI. Here "station" results are averaged over all the stations in a particular network. The categories, "detected", "mixed", and "masked", have been defined for a station, but not as yet for a network. By "detected" on a network, we here mean that $\geq$ two stations of the network declared a clear detection; by "mixed" that $\geq$ two stations declared a detection, clear at none or at most one station and mixed at the remainder; by "masked" that either at least one station reported the event as masked if only one station reported a detection (mixed or clear) or at least two stations reported the event as masked if no station reported detection (mixed or clear). In other words, the network reports an event as mixed if signal interference hindered it from having at least two clear station detections, and it reports an event as masked if more severe interference hindered it from having at least two detections of any sort. (We mention that in the real detection situation, there is no way of knowing absolutely whether an arrival one might choose to report as masked would have been detected under normal background conditions. The simulation program is artificial in this sense then: it knows a priori what events, when interferred with, would have been detected without interference. On the other hand, the real data is imperfect since the "masked" label will be arbitrarily applied. (The number of reported masked events in the LPE data exceeded the number of truly masked events because the analysts routinely called an arrival masked if its $m_b \geq 4.0$ and $\Delta \leq 100°$ and if a signal from another event was present. A crude adjustment to the empirical data was made in calibrating the simulation program by noting the observed

TABLE V

Station Locations Used in the Simulation

Station Code	Location	Latitude	Longitude
AFI	Afiamalu, Samao Islands	13.9S	171.8E
ALQ	Albuquerque, New Mexico	34.9N	106.5W
CHG	Chiang Mai, Thailand	18.8N	99.0E
CTA	Charters Towers, Australia	20.1S	146.3E
DAV	Davas, Philippines	7.1N	125.6E
EIL	Eilat, Israel	29.3N	34.5E
FBK	Fairbanks, Alaska	64.9N	148.0W
KIP	Kipapa, Hawaii	21.4N	158.0W
KON	Kongberg, Norway	59.6N	9.6E
MAT	Matsushiro, Japan	36.5N	138.3E
MFP	Fernando Poo, Cameroon	3.3N	8.7E
NDI	New Delhi, India	28.6N	77.2E
OGD	Ogdenburg, New Jersey	41.1N	74.6W
PRE	Pretoria, South Africa	25.7S	28.2E
PSC	Easter Island, Pacific Ocean	27.1S	109.4W
SBA	Scott Base, Antarctica	77.9S	166.8E
SJG	San Juan, Puerto Rico	18.1N	66.1W
SOM	Sombrero, Chile	52.8S	69.2W
TOL	Toledo, Spain	39.9N	4.0W
ZLP	La Paz, Bolivia	16.3S	68.1W

5-station global network: CTA, EIL, FBK, PRE, ZLP

5-station northern hemisphere network: CHG, EIL, FBK, KIP, SJG

10-station global network: ALQ, CHG, CTA, EIL, FBK, MAT, PRE, PSC, SBA, ZLP

10-station northern hemisphere network: ALQ, CHG, DAV, EIL, FBK, KIP, KON, MAT, OGD, SJG

20-station global network: all

TABLE VI

Simulation Results for Hypothetical Networks

Network Type	Thresholds	Station Statistics in Percent									Network Statistics in Percent							
		50% thresholds	$M_s \geq 3.0$ D	$M_s \geq 3.0$ X	$M_s \geq 3.0$ M	$M_s \geq 3.0$ U	$M_s \geq 3.5$ D	$M_s \geq 3.5$ X	$M_s \geq 3.5$ M	$M_s \geq 3.5$ U	50% thresholds	$M_s \geq 3.0$ D	$M_s \geq 3.0$ X	$M_s \geq 3.0$ M	$M_s \geq 3.0$ U	$M_s \geq 3.5$ D	$M_s \geq 3.5$ X	$M_s \geq 3.5$ M	$M_s \geq 3.5$ U
Without Aftershocks																			
5-station N. hemi.	normal	3.9	21.9	1.3	2.1	74.7	52.3	2.9	4.6	40.2	3.7	25.4	1.3	2.2	71.1	67.0	3.7	5.1	24.2
10-station N. hemi.	normal	3.9	19.0	0.9	1.4	78.7	46.8	2.1	3.2	47.9	3.6	30.2	0.8	2.2	66.8	74.6	1.4	3.1	20.9
5-station global	normal	3.8	22.1	1.3	2.4	74.2	53.0	3.1	5.1	38.8	3.7	23.6	1.3	1.9	73.2	65.6	3.7	5.4	25.3
10-station global	normal	3.9	20.4	1.0	1.8	76.8	50.2	2.6	4.0	43.2	3.5	31.8	1.6	1.9	64.7	82.3	3.4	3.4	10.9
20-station global	normal	3.9	19.0	0.9	1.5	78.6	47.5	2.3	3.3	46.9	3.4	42.3	0.8	3.2	53.7	92.4	1.4	3.1	3.1
5-station N. hemi.	low	3.4	44.2	6.1	12.5	37.2	75.6	8.6	13.8	2.0	3.2	59.2	6.8	17.6	16.4	88.4	5.4	6.2	0.0
10-station N. hemi.	low	3.5	40.3	4.8	9.4	45.5	73.3	7.9	11.8	7.0	3.1	68.8	5.0	12.6	13.6	93.0	3.1	3.9	0.0
5-station global	low	3.4	44.7	6.4	13.1	35.8	75.0	9.1	13.9	2.0	3.2	58.7	6.7	18.4	16.2	87.9	5.9	6.2	0.0
10-station global	low	3.5	42.4	5.5	10.8	41.3	74.4	8.8	12.9	3.9	3.1	75.1	4.9	14.0	6.0	93.5	4.2	2.3	0.0
20-station global	low	3.5	40.5	4.8	9.3	45.4	73.9	8.3	12.3	5.5	2.9	83.8	5.4	9.8	1.0	94.9	2.8	2.3	0.0
With Aftershocks																			
5-station N. hemi.	normal	3.8	19.3	1.1	2.1	77.5	53.8	2.6	4.9	38.7	3.6	22.2	1.5	2.4	73.9	68.8	3.9	6.8	20.5
10-station N. hemi.	normal	3.9	16.4	0.8	1.5	81.3	46.9	2.1	3.6	47.4	3.6	26.5	1.3	2.0	70.2	77.3	2.6	4.9	15.2
5-station global	normal	3.8	19.4	1.2	2.3	77.1	53.4	2.8	5.6	38.2	3.6	20.9	1.0	1.9	77.2	67.9	3.2	5.8	23.1
10-station global	normal	3.8	17.7	1.0	1.8	79.5	50.0	2.3	4.5	43.2	3.5	26.7	0.8	1.7	71.8	81.5	1.9	4.2	12.4
20-station global	normal	3.9	16.5	0.7	1.5	81.3	47.1	1.9	3.9	47.1	3.4	34.8	1.6	3.1	60.5	90.9	1.3	3.9	3.9
5-station N. hemi.	low	3.4	38.7	6.4	12.7	42.2	74.8	9.5	14.4	1.3	3.2	50.8	9.4	19.5	20.3	85.7	7.2	7.1	0.0
10-station N. hemi.	low	3.5	34.6	5.2	9.7	50.5	72.2	8.7	12.9	6.2	3.1	59.2	7.5	16.5	16.8	89.3	4.9	5.8	0.0
5-station global	low	3.5	38.8	7.0	13.3	40.9	74.4	10.2	14.0	1.4	3.2	49.3	9.7	17.7	23.3	86.4	5.2	8.4	0.0
10-station global	low	3.5	36.7	5.9	11.0	46.4	73.7	9.2	14.1	3.0	3.1	64.8	8.7	16.7	9.8	91.2	3.9	4.9	0.0
20-station global	low	3.5	35.0	5.2	9.4	50.4	73.4	9.0	13.1	4.5	3.0	76.5	7.9	13.7	1.9	92.9	3.9	3.2	0.0

D-detected (does not include mixed)
X-mixed
M-masked
U-undetected (does not include masked)

detection probability at a given magnitude and multiplying the number of reported masked events by this factor to get an estimate of the number of truly masked events.)

The event sample size in the simulation runs was 1000, whether or not aftershocks were included. Although the event sets were completely different for both event simulation models, the ten network runs in Table VI for each model were made beginning with the same random number; that is, all ten networks "looked" at exactly the same set of 1000 events in each case. The results with "normal" thresholds are for when the background noise values were set as previously stated; and the "low" threshold results are for when these noise values are reduced by a factor of three, a reasonable possibility if small arrays replaced the single seismometers at each site. Cumulative detection results have been computed using both a M_s = 3.0 and a M_s = 3.5 cutoff. Recall that events with M_s = 3.0 were the lowest magnitude epicenters generated in the simulation; and M_s = 3.5 is approximately equivalent to a m_b = 4.0 earthquake using the M_s-m_b formula given previously in this report.

The percentages of mixed and masked events in Table VI are somewhat less than to be expected with real detection due to reasons previously mentioned: 1) deep events are not simulated, 2) the body-wave portion of the seismogram is not included in the simulation, and 3) masking in the simulation run is declared only if the event was detectable under normal conditions.

Also the percentage of mixed and masked events is almost always higher, as expected, for the case where aftershocks are included in the model. Those instances where they are not is due to the fact that the event sets are completely different for the two cases, and 1000 events is not enough to smooth out statistical fluctuations of the sample. As noted before, we choose an aftershock model which we believed produced more events closely spaced in time and location than real seismic activity and a main shock model which is completely random in time and location; thus the results for the cases with aftershocks in Table VI should more or less approach the real situation. Anyway, the relative amounts of mixing and masking in the various simulation runs should be meaningful even if their absolute amount is somewhat in error.

In regard to the results in Table VI then, we note the following:

1) The station statistics (actually an average over all stations in the network under consideration) are stable. This is as expected since all stations in all five networks are roughly of equal capability.
2) Between 5% and 8% of the events with $M_s \geq 3.5$ ($m_b \geq 4.0$) will not be clearly detected at a typical LPE long-period site due to interference. (These percentages should be somewhat higher for detection of real events.) If station thresholds were lowered by .5 M_s, the corresponding percentage would be between 20% and 24% while the number of detections would be roughly 50% greater.
3) Although a seismic network detects more events as its size is augmented, the number of mixed and masked events is apparently decreased; this is due to the fact that, with more stations, there are more chances for events (provided they are not aftershocks) to be separated sufficiently in arrival time for detection.
4) There is no significant difference between a global network and a more limited network in the northern hemisphere in regard to overall detection thresholds and numbers of mixed or masked events.
5) When stations thresholds are decreased by 0.5 M_s, the number of mixed and masked events reported by a network does not increase significantly for $M_s \geq 3.5$; and the interference problem prevents all of the simulation networks with low thresholds from achieving 100% detection down to $M_s = 3.5$. However, for $M_s \geq 3.0$, lower thresholds cause a considerable increase in network mixed and masked events due to the greater number of events between 3.0 and 3.5 (64.5% of the randomly generated events had $3.0 \leq M_s < 3.5$.

CONCLUSIONS

Long-period interference is a significant problem which is not accounted for in conventional station or network capability estimates, such as by program NETWORTH at the SDAC. Interference depends on the magnitude, shape, and duration of the seismic signals, which vary considerably depending on path and station. Nonetheless, a reasonably accurate model of signal interference can be programmed by parameterizing average coda shapes and durations. Such a program can be calibrated against real data and then utilized to predict interference effects on proposed networks. In this way we were able to predict that neither augmenting a network of stations nor lowering the thresholds at its stations will cause an increase in the number of mixed and masked events above a certain M_s even though more are detected above this M_s. Lowering the station thresholds will produce more mixed and masked events as this M_s cutoff is decreased though; on the other hand augmenting the network will not cause a similar effect at these lower M_s values. Clearly, when M_s thresholds are pushed lower and lower, there will be more and more mixed and masked events to be sorted out since the number of events increases with decreasing magnitude. A long-period system which is designed to sort out these interferring events and which works well at current threshold levels may well be overwhelmed when thresholds are lowered considerably.

REFERENCES

Alsup, Stephen A., and David G. Lambert, 1973: A random model for half-amplitude decay times of Rayleigh waves, Special Report No. 4, Extended Array Evaluation Program, Texas Instruments, Dallas, Texas.

Flinn, E. A., and Eric R. Engdahl, 1965: A proposed basis for geographical and seismic regionalization, Rev. of Geophys., v. 3, pp. 123-149.

Harkrider, David G., 1970: Surface waves in multilayered elastic media.II. Higher mode spectra and spectral ratios from point sources in plane layered earth models, Bull. Seismol. Soc. Amer., v. 60, pp. 1937-1988.

Mack, H., and H. C. Robertson, 1973: Detection threshold of the LASA, ALPA, NORSAR long-period network, SAAC Report No. 10, Teledyne Geotech, Alexandria, Virginia.

Sadeh, Dror S., and Meir Meidav, 1973: Search for sidereal periodicity in earthquake occurrences, J. Geophys. Res., v. 78, pp. 7709-7716.

Shlien, Seymour, and M. Nafi Toksöz, 1974: A compound Poisson-Markov model of earthquake occurrences, submitted to Geophys. J. R. Astro. Soc.

Shlien, Seymour, and M. Nafi Toksöz, 1970: A clustering model for earthquake occurrences, Bull. Seismol. Soc. Amer., v. 60, pp. 1765-1788.

von Seggern, D. H., 1974: Final report on the analysis of recordings from the Very Long Period Experimental stations, Teledyne Geotech, Alexandria, Virginia.

APPENDIX

Normalized plots of amplitudes of Rayleigh-wave signals and coda recorded at LPE sites

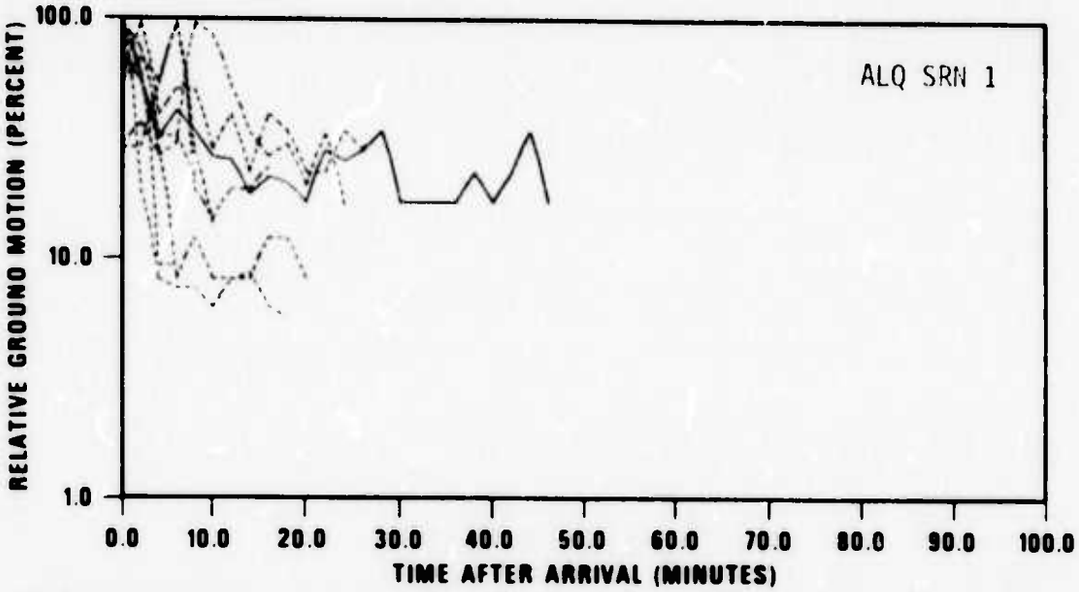
ALQ SRN 1
RELATIVE GROUND MOTION (PERCENT)
100.0
10.0
1.0
0.0
10.0
20.0
30.0
40.0
50.0
60.0
70.0
80.0
90.0
100.0
TIME AFTER ARRIVAL (MINUTES)

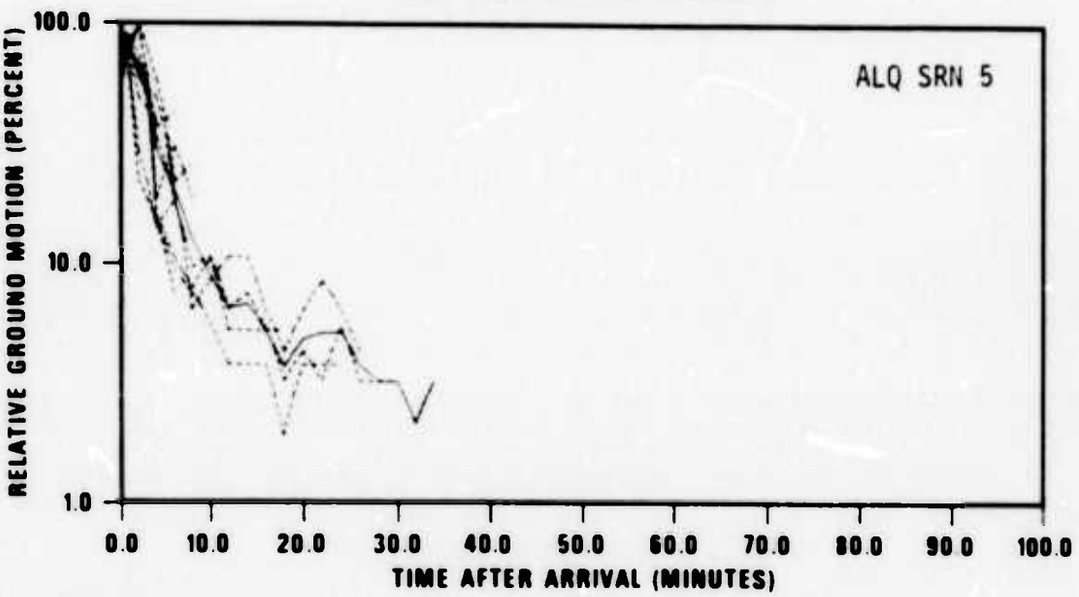
ALQ SRN 5
RELATIVE GROUND MOTION (PERCENT)
100.0
10.0
1.0
0.0
10.0
20.0
30.0
40.0
50.0
60.0
70.0
80.0
90.0
100.0
TIME AFTER ARRIVAL (MINUTES)

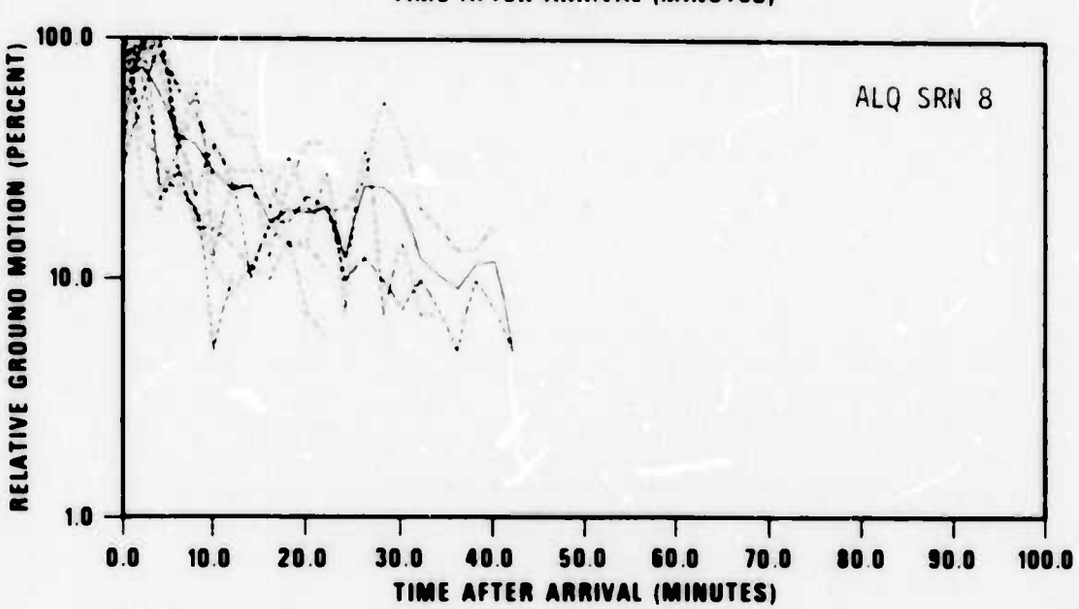
ALQ SRN 8
RELATIVE GROUND MOTION (PERCENT)
100.0
10.0
1.0
0.0
10.0
20.0
30.0
40.0
50.0
60.0
70.0
80.0
90.0
100.0
TIME AFTER ARRIVAL (MINUTES)

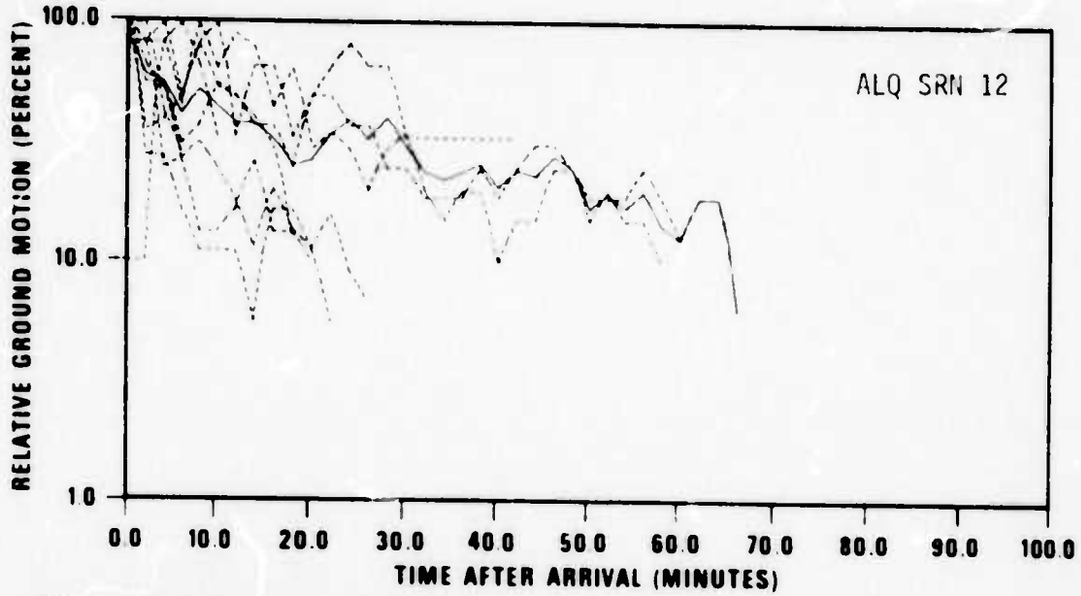
ALQ SRN 12
RELATIVE GROUND MOTION (PERCENT)
100.0
10.0
1.0
0.0
10.0
20.0
30.0
40.0
50.0
60.0
70.0
80.0
90.0
100.0
TIME AFTER ARRIVAL (MINUTES)

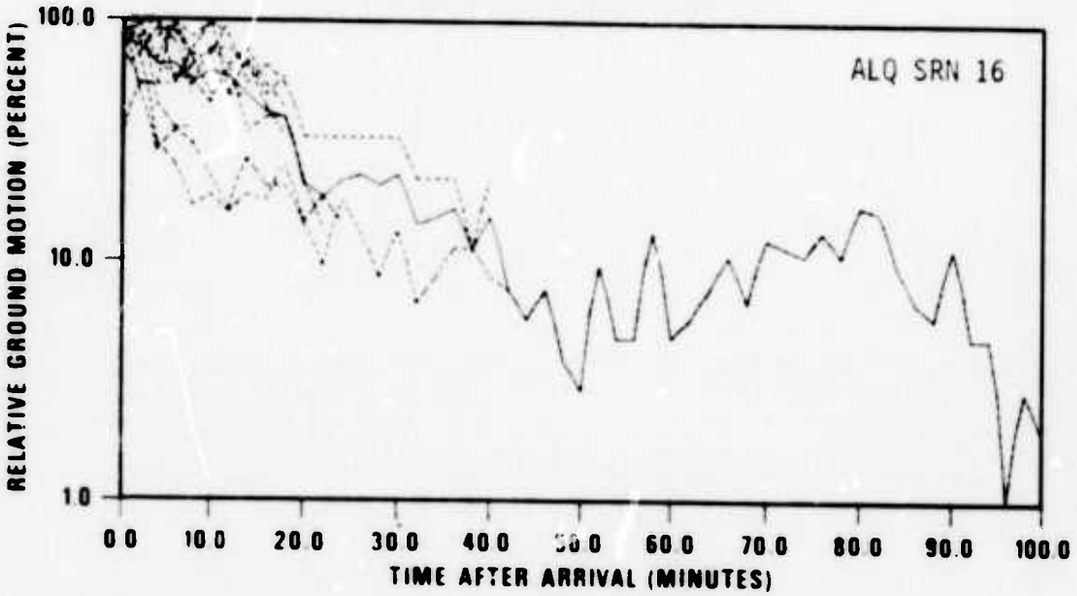
ALQ SRN 16
RELATIVE GROUND MOTION (PERCENT)
100.0
10.0
1.0
0.0
10.0
20.0
30.0
40.0
50.0
60.0
70.0
80.0
90.0
100.0
TIME AFTER ARRIVAL (MINUTES)

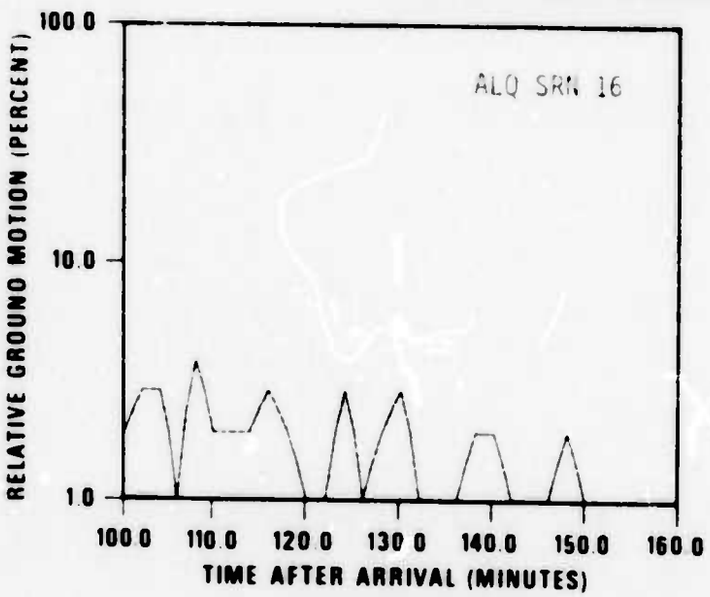
ALQ SRN 16
RELATIVE GROUND MOTION (PERCENT)
100.0
10.0
1.0
100.0
110.0
120.0
130.0
140.0
150.0
160.0
TIME AFTER ARRIVAL (MINUTES)

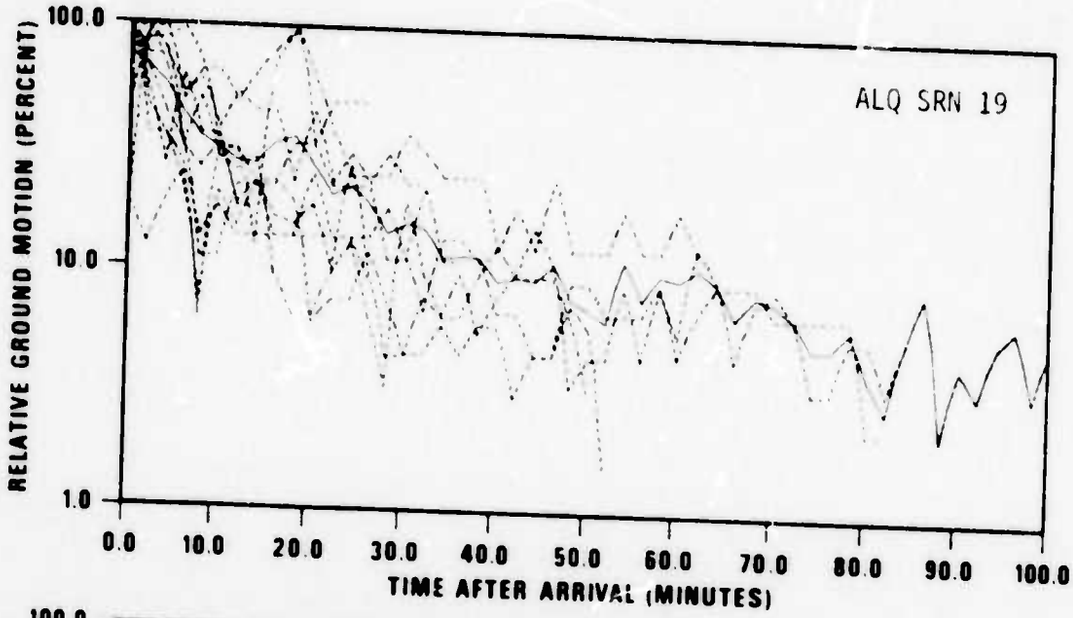
ALQ SRN 19
RELATIVE GROUND MOTION (PERCENT)
100.0
10.0
1.0
0.0
10.0
20.0
30.0
40.0
50.0
60.0
70.0
80.0
90.0
100.0
TIME AFTER ARRIVAL (MINUTES)

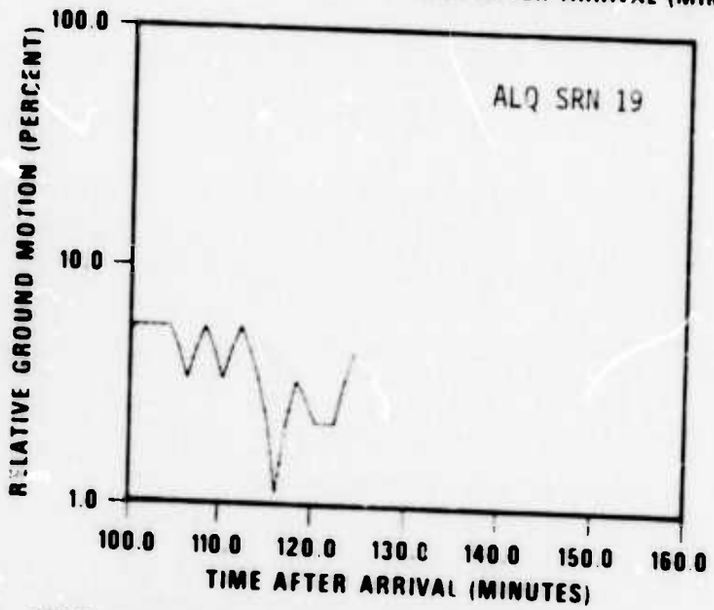
ALQ SRN 19
RELATIVE GROUND MOTION (PERCENT)
100.0
10.0
1.0
100.0
110.0
120.0
130.0
140.0
150.0
160.0
TIME AFTER ARRIVAL (MINUTES)

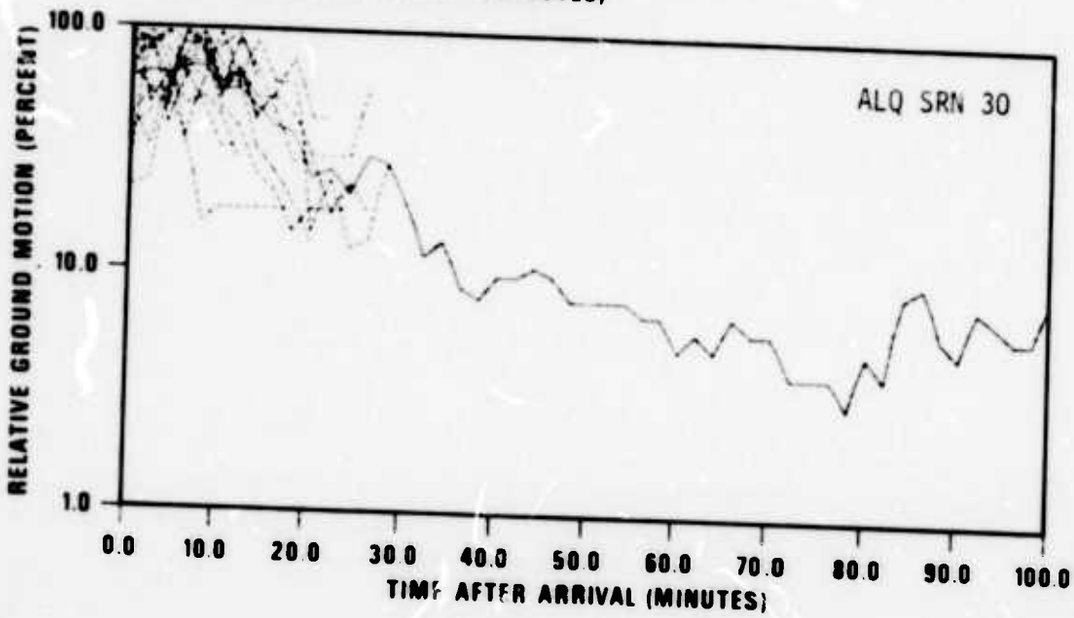
ALQ SRN 30
RELATIVE GROUND MOTION (PERCENT)
100.0
10.0
1.0
0.0
10.0
20.0
30.0
40.0
50.0
60.0
70.0
80.0
90.0
100.0
TIME AFTER ARRIVAL (MINUTES)

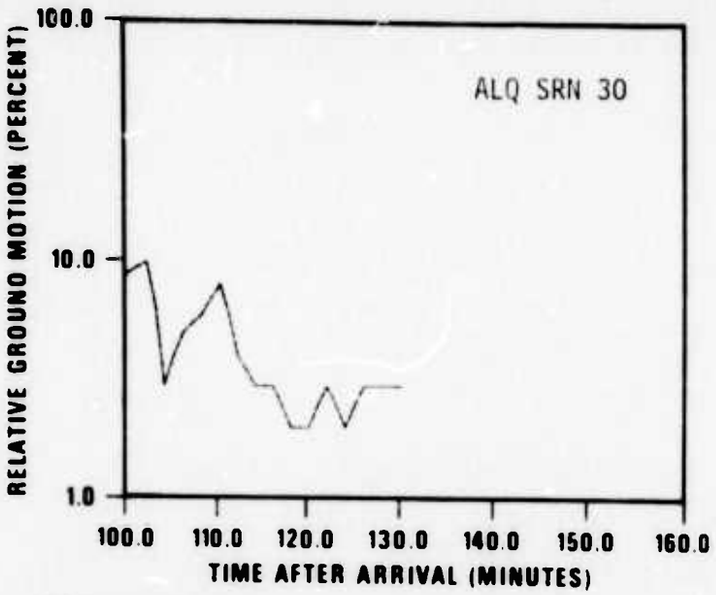
ALQ SRN 30
RELATIVE GROUND MOTION (PERCENT)
100.0
10.0
1.0
100.0 110.0 120.0 130.0 140.0 150.0 160.0
TIME AFTER ARRIVAL (MINUTES)

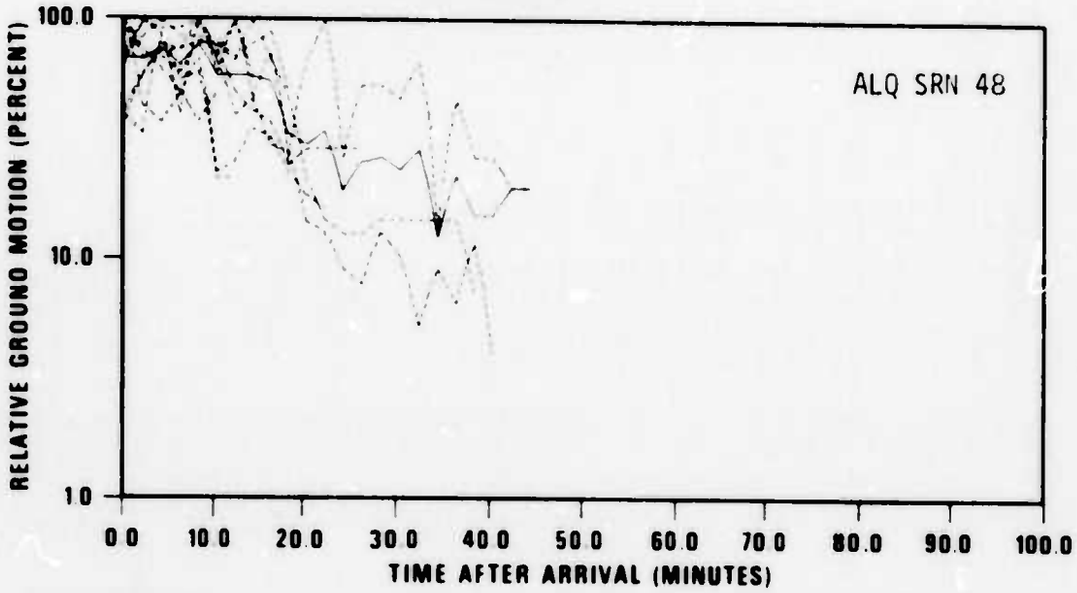
ALQ SRN 48
RELATIVE GROUND MOTION (PERCENT)
100.0
10.0
1.0
0.0 10.0 20.0 30.0 40.0 50.0 60.0 70.0 80.0 90.0 100.0
TIME AFTER ARRIVAL (MINUTES)

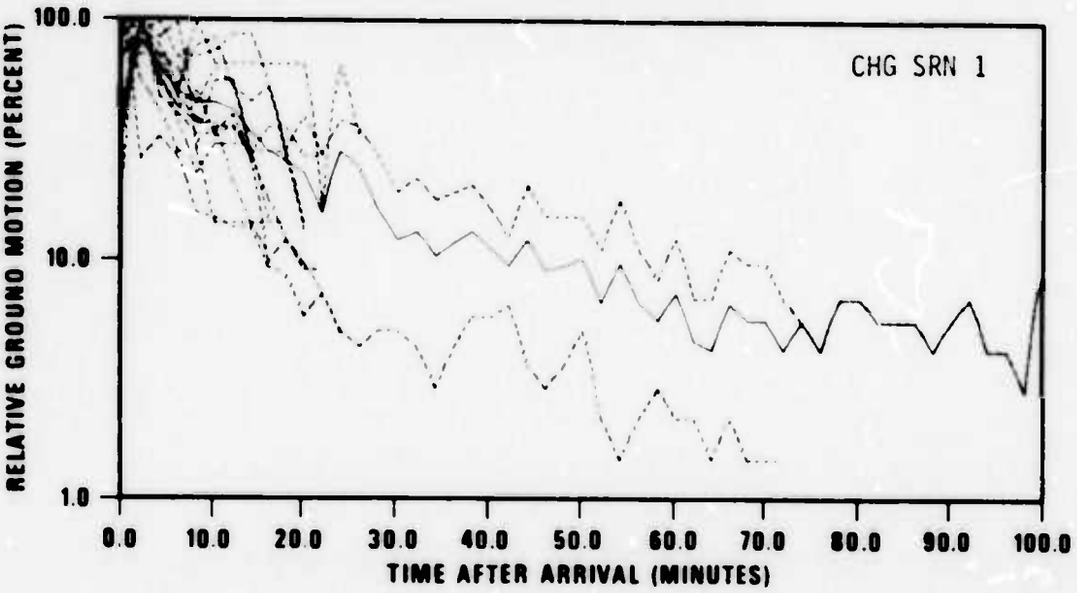
CHG SRN 1
RELATIVE GROUND MOTION (PERCENT)
100.0
10.0
1.0
0.0 10.0 20.0 30.0 40.0 50.0 60.0 70.0 80.0 90.0 100.0
TIME AFTER ARRIVAL (MINUTES)

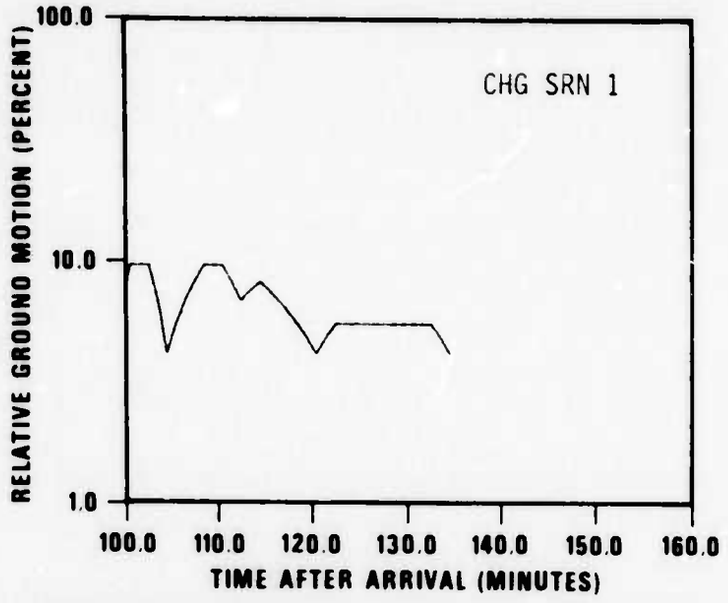
CHG SRN 1
RELATIVE GROUND MOTION (PERCENT)
100.0
10.0
1.0
100.0
110.0
120.0
130.0
140.0
150.0
160.0
TIME AFTER ARRIVAL (MINUTES)

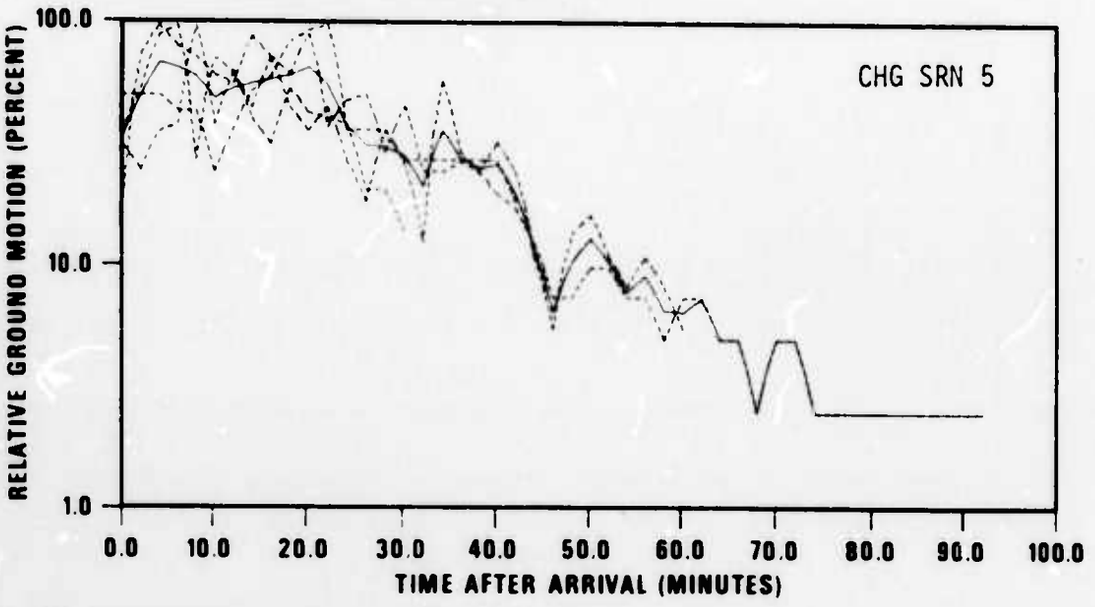
CHG SRN 5
RELATIVE GROUND MOTION (PERCENT)
100.0
10.0
1.0
0.0
10.0
20.0
30.0
40.0
50.0
60.0
70.0
80.0
90.0
100.0
TIME AFTER ARRIVAL (MINUTES)

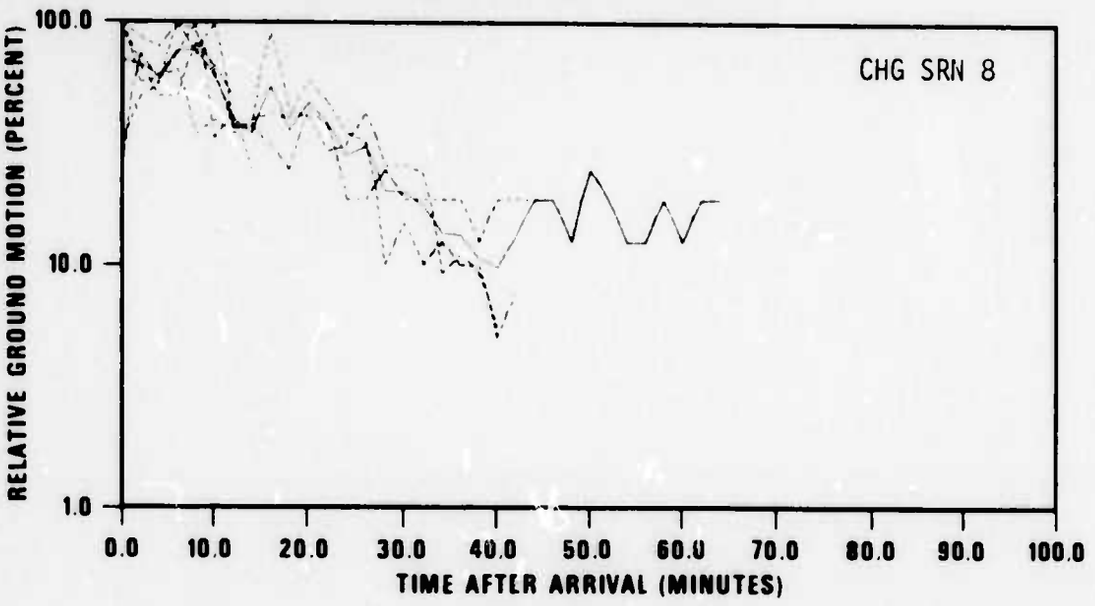
CHG SRN 8
RELATIVE GROUND MOTION (PERCENT)
100.0
10.0
1.0
0.0
10.0
20.0
30.0
40.0
50.0
60.0
70.0
80.0
90.0
100.0
TIME AFTER ARRIVAL (MINUTES)

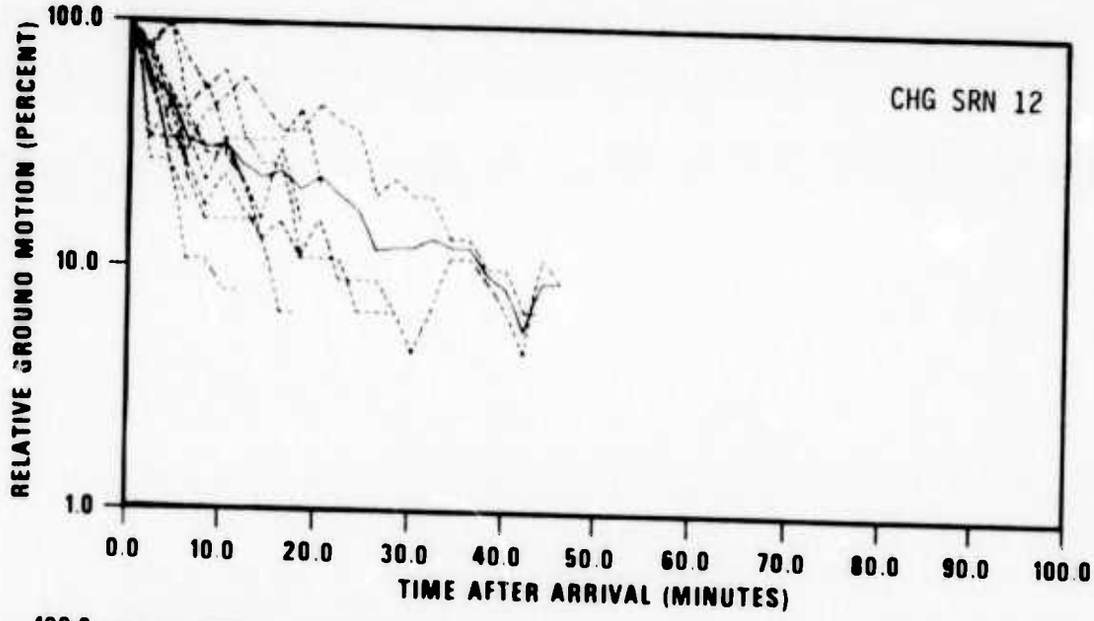
CHG SRN 12
RELATIVE GROUND MOTION (PERCENT)
100.0
10.0
1.0
0.0
10.0
20.0
30.0
40.0
50.0
60.0
70.0
80.0
90.0
100.0
TIME AFTER ARRIVAL (MINUTES)

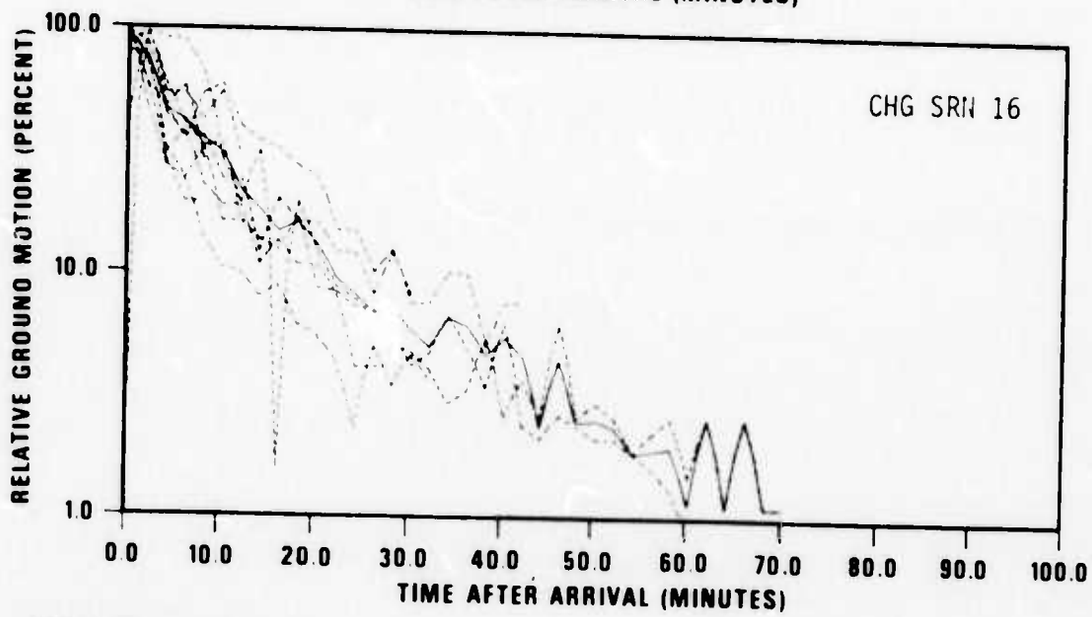
CHG SRN 16
RELATIVE GROUND MOTION (PERCENT)
100.0
10.0
1.0
0.0
10.0
20.0
30.0
40.0
50.0
60.0
70.0
80.0
90.0
100.0
TIME AFTER ARRIVAL (MINUTES)

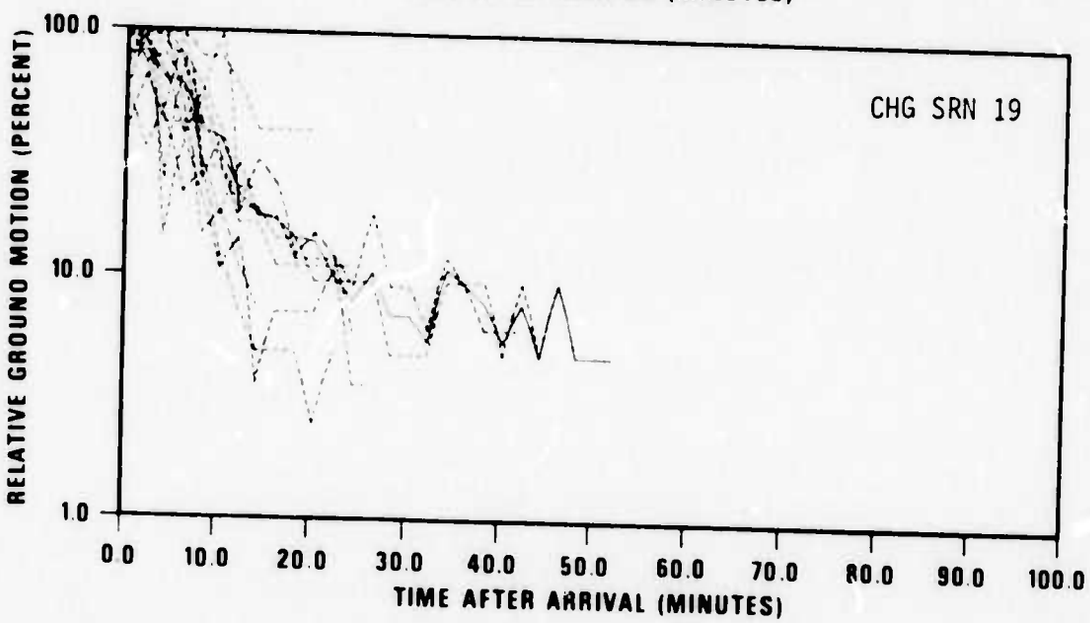
CHG SRN 19
RELATIVE GROUND MOTION (PERCENT)
100.0
10.0
1.0
0.0
10.0
20.0
30.0
40.0
50.0
60.0
70.0
80.0
90.0
100.0
TIME AFTER ARRIVAL (MINUTES)

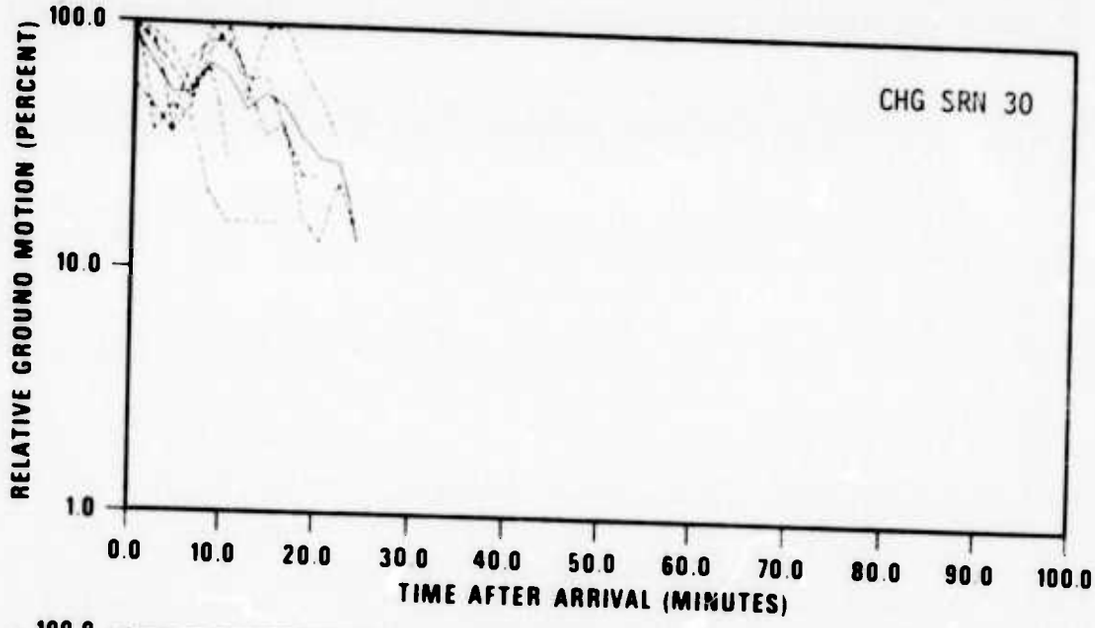
CHG SRN 30
RELATIVE GROUND MOTION (PERCENT)
100.0
10.0
1.0
0.0
10.0
20.0
30.0
40.0
50.0
60.0
70.0
80.0
90.0
100.0
TIME AFTER ARRIVAL (MINUTES)

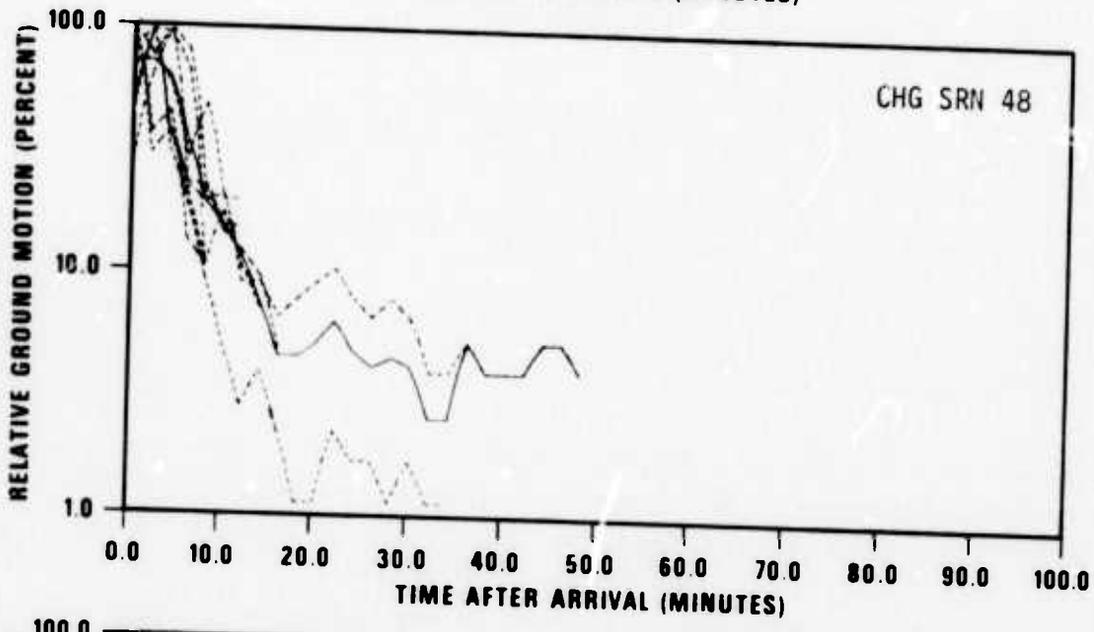
CHG SRN 48
RELATIVE GROUND MOTION (PERCENT)
100.0
10.0
1.0
0.0
10.0
20.0
30.0
40.0
50.0
60.0
70.0
80.0
90.0
100.0
TIME AFTER ARRIVAL (MINUTES)

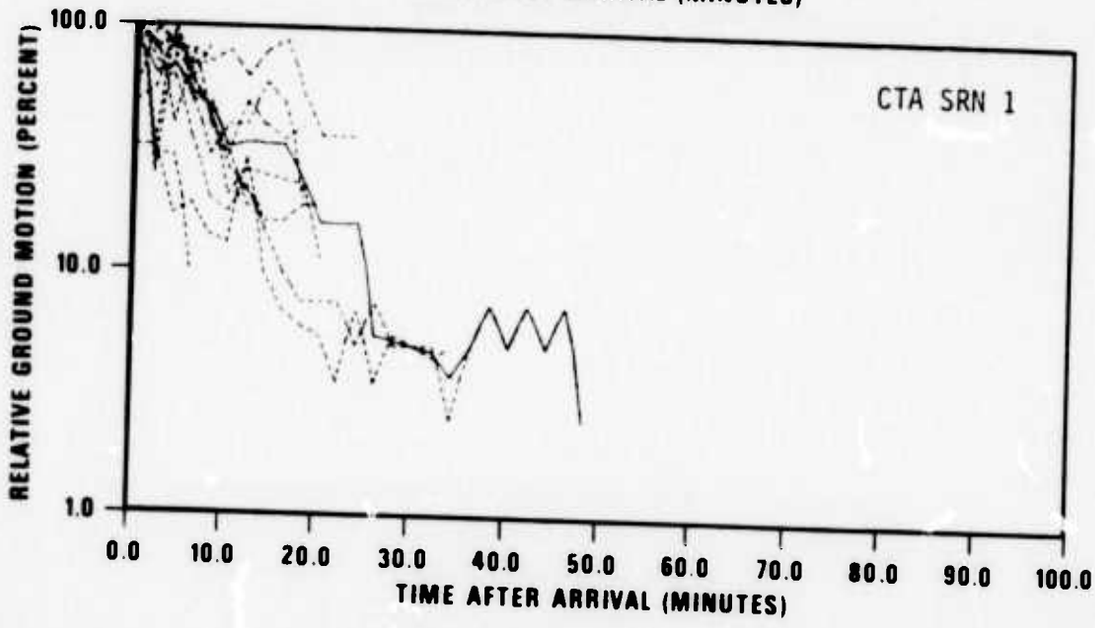
CTA SRN 1
RELATIVE GROUND MOTION (PERCENT)
100.0
10.0
1.0
0.0
10.0
20.0
30.0
40.0
50.0
60.0
70.0
80.0
90.0
100.0
TIME AFTER ARRIVAL (MINUTES)

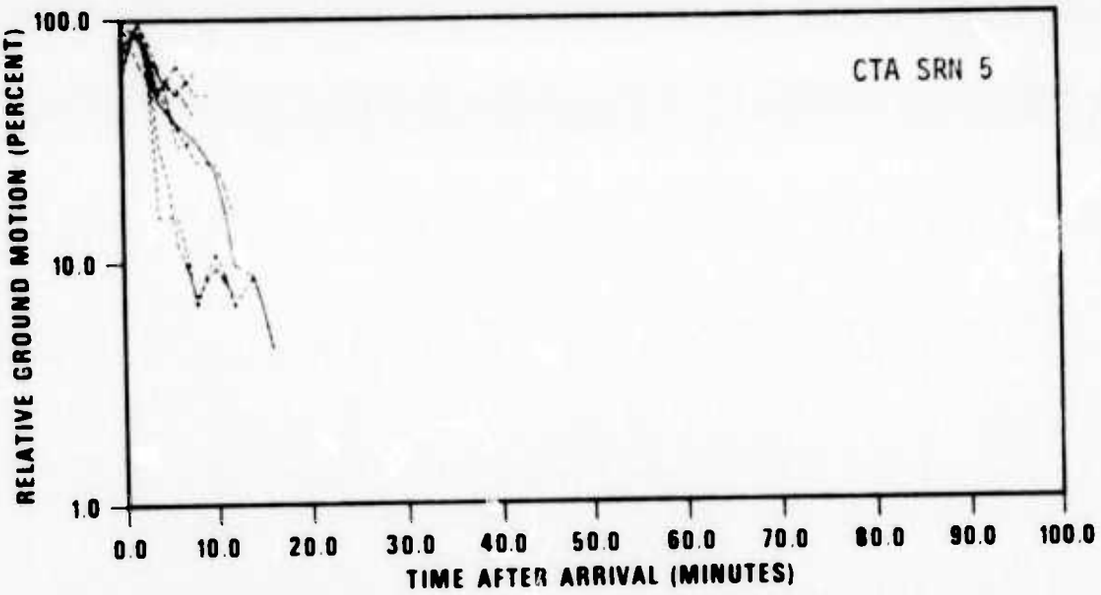
CTA SRN 5
RELATIVE GROUND MOTION (PERCENT)
100.0
10.0
1.0
0.0
10.0
20.0
30.0
40.0
50.0
60.0
70.0
80.0
90.0
100.0
TIME AFTER ARRIVAL (MINUTES)

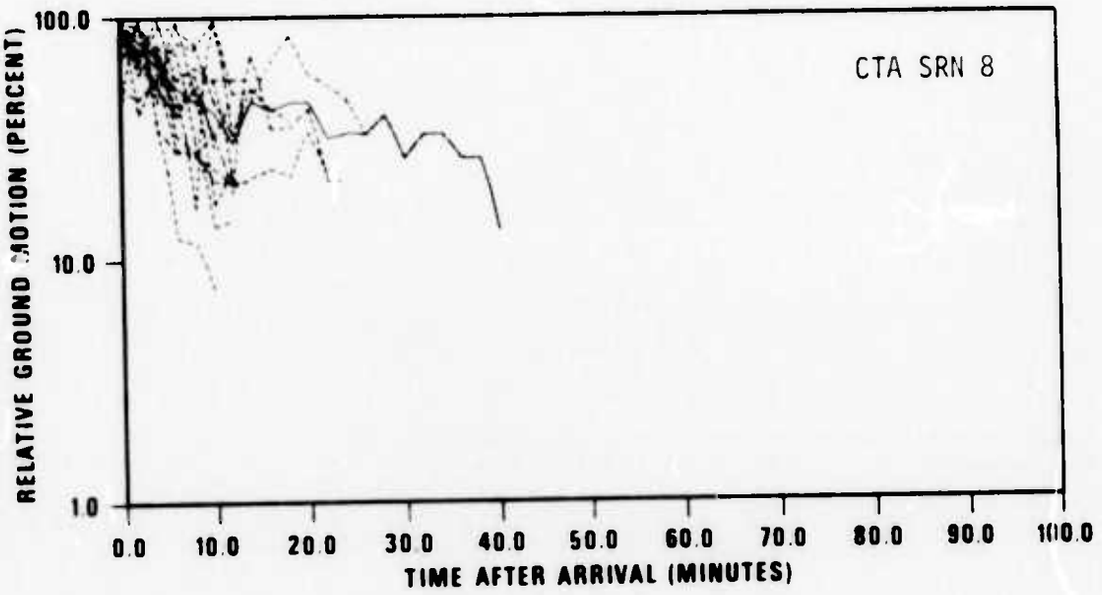
CTA SRN 8
RELATIVE GROUND MOTION (PERCENT)
100.0
10.0
1.0
0.0
10.0
20.0
30.0
40.0
50.0
60.0
70.0
80.0
90.0
100.0
TIME AFTER ARRIVAL (MINUTES)

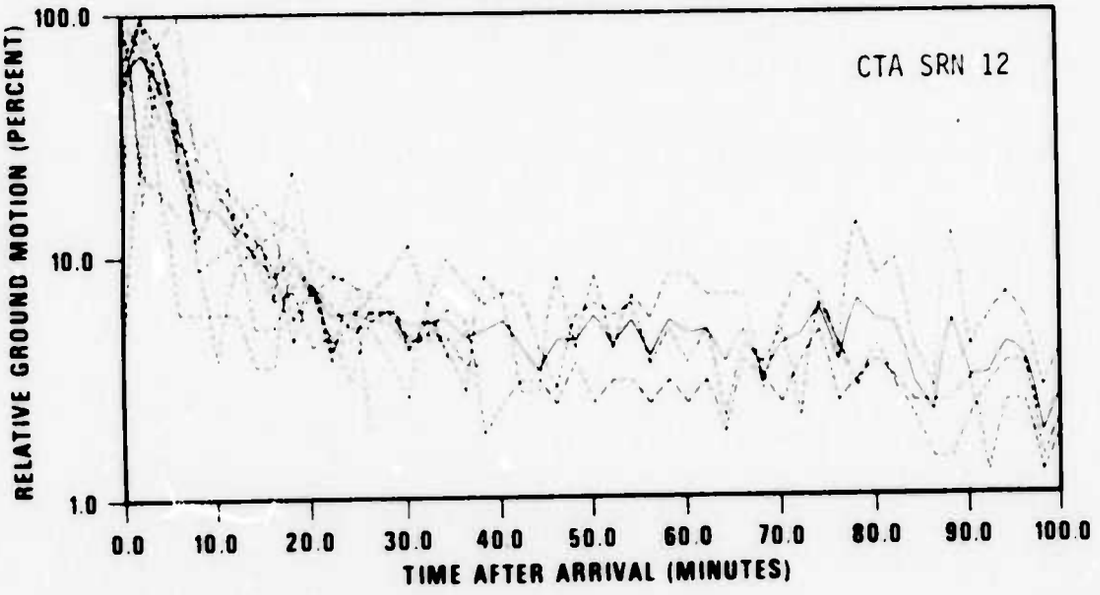
CTA SRN 12
RELATIVE GROUND MOTION (PERCENT)
100.0
10.0
1.0
0.0
10.0
20.0
30.0
40.0
50.0
60.0
70.0
80.0
90.0
100.0
TIME AFTER ARRIVAL (MINUTES)

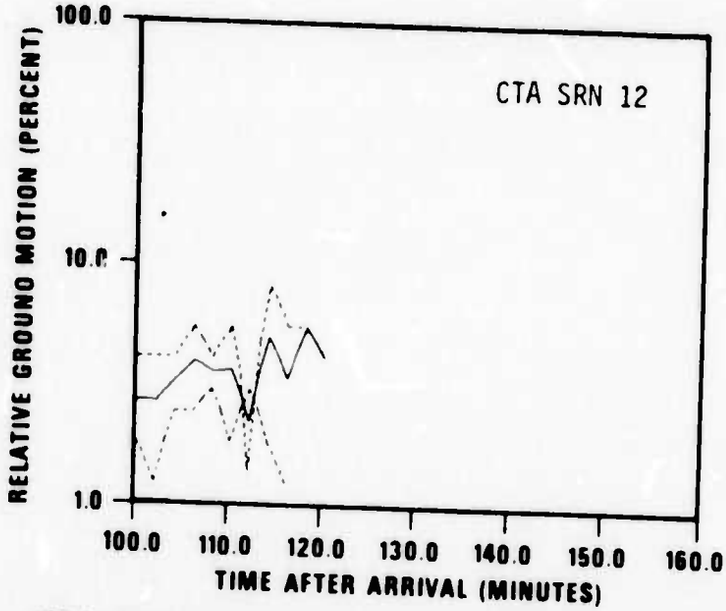
CTA SRN 12
RELATIVE GROUND MOTION (PERCENT)
100.0
10.0
1.0
100.0 110.0 120.0 130.0 140.0 150.0 160.0
TIME AFTER ARRIVAL (MINUTES)

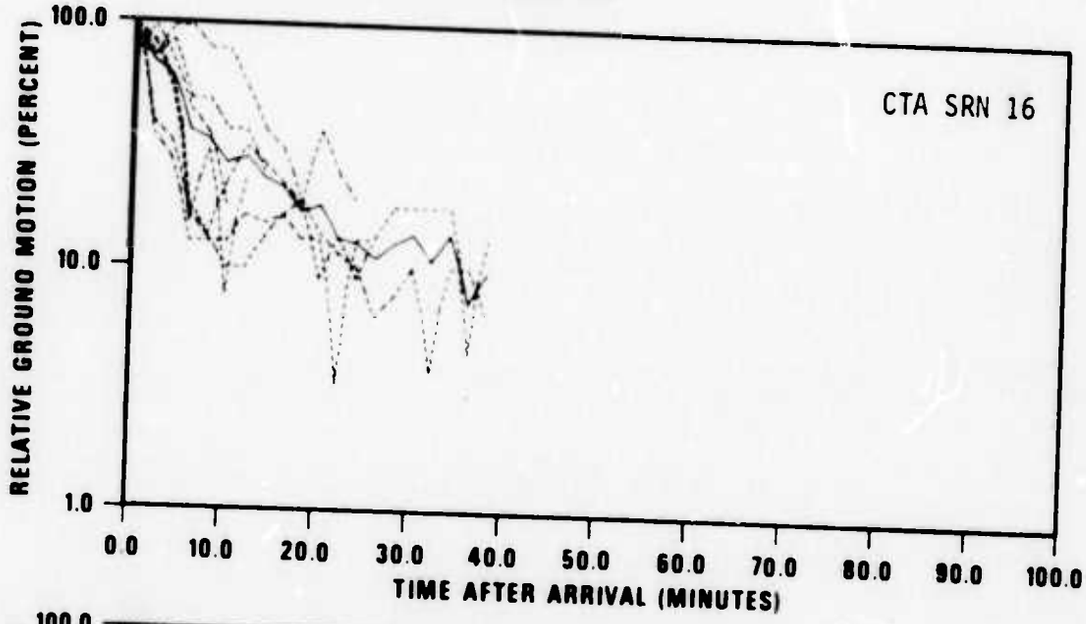
CTA SRN 16
RELATIVE GROUND MOTION (PERCENT)
100.0
10.0
1.0
0.0 10.0 20.0 30.0 40.0 50.0 60.0 70.0 80.0 90.0 100.0
TIME AFTER ARRIVAL (MINUTES)

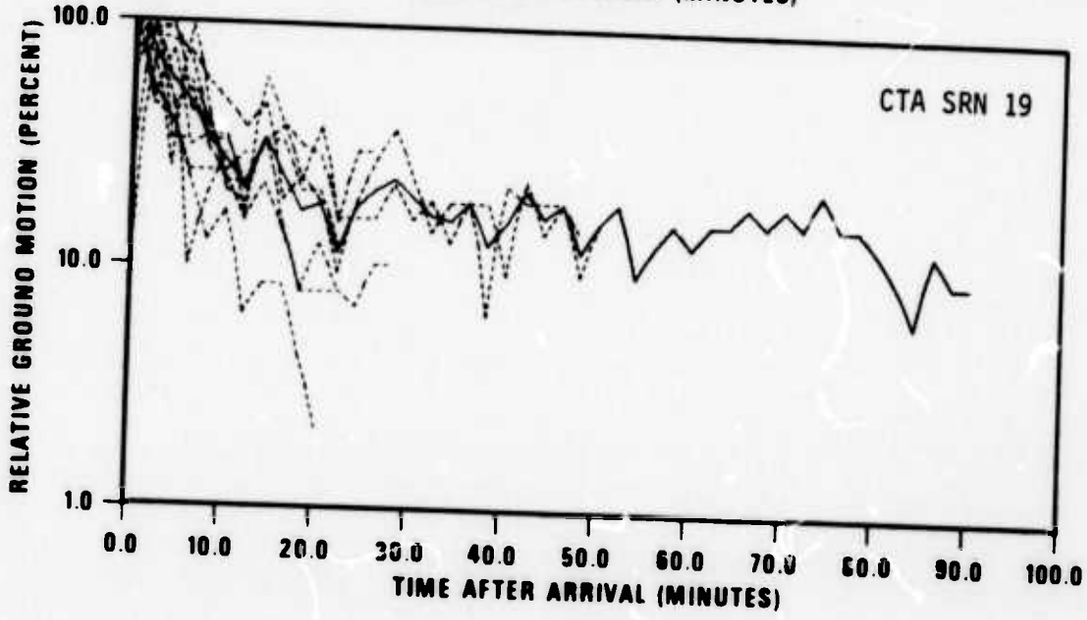
CTA SRN 19
RELATIVE GROUND MOTION (PERCENT)
100.0
10.0
1.0
0.0 10.0 20.0 30.0 40.0 50.0 60.0 70.0 80.0 90.0 100.0
TIME AFTER ARRIVAL (MINUTES)

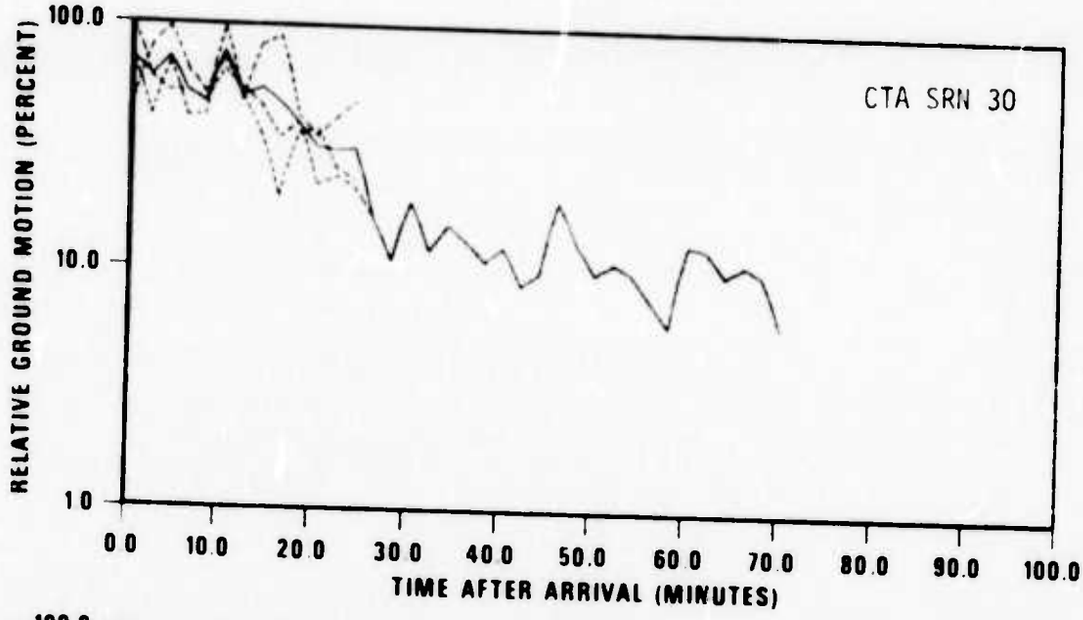
CTA SRN 30
RELATIVE GROUND MOTION (PERCENT)
100.0
10.0
1.0
0.0
10.0
20.0
30.0
40.0
50.0
60.0
70.0
80.0
90.0
100.0
TIME AFTER ARRIVAL (MINUTES)

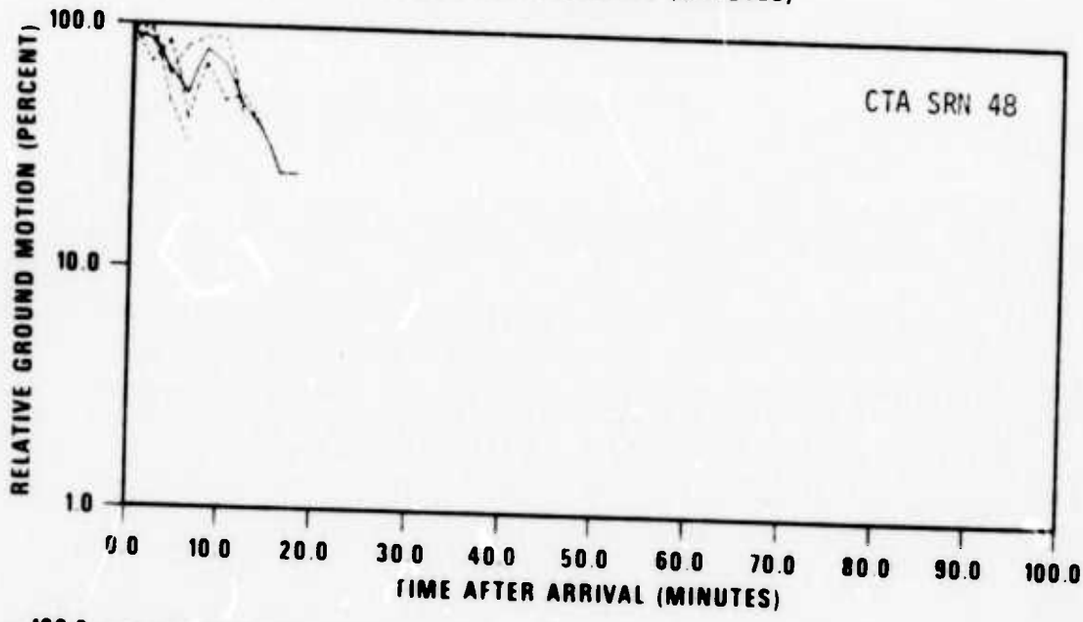
CTA SRN 48
RELATIVE GROUND MOTION (PERCENT)
100.0
10.0
1.0
0.0
10.0
20.0
30.0
40.0
50.0
60.0
70.0
80.0
90.0
100.0
TIME AFTER ARRIVAL (MINUTES)

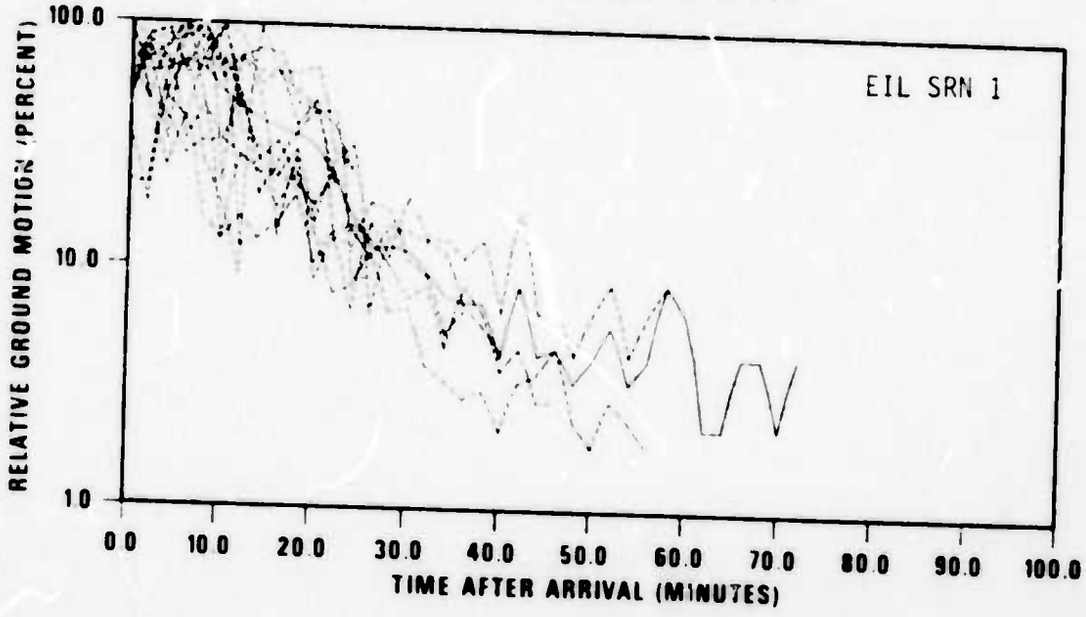
EIL SRN 1
RELATIVE GROUND MOTION (PERCENT)
100.0
10.0
1.0
0.0
10.0
20.0
30.0
40.0
50.0
60.0
70.0
80.0
90.0
100.0
TIME AFTER ARRIVAL (MINUTES)

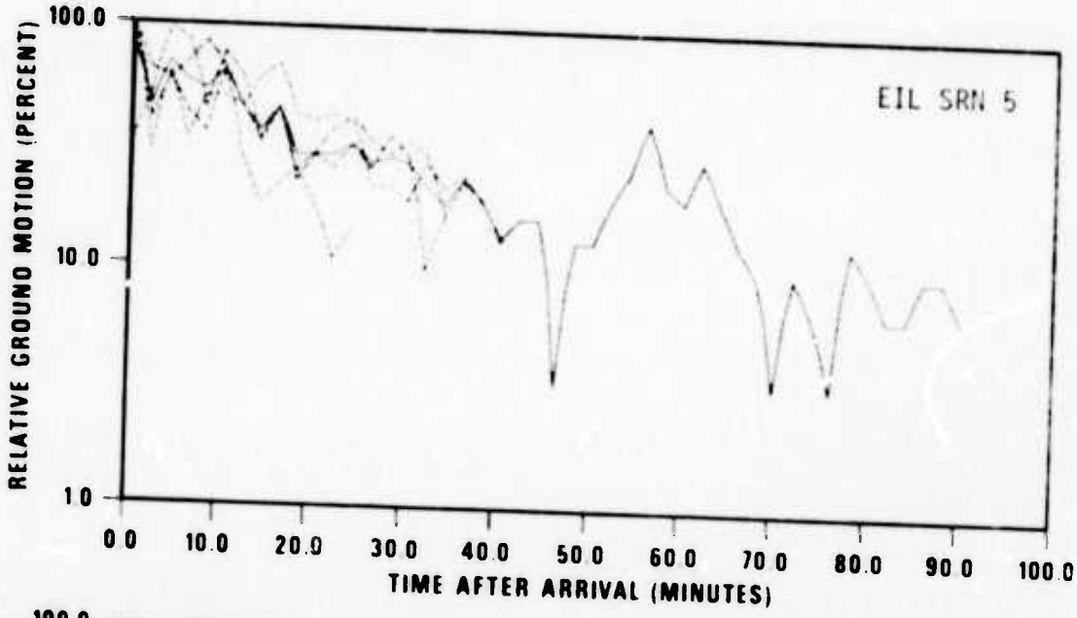
EIL SRN 5
RELATIVE GROUND MOTION (PERCENT)
100.0
10.0
1.0
0.0
10.0
20.0
30.0
40.0
50.0
60.0
70.0
80.0
90.0
100.0
TIME AFTER ARRIVAL (MINUTES)

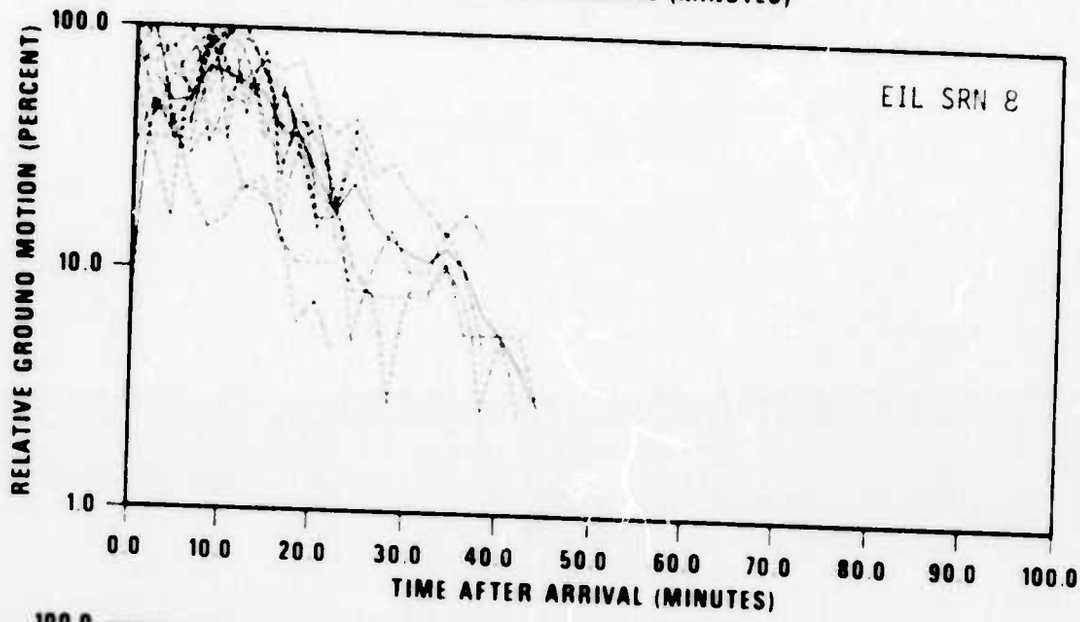
EIL SRN 8
RELATIVE GROUND MOTION (PERCENT)
100.0
10.0
1.0
0.0
10.0
20.0
30.0
40.0
50.0
60.0
70.0
80.0
90.0
100.0
TIME AFTER ARRIVAL (MINUTES)

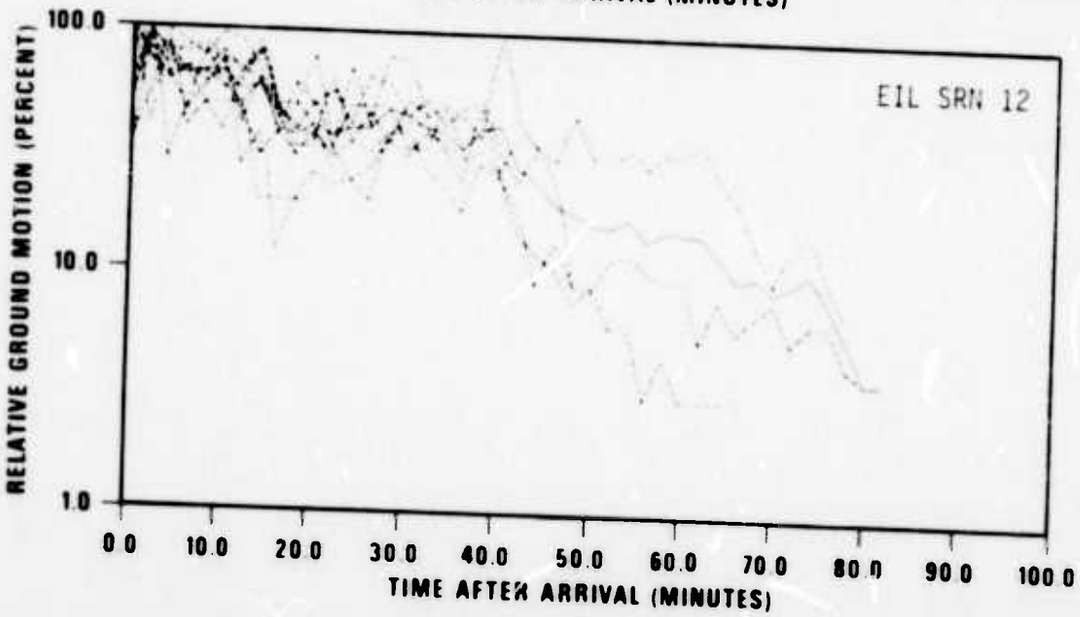
EIL SRN 12
RELATIVE GROUND MOTION (PERCENT)
100.0
10.0
1.0
0.0
10.0
20.0
30.0
40.0
50.0
60.0
70.0
80.0
90.0
100.0
TIME AFTER ARRIVAL (MINUTES)

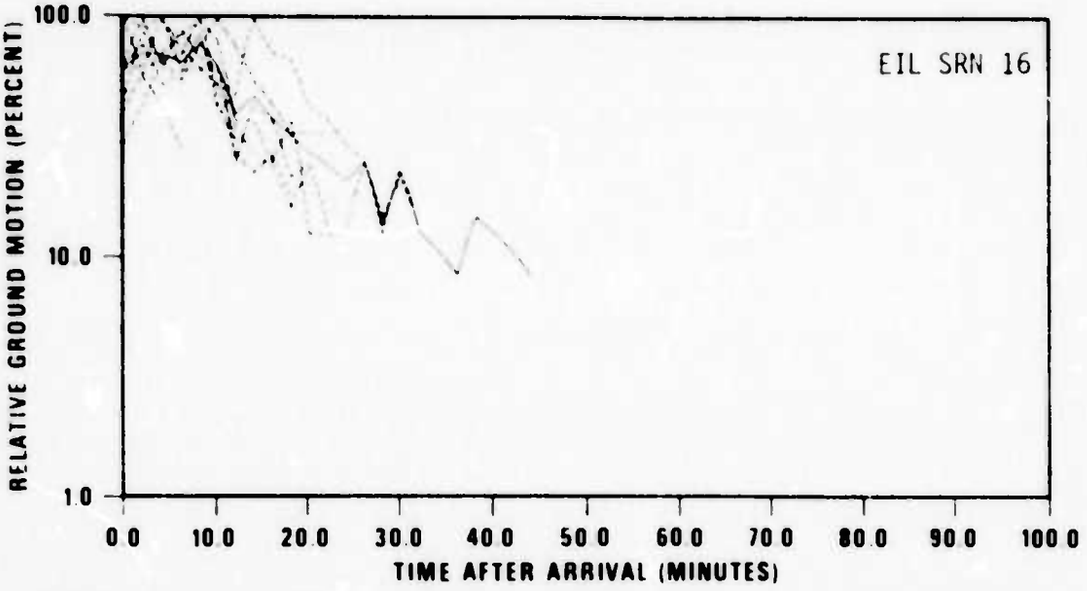
EIL SRN 16
RELATIVE GROUND MOTION (PERCENT)
100.0
10.0
1.0
0.0
10.0
20.0
30.0
40.0
50.0
60.0
70.0
80.0
90.0
100.0
TIME AFTER ARRIVAL (MINUTES)

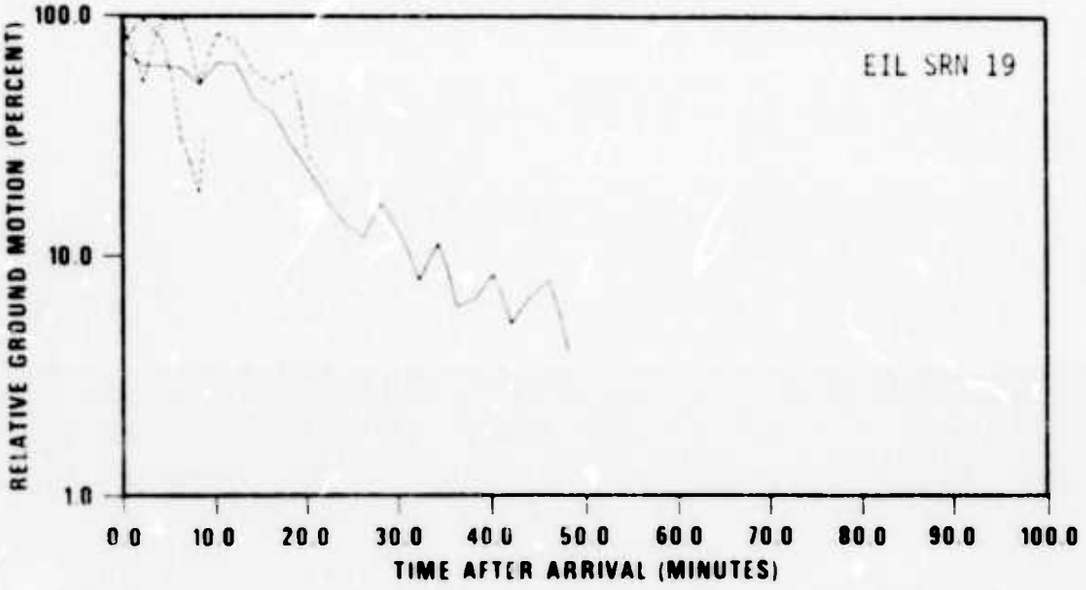
EIL SRN 19
RELATIVE GROUND MOTION (PERCENT)
100.0
10.0
1.0
0.0
10.0
20.0
30.0
40.0
50.0
60.0
70.0
80.0
90.0
100.0
TIME AFTER ARRIVAL (MINUTES)

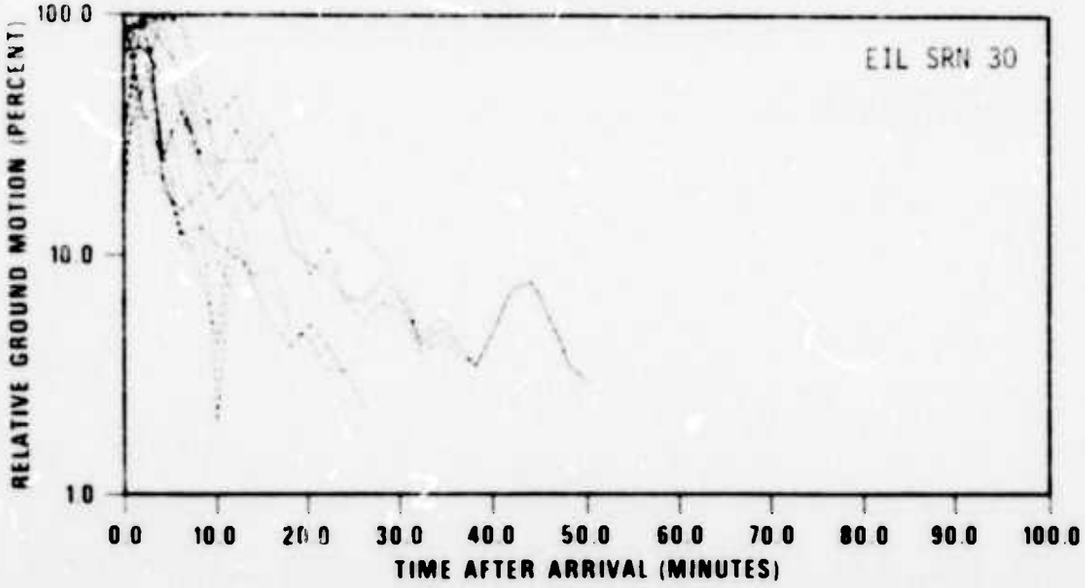
EIL SRN 30
RELATIVE GROUND MOTION (PERCENT)
100.0
10.0
1.0
0.0
10.0
20.0
30.0
40.0
50.0
60.0
70.0
80.0
90.0
100.0
TIME AFTER ARRIVAL (MINUTES)

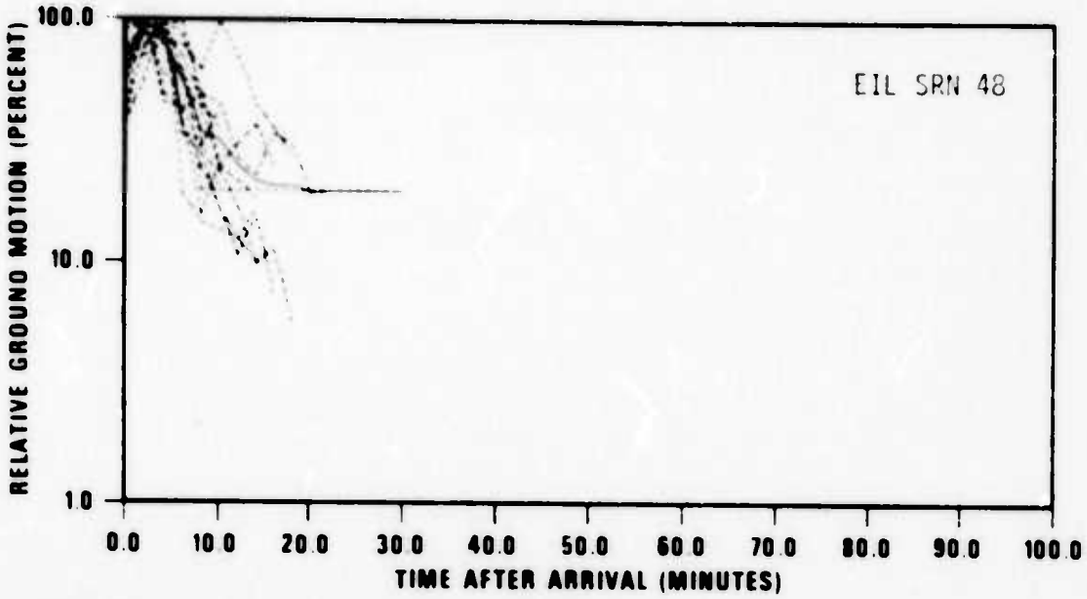
EIL SRN 48
RELATIVE GROUND MOTION (PERCENT)
100.0
10.0
1.0
0.0
10.0
20.0
30.0
40.0
50.0
60.0
70.0
80.0
90.0
100.0
TIME AFTER ARRIVAL (MINUTES)

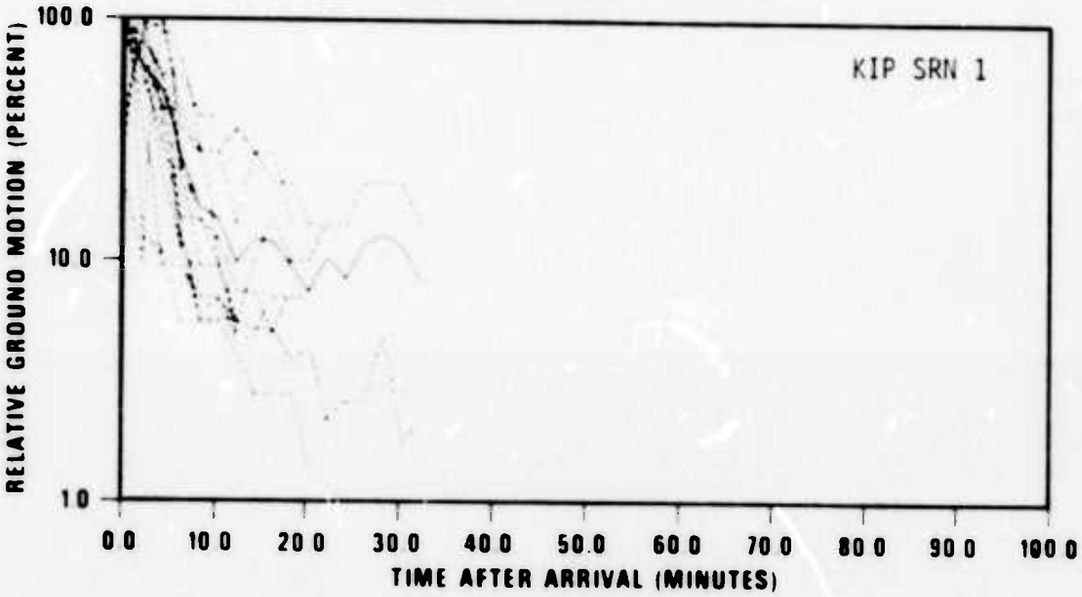
KIP SRN 1
RELATIVE GROUND MOTION (PERCENT)
100.0
10.0
1.0
0.0
10.0
20.0
30.0
40.0
50.0
60.0
70.0
80.0
90.0
100.0
TIME AFTER ARRIVAL (MINUTES)

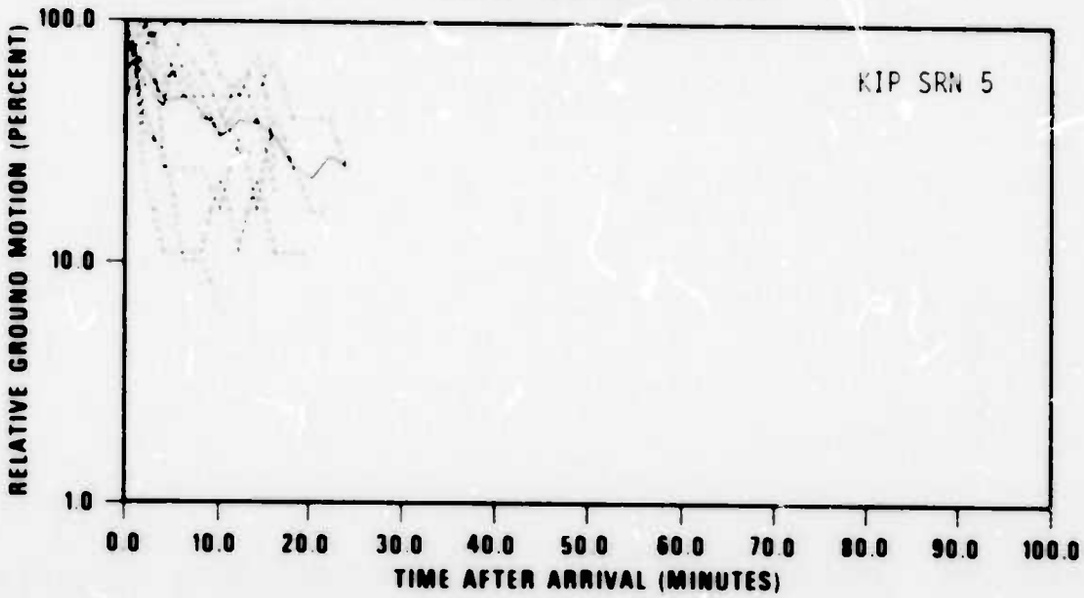
KIP SRN 5
RELATIVE GROUND MOTION (PERCENT)
100.0
10.0
1.0
0.0
10.0
20.0
30.0
40.0
50.0
60.0
70.0
80.0
90.0
100.0
TIME AFTER ARRIVAL (MINUTES)

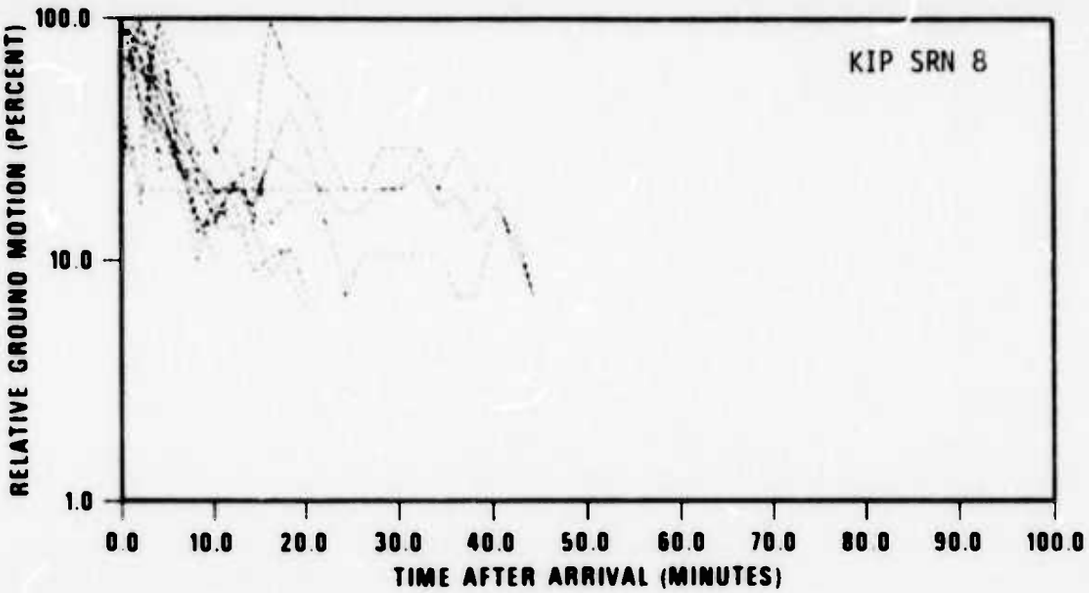
KIP SRN 8
RELATIVE GROUND MOTION (PERCENT)
100.0
10.0
1.0
0.0
10.0
20.0
30.0
40.0
50.0
60.0
70.0
80.0
90.0
100.0
TIME AFTER ARRIVAL (MINUTES)

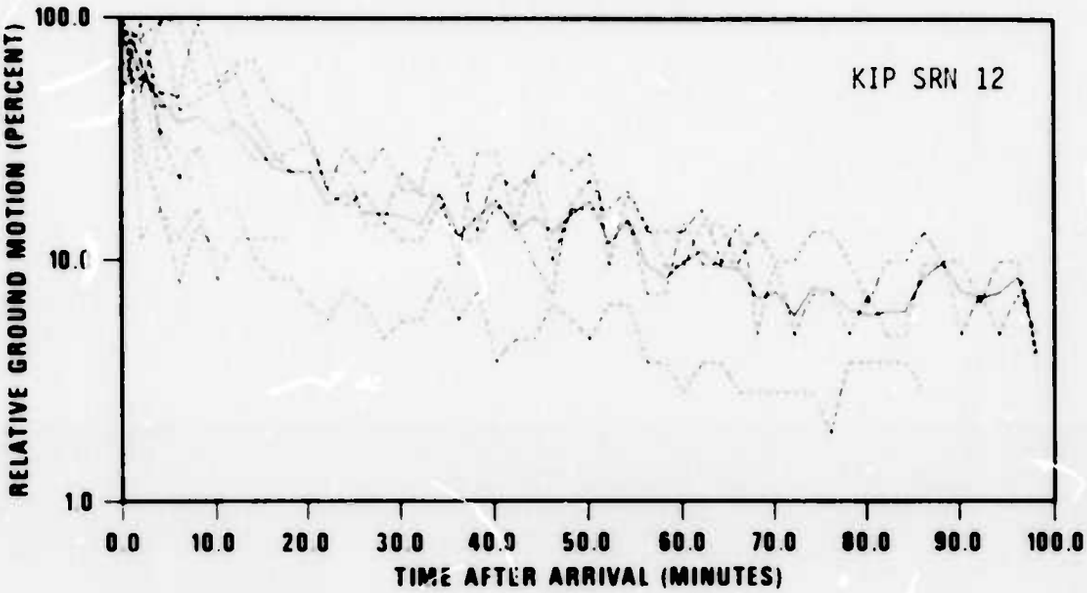
KIP SRN 12
RELATIVE GROUND MOTION (PERCENT)
100.0
10.0
1.0
0.0
10.0
20.0
30.0
40.0
50.0
60.0
70.0
80.0
90.0
100.0
TIME AFTER ARRIVAL (MINUTES)

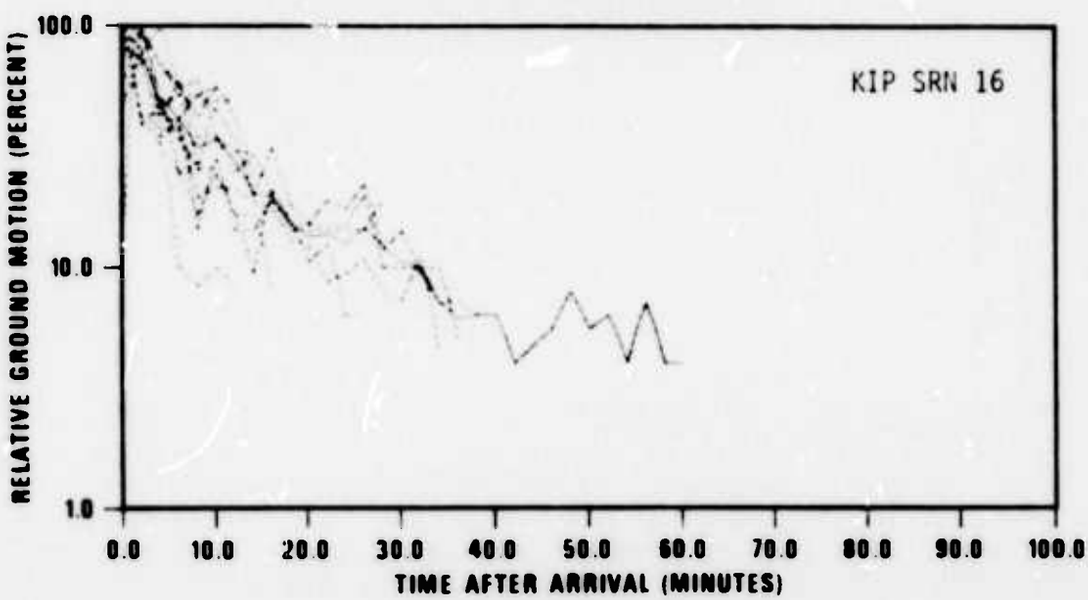
KIP SRN 16
RELATIVE GROUND MOTION (PERCENT)
100.0
10.0
1.0
0.0
10.0
20.0
30.0
40.0
50.0
60.0
70.0
80.0
90.0
100.0
TIME AFTER ARRIVAL (MINUTES)

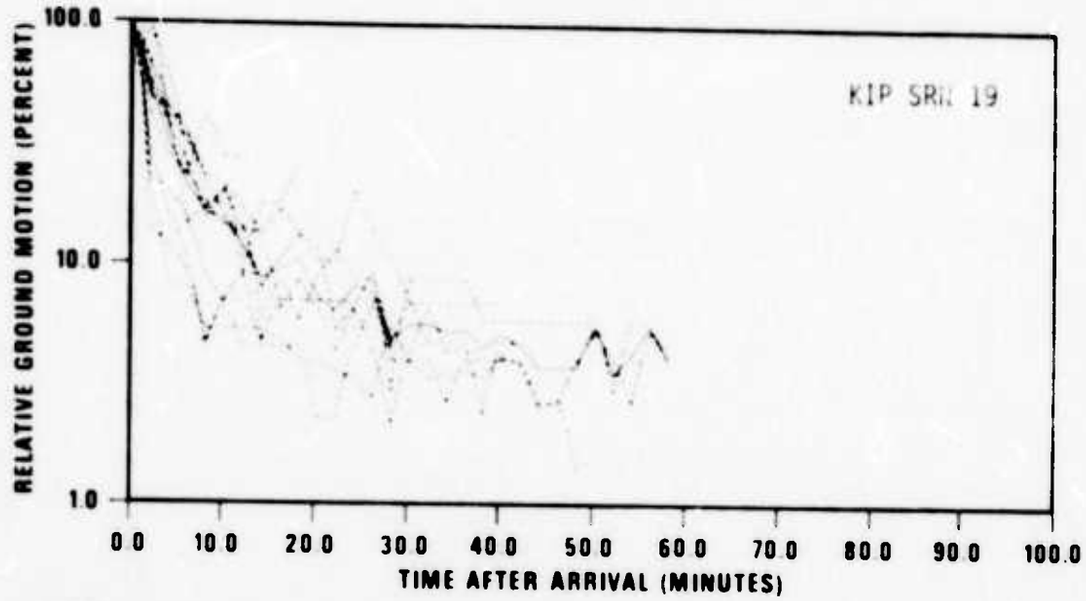
KIP SRN 19
RELATIVE GROUND MOTION (PERCENT)
100.0
10.0
1.0
0.0
10.0
20.0
30.0
40.0
50.0
60.0
70.0
80.0
90.0
100.0
TIME AFTER ARRIVAL (MINUTES)

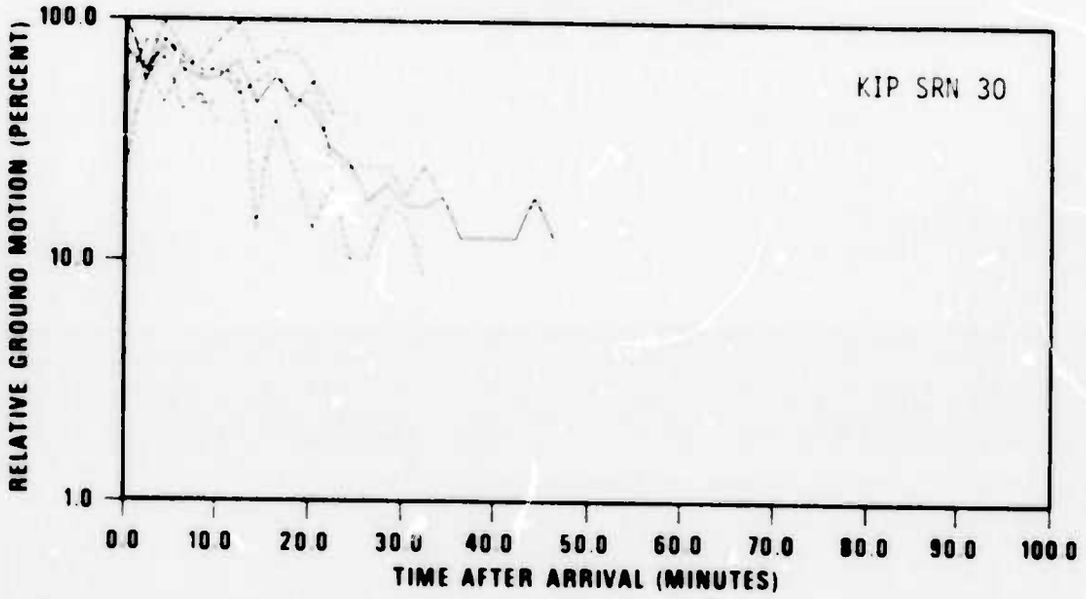
KIP SRN 30
RELATIVE GROUND MOTION (PERCENT)
100.0
10.0
1.0
0.0
10.0
20.0
30.0
40.0
50.0
60.0
70.0
80.0
90.0
100.0
TIME AFTER ARRIVAL (MINUTES)

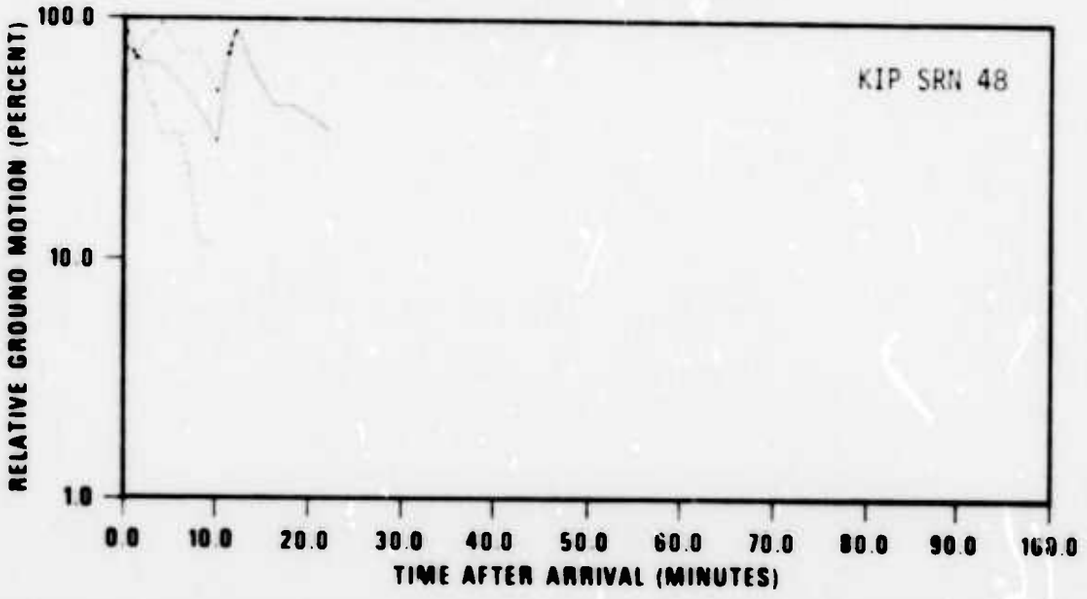
KIP SRN 48
RELATIVE GROUND MOTION (PERCENT)
100.0
10.0
1.0
0.0
10.0
20.0
30.0
40.0
50.0
60.0
70.0
80.0
90.0
100.0
TIME AFTER ARRIVAL (MINUTES)

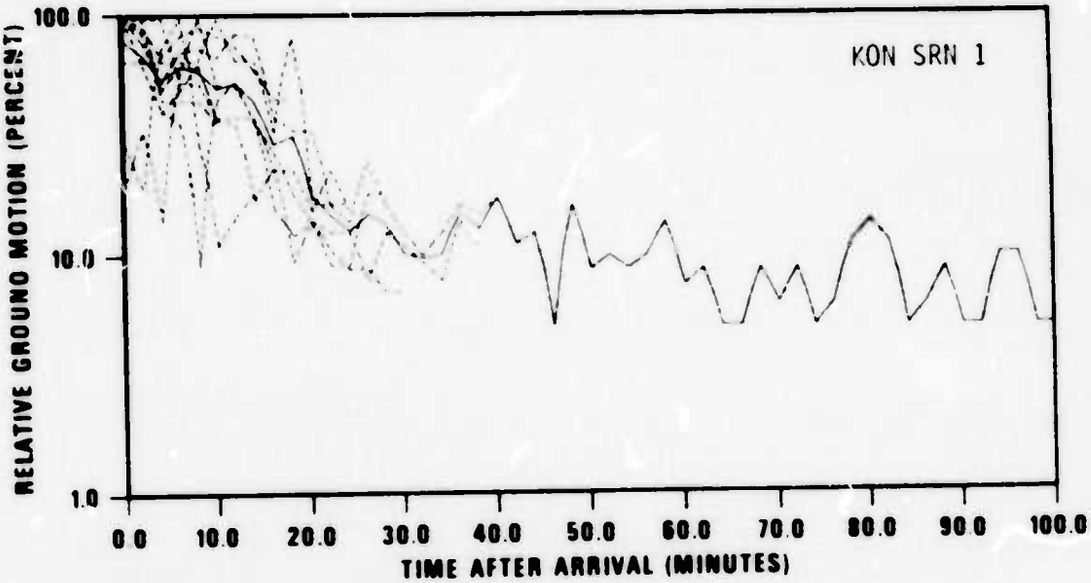
KON SRN 1
RELATIVE GROUND MOTION (PERCENT)
100.0
10.0
1.0
0.0
10.0
20.0
30.0
40.0
50.0
60.0
70.0
80.0
90.0
100.0
TIME AFTER ARRIVAL (MINUTES)

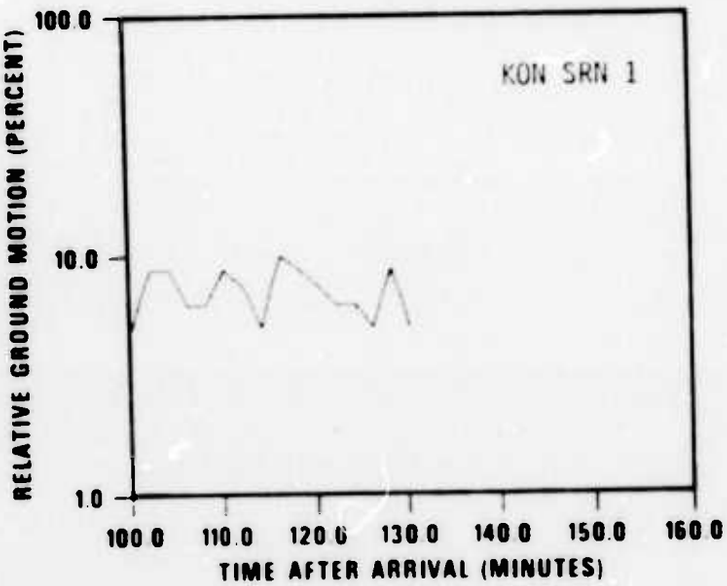
KON SRN 1
RELATIVE GROUND MOTION (PERCENT)
100.0
10.0
1.0
100.0
110.0
120.0
130.0
140.0
150.0
160.0
TIME AFTER ARRIVAL (MINUTES)

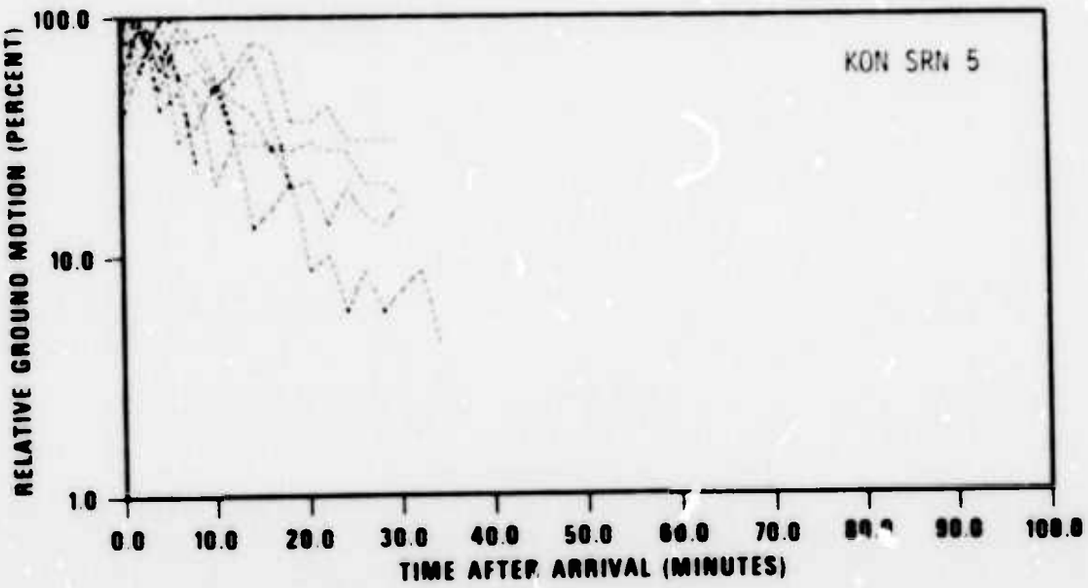
KON SRN 5
RELATIVE GROUND MOTION (PERCENT)
100.0
10.0
1.0
0.0
10.0
20.0
30.0
40.0
50.0
60.0
70.0
80.0
90.0
100.0
TIME AFTER ARRIVAL (MINUTES)

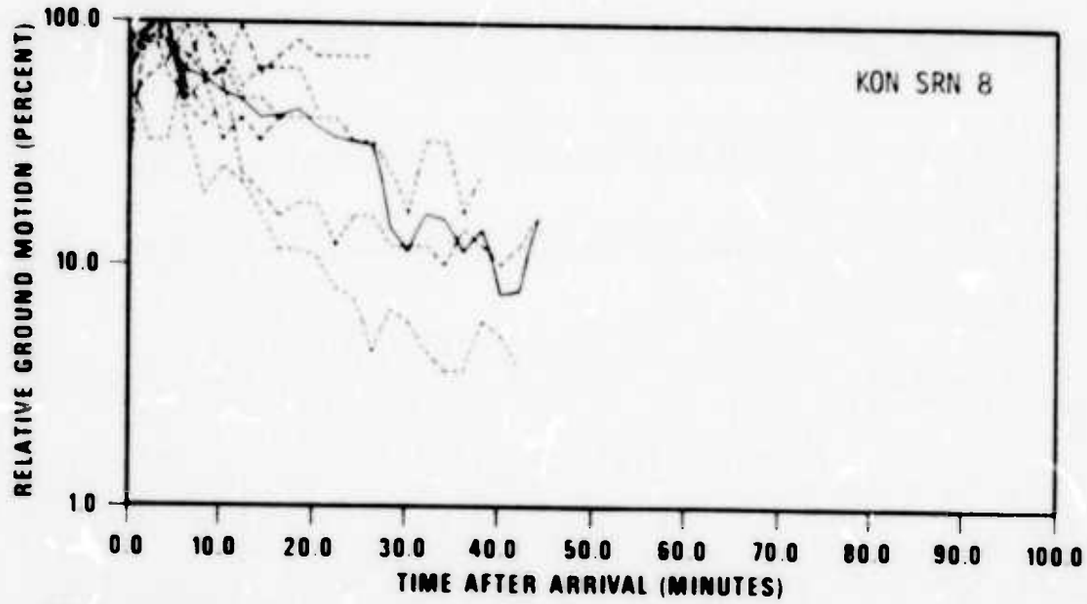
KON SRN 8
RELATIVE GROUND MOTION (PERCENT)
100.0
10.0
1.0
0.0
10.0
20.0
30.0
40.0
50.0
60.0
70.0
80.0
90.0
100.0
TIME AFTER ARRIVAL (MINUTES)

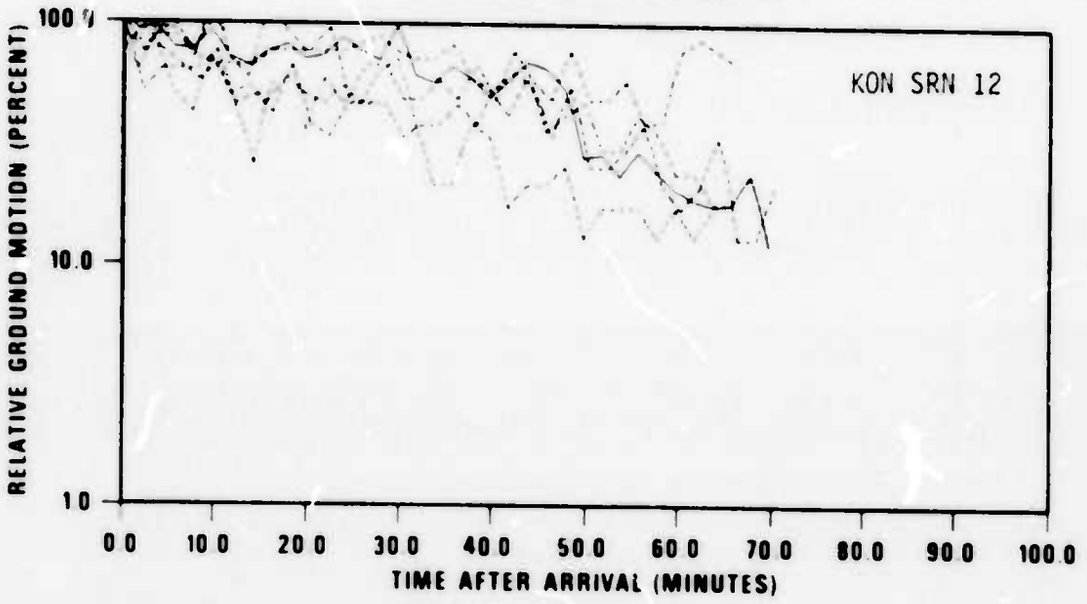
KON SRN 12
RELATIVE GROUND MOTION (PERCENT)
100.0
10.0
1.0
0.0
10.0
20.0
30.0
40.0
50.0
60.0
70.0
80.0
90.0
100.0
TIME AFTER ARRIVAL (MINUTES)

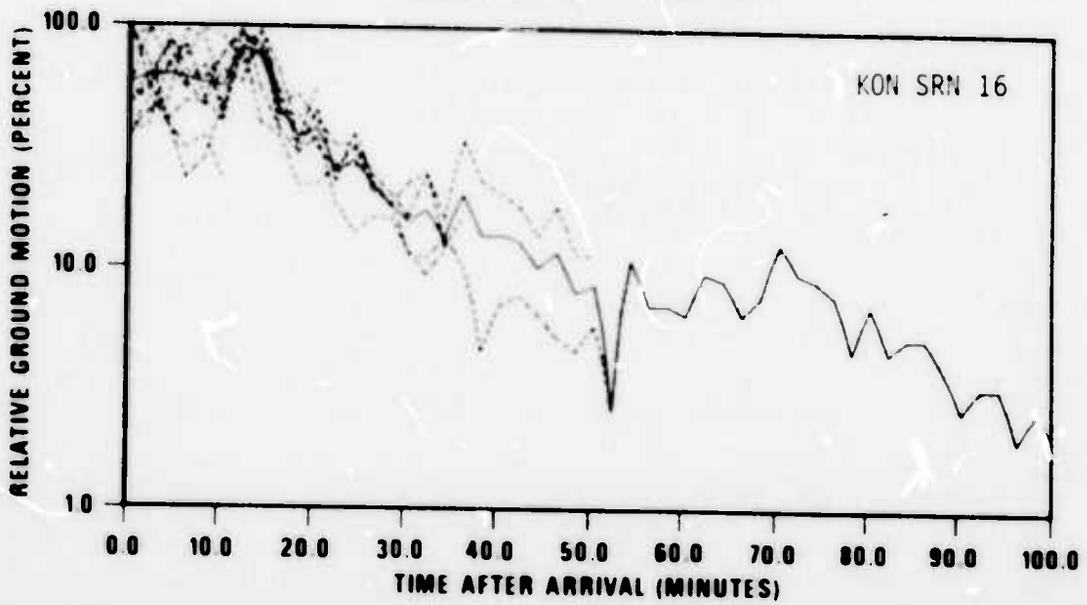
KON SRN 16
RELATIVE GROUND MOTION (PERCENT)
100.0
10.0
1.0
0.0
10.0
20.0
30.0
40.0
50.0
60.0
70.0
80.0
90.0
100.0
TIME AFTER ARRIVAL (MINUTES)

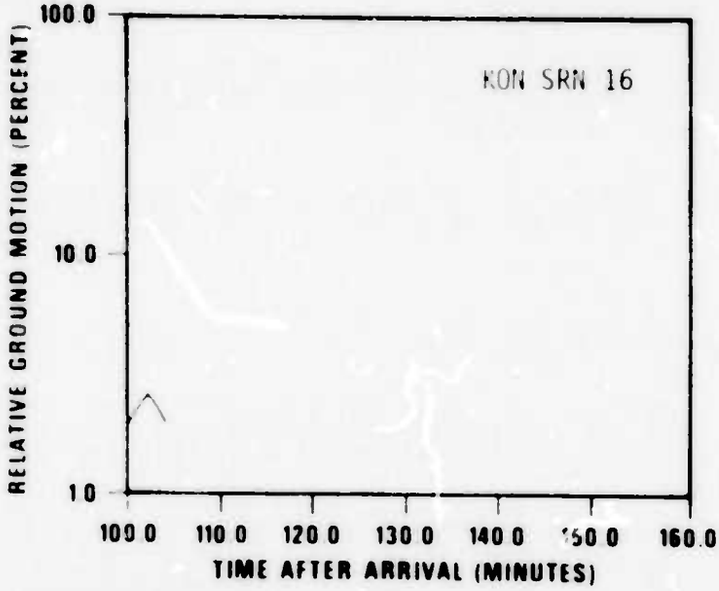
KON SRN 16
RELATIVE GROUND MOTION (PERCENT)
100.0
10.0
1.0
100.0
110.0
120.0
130.0
140.0
150.0
160.0
TIME AFTER ARRIVAL (MINUTES)

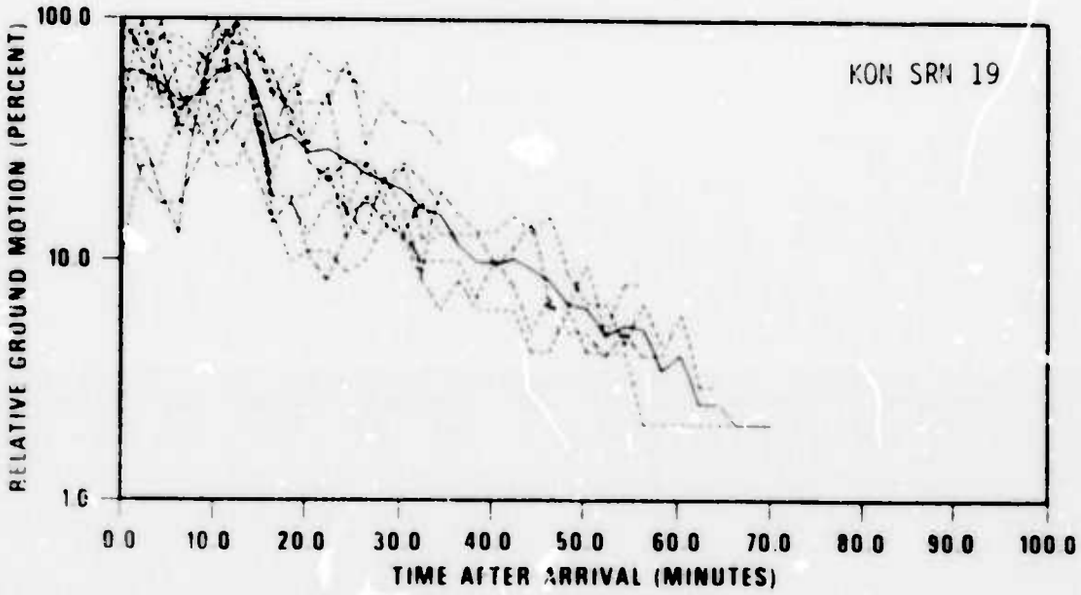
KON SRN 19
RELATIVE GROUND MOTION (PERCENT)
100.0
10.0
1.0
0.0
10.0
20.0
30.0
40.0
50.0
60.0
70.0
80.0
90.0
100.0
TIME AFTER ARRIVAL (MINUTES)

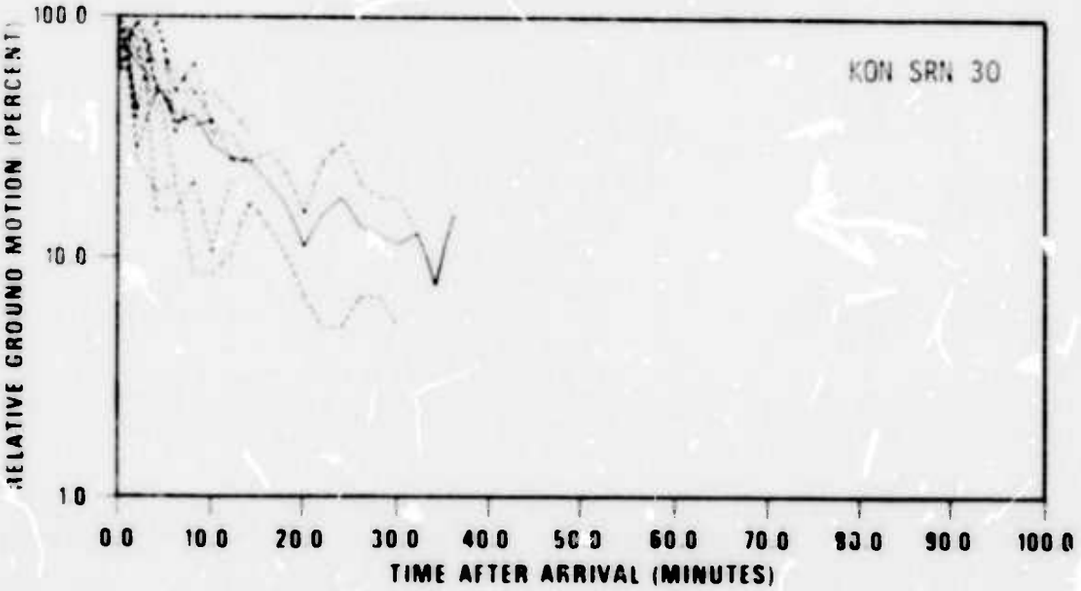
KON SRN 30
RELATIVE GROUND MOTION (PERCENT)
100.0
10.0
1.0
0.0
10.0
20.0
30.0
40.0
50.0
60.0
70.0
80.0
90.0
100.0
TIME AFTER ARRIVAL (MINUTES)

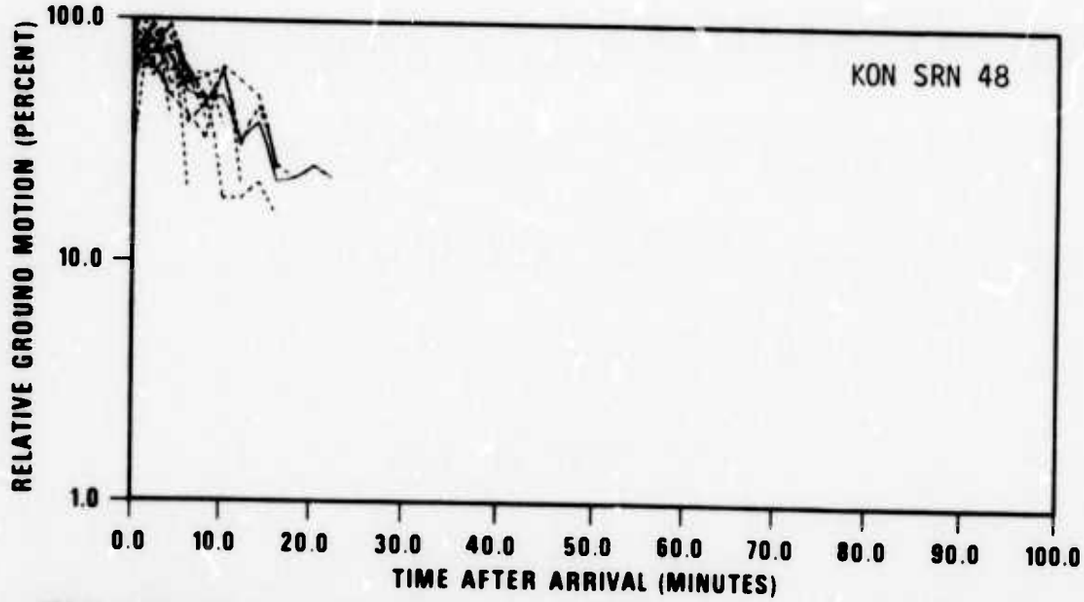
KON SRN 48
RELATIVE GROUND MOTION (PERCENT)
100.0
10.0
1.0
0.0
10.0
20.0
30.0
40.0
50.0
60.0
70.0
80.0
90.0
100.0
TIME AFTER ARRIVAL (MINUTES)

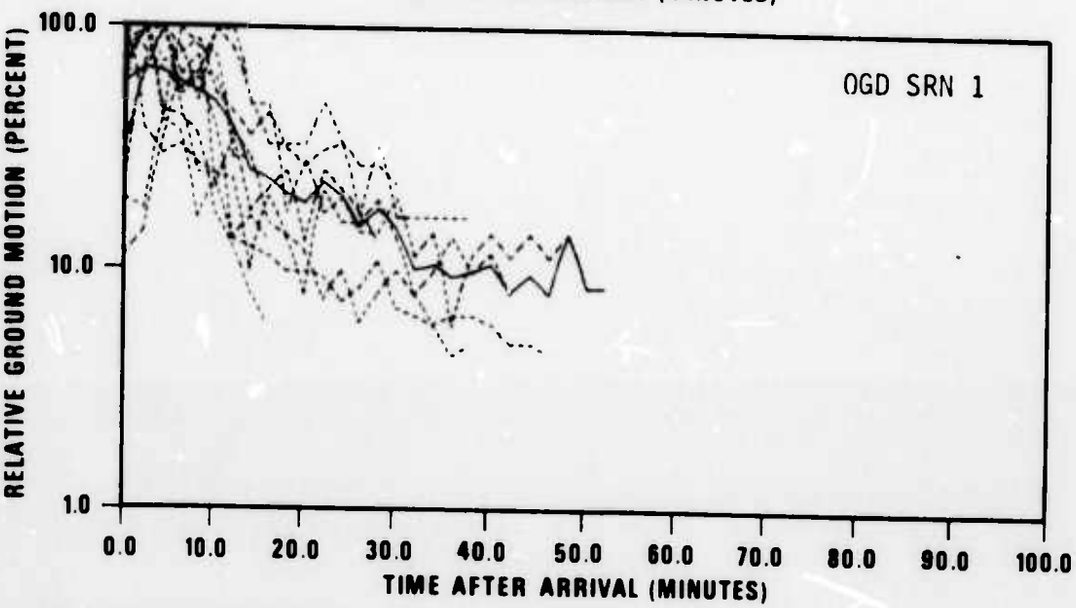
OGD SRN 1
RELATIVE GROUND MOTION (PERCENT)
100.0
10.0
1.0
0.0
10.0
20.0
30.0
40.0
50.0
60.0
70.0
80.0
90.0
100.0
TIME AFTER ARRIVAL (MINUTES)

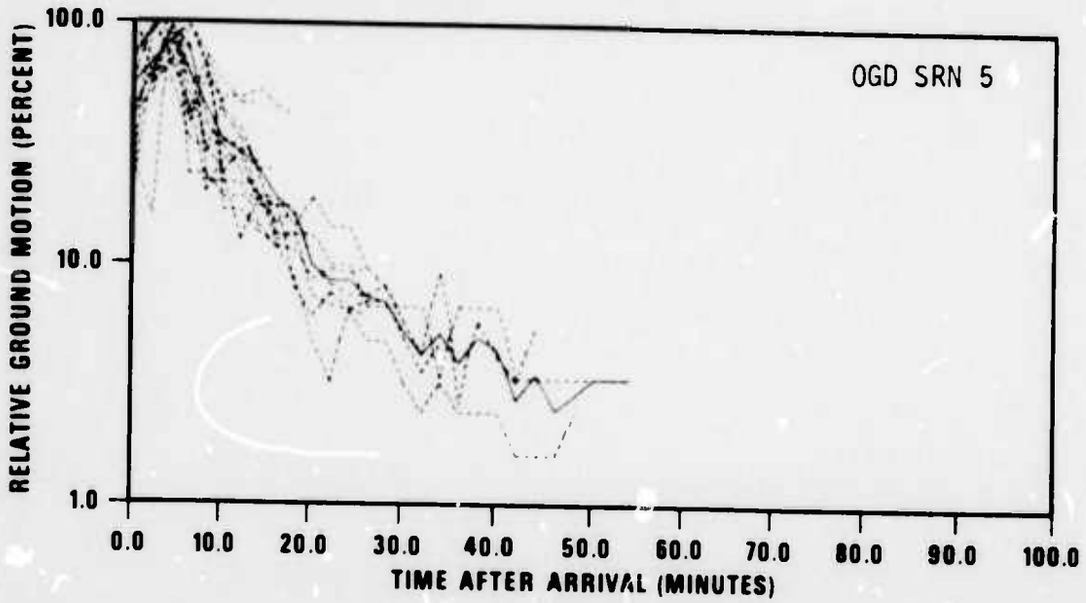
OGD SRN 5
RELATIVE GROUND MOTION (PERCENT)
100.0
10.0
1.0
0.0
10.0
20.0
30.0
40.0
50.0
60.0
70.0
80.0
90.0
100.0
TIME AFTER ARRIVAL (MINUTES)

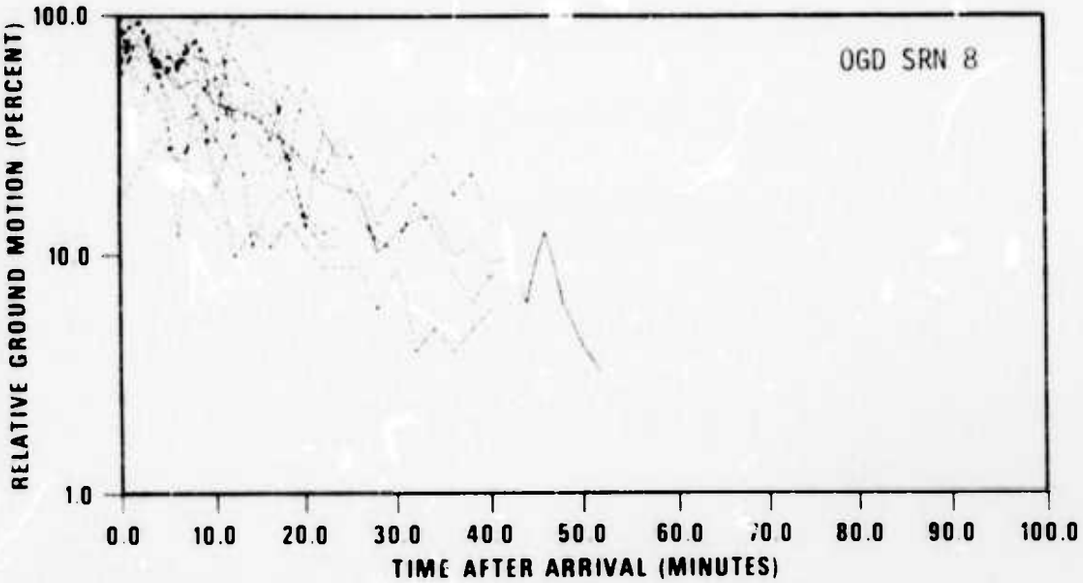
OGD SRN 8
RELATIVE GROUND MOTION (PERCENT)
100.0
10.0
1.0
0.0
10.0
20.0
30.0
40.0
50.0
60.0
70.0
80.0
90.0
100.0
TIME AFTER ARRIVAL (MINUTES)

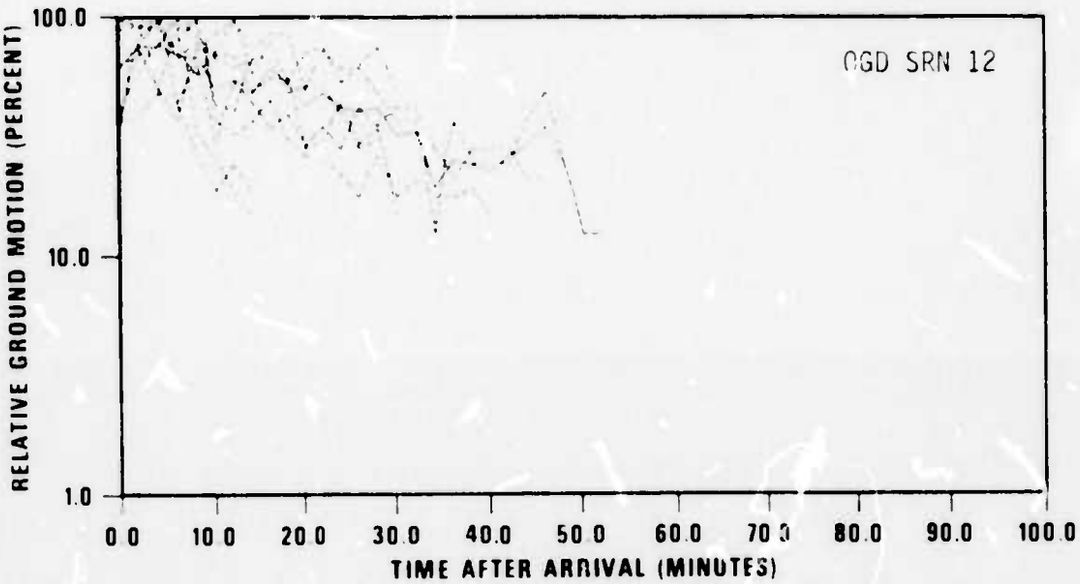
OGD SRN 12
RELATIVE GROUND MOTION (PERCENT)
100.0
10.0
1.0
0.0
10.0
20.0
30.0
40.0
50.0
60.0
70.0
80.0
90.0
100.0
TIME AFTER ARRIVAL (MINUTES)

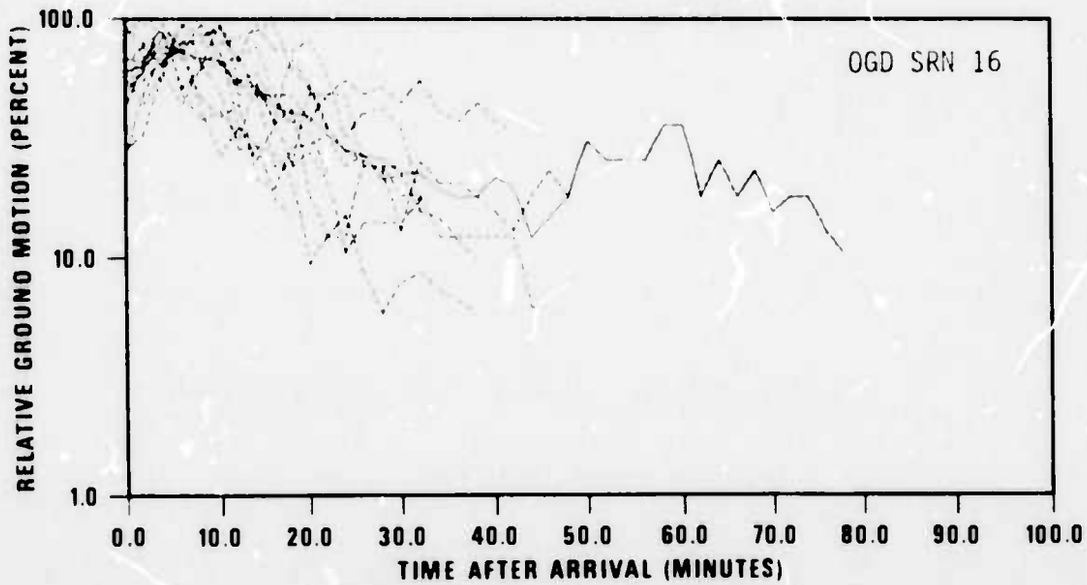
OGD SRN 16
RELATIVE GROUND MOTION (PERCENT)
100.0
10.0
1.0
0.0
10.0
20.0
30.0
40.0
50.0
60.0
70.0
80.0
90.0
100.0
TIME AFTER ARRIVAL (MINUTES)

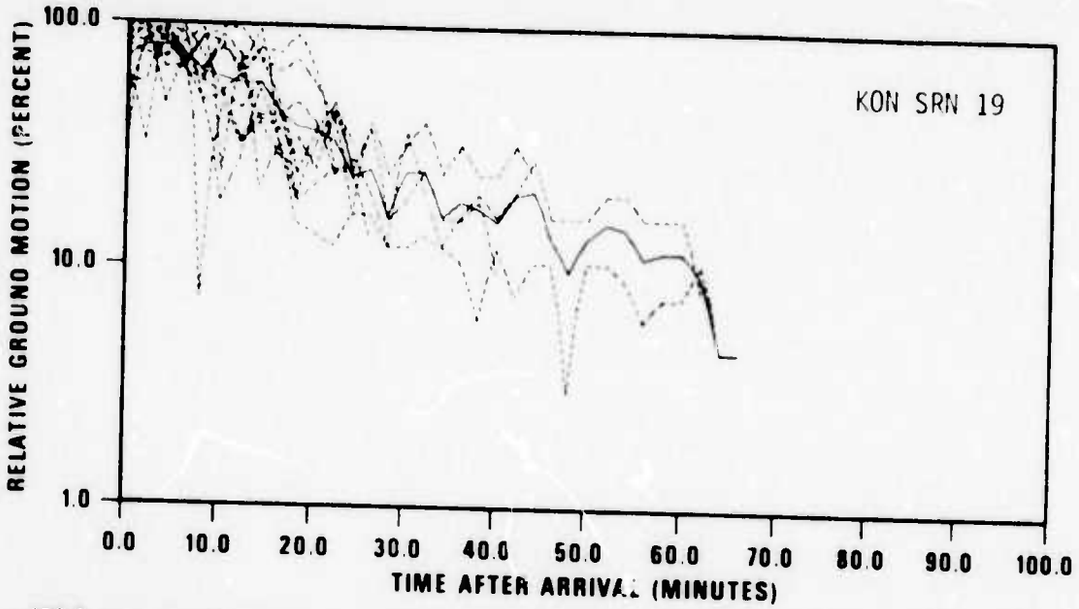
KON SRN 19
RELATIVE GROUND MOTION (PERCENT)
100.0
10.0
1.0
0.0
10.0
20.0
30.0
40.0
50.0
60.0
70.0
80.0
90.0
100.0
TIME AFTER ARRIVAL (MINUTES)

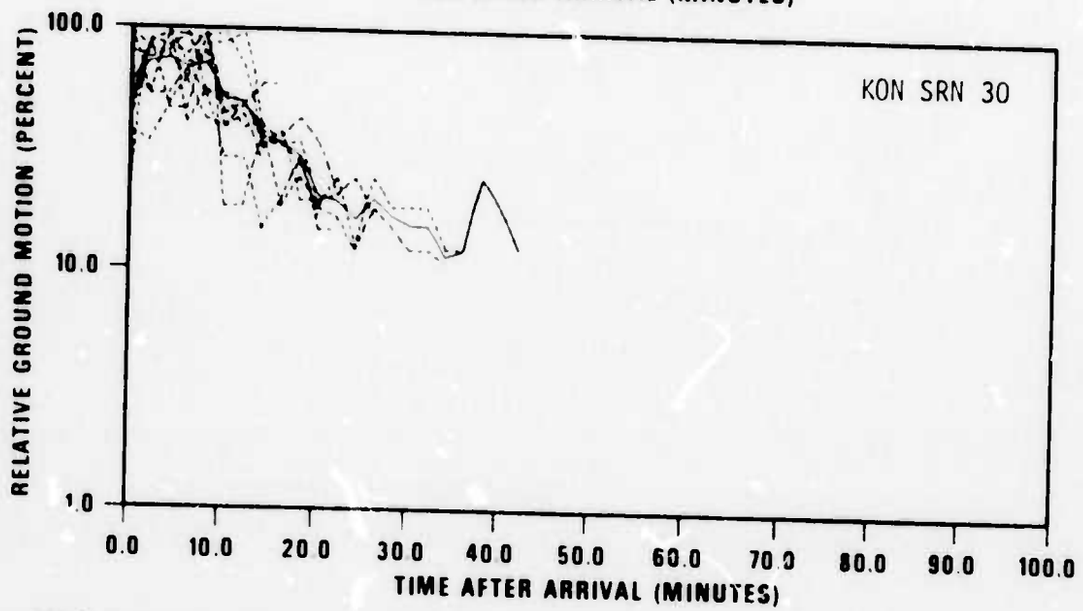
KON SRN 30
RELATIVE GROUND MOTION (PERCENT)
100.0
10.0
1.0
0.0
10.0
20.0
30.0
40.0
50.0
60.0
70.0
80.0
90.0
100.0
TIME AFTER ARRIVAL (MINUTES)

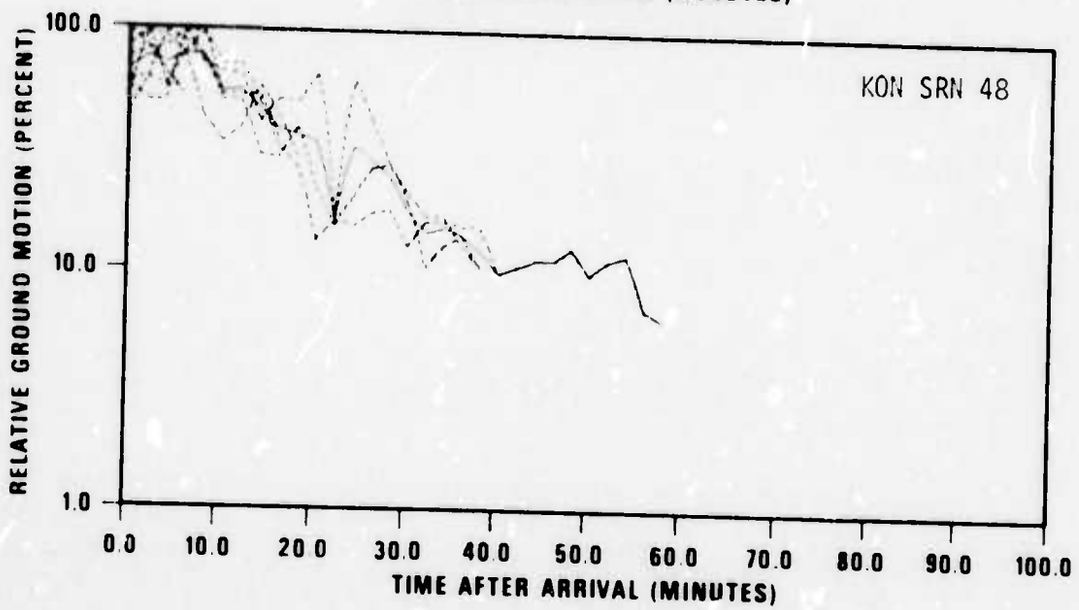
KON SRN 48
RELATIVE GROUND MOTION (PERCENT)
100.0
10.0
1.0
0.0
10.0
20.0
30.0
40.0
50.0
60.0
70.0
80.0
90.0
100.0
TIME AFTER ARRIVAL (MINUTES)

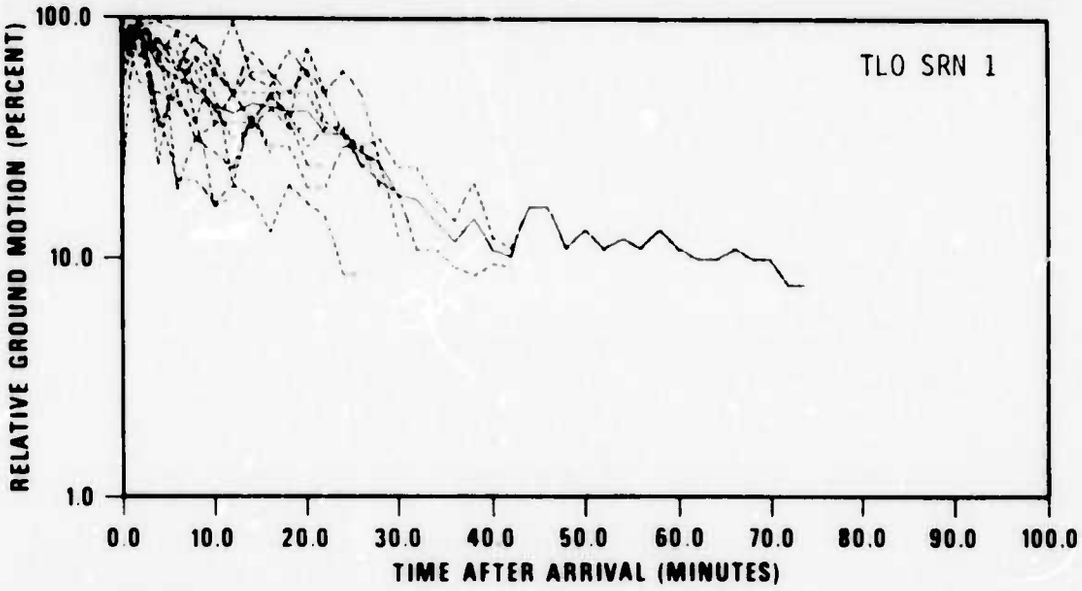
TLO SRN 1
RELATIVE GROUND MOTION (PERCENT)
100.0
10.0
1.0
0.0
10.0
20.0
30.0
40.0
50.0
60.0
70.0
80.0
90.0
100.0
TIME AFTER ARRIVAL (MINUTES)

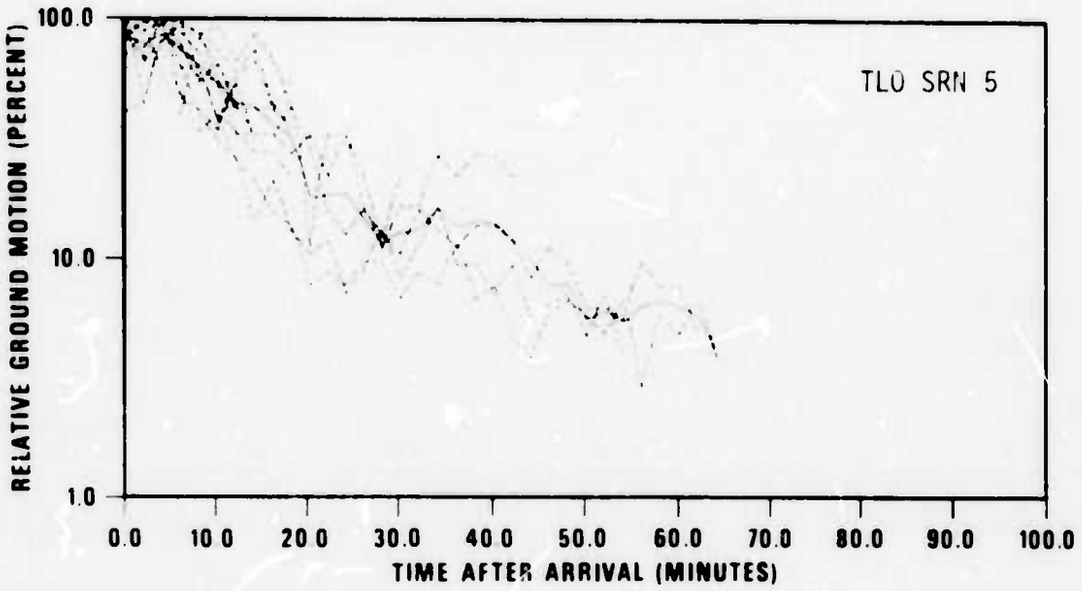
TLO SRN 5
RELATIVE GROUND MOTION (PERCENT)
100.0
10.0
1.0
0.0
10.0
20.0
30.0
40.0
50.0
60.0
70.0
80.0
90.0
100.0
TIME AFTER ARRIVAL (MINUTES)

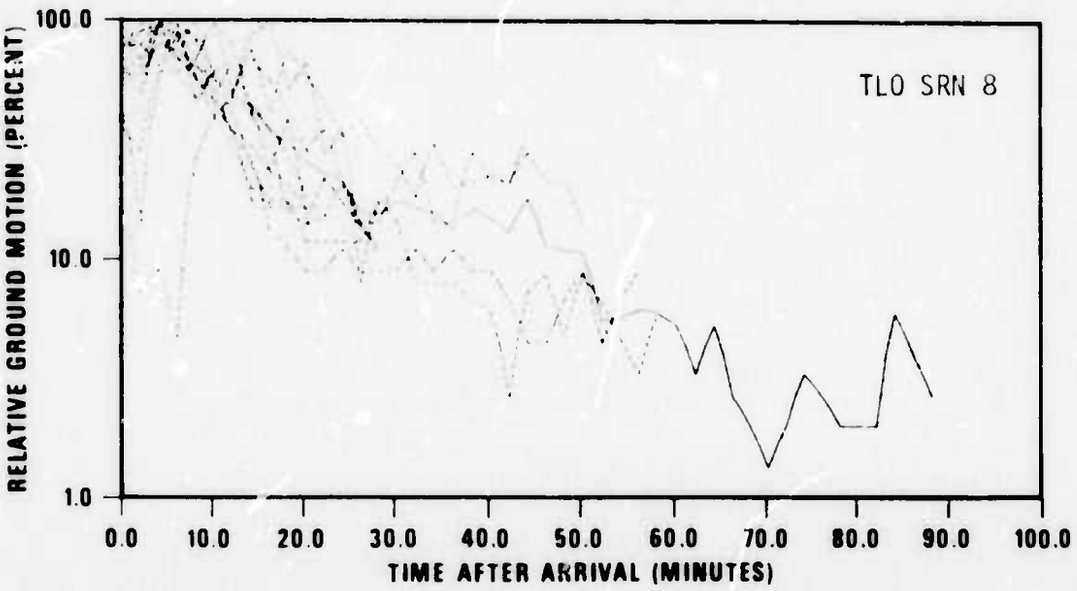
TLO SRN 8
RELATIVE GROUND MOTION (PERCENT)
100.0
10.0
1.0
0.0
10.0
20.0
30.0
40.0
50.0
60.0
70.0
80.0
90.0
100.0
TIME AFTER ARRIVAL (MINUTES)

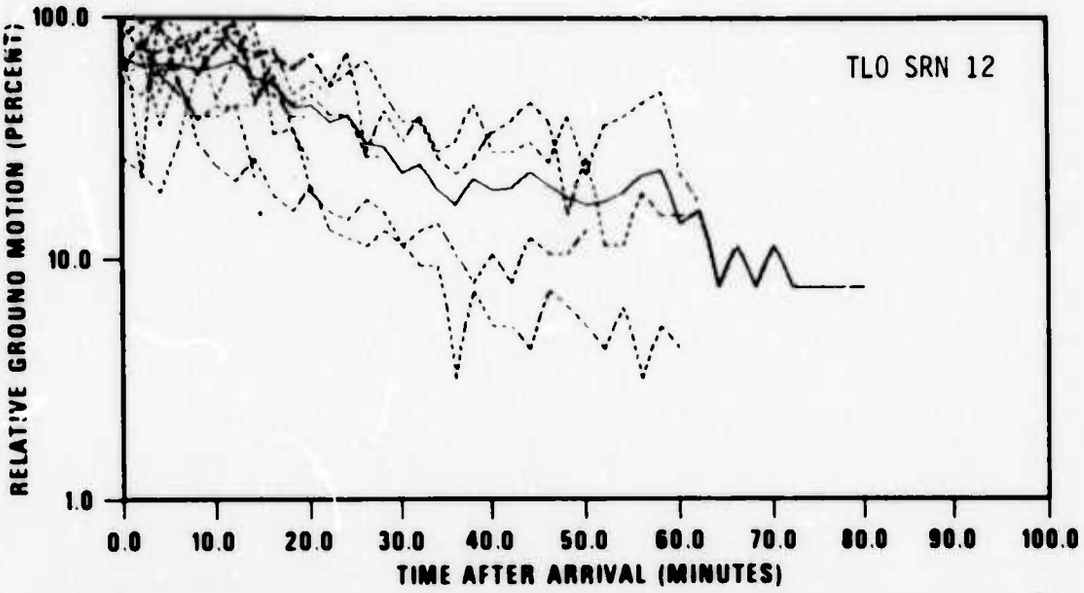
TLO SRN 12
RELATIVE GROUND MOTION (PERCENT)
100.0
10.0
1.0
0.0
10.0
20.0
30.0
40.0
50.0
60.0
70.0
80.0
90.0
100.0
TIME AFTER ARRIVAL (MINUTES)

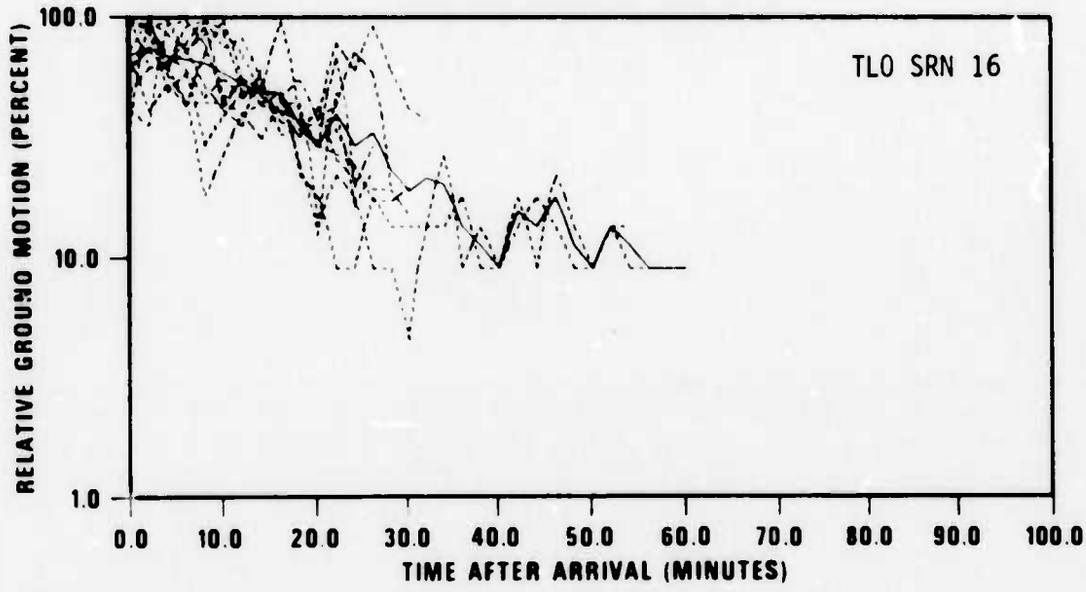
TLO SRN 16
RELATIVE GROUND MOTION (PERCENT)
100.0
10.0
1.0
0.0
10.0
20.0
30.0
40.0
50.0
60.0
70.0
80.0
90.0
100.0
TIME AFTER ARRIVAL (MINUTES)

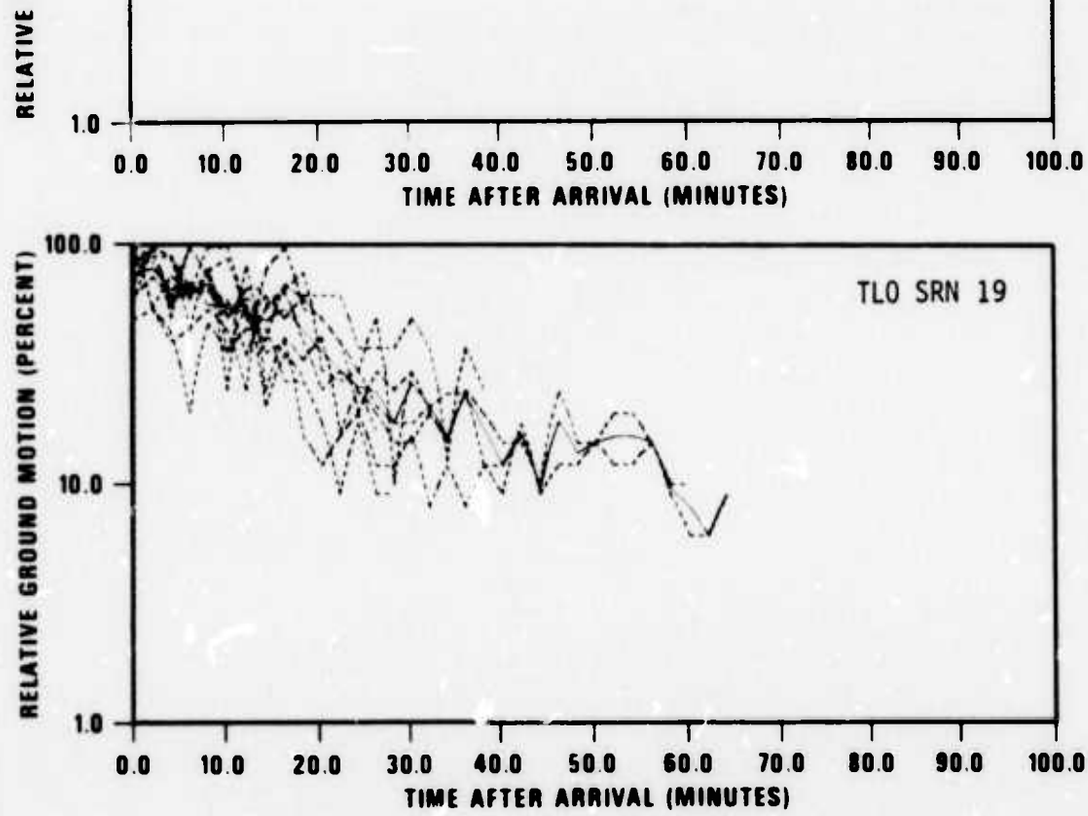
TLO SRN 19
RELATIVE GROUND MOTION (PERCENT)
100.0
10.0
1.0
0.0
10.0
20.0
30.0
40.0
50.0
60.0
70.0
80.0
90.0
100.0
TIME AFTER ARRIVAL (MINUTES)

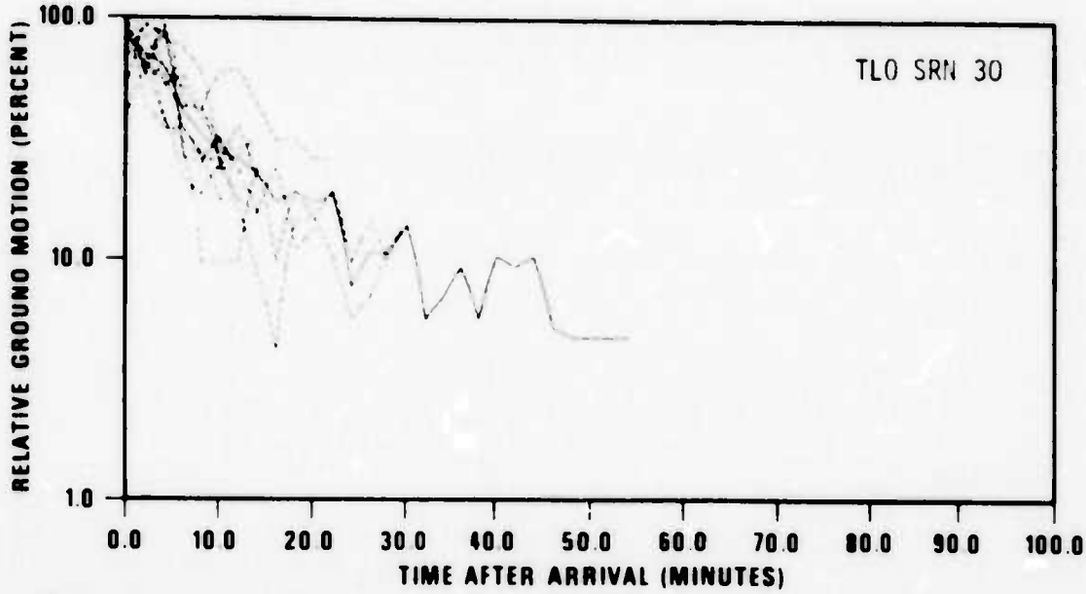
TLO SRN 30
RELATIVE GROUND MOTION (PERCENT)
100.0
10.0
1.0
0.0
10.0
20.0
30.0
40.0
50.0
60.0
70.0
80.0
90.0
100.0
TIME AFTER ARRIVAL (MINUTES)

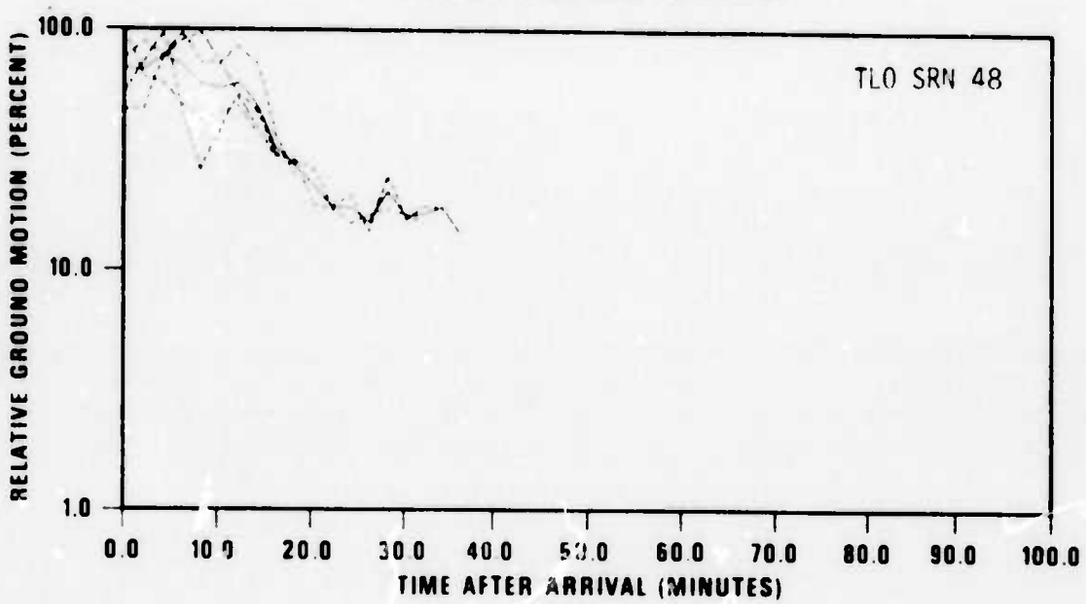
TLO SRN 48
RELATIVE GROUND MOTION (PERCENT)
100.0
10.0
1.0
0.0
10.0
20.0
30.0
40.0
50.0
60.0
70.0
80.0
90.0
100.0
TIME AFTER ARRIVAL (MINUTES)